



Cyprus  
University of  
Technology



杭州电子科技大学  
HANGZHOU DIANZI UNIVERSITY

Master's Thesis

# Research on Cardiac Health Detection

## Sensors Based on CYTOP Fiber Bragg

### Grating

Hu Yuchi

Limassol, May 2025

 MSc in Electronics Science  
and Technology



CYPRUS UNIVERSITY OF TECHNOLOGY  
FACULTY OF ENGINEERING AND TECHNOLOGY  
DEPARTMENT OF ELECTRICAL ENGINEERING AND COMPUTER  
ENGINEERING AND INFORMATICS

Master's Thesis

**Research on Cardiac Health Detection Sensors Based on  
CYTOP Fiber Bragg Grating**

Hu Yuchi

Supervisor

**Prof. Kyriacos Kalli**

Limassol, May 2025

## **Approval Form**

Master's Thesis

### **Research on Cardiac Health Detection Sensors Based on CYTOP Fiber Bragg Grating**

Presented by

Hu Yuchi

Supervisor: [Faculty of Engineering and Technology, Dr. Kyriacos Kalli, Professor]

Member of the committee: [Faculty of Engineering and Technology, Dr. Paul Christodoulides, Assistant Professor]

Member of the committee: [Faculty of Engineering and Technology, Dr. Andreas Ioannou, Researcher]

Cyprus University of Technology

Limassol, May 2025

## **Copyrights**

Copyright© 2025 Hu Yuchi

All rights reserved.

The approval of the thesis by the Department of Electrical Engineering and Computer Engineering and Informatics does not necessarily imply the approval by the Department of the writer's views.

## **Acknowledgements**

During the preparation and research for this thesis, I received invaluable guidance and unwavering support from my advisor, Professor Kyriacos Kalli. His rigorous academic approach and patient mentorship not only significantly enhanced my scientific thinking and research skills but also provided me with continuous care and support, ensuring the successful completion of this thesis.

My heartfelt thanks to my senior Dr.Andreas Ioannou for his patient guidance and mentorship during the experimental phases. His invaluable assistance helped me overcome numerous experimental challenges, greatly enhancing my research capabilities and practical experience.

Special appreciation goes to the Cyprus University of Technology (CUT) Photonics and Optical Sensors Research Laboratory for providing excellent research facilities and abundant resources. All researchers in the laboratory generously shared their extensive knowledge and selfless assistance, profoundly influencing my academic and personal development.

I would also deeply grateful to all the professors at CUT for their considerable support and encouragement throughout the past year, both academically and personally.

Finally, I would like to extend my sincere gratitude once again to everyone who has provided guidance and assistance during the preparation of this thesis.

## ABSTRACT

This study focuses on the development of a fiber Bragg grating (FBG) sensor based on CYTOP polymer optical fiber for non-invasive and dynamic detection of cardiac mechanical activity. FBGs were inscribed in CYTOP fibers using femtosecond laser plane-by-plane processing, and encapsulated with Polydimethylsiloxane (PDMS) to create a flexible sensor unit that can be attached to the skin surface. After completing the construction of the experimental system—including structural design, signal demodulation, and data processing—human body test were conducted at three key thoracic sites (Inferior Apical, Left Parasternal, and Midsternal) and one posterior site (Medial Inferior Scapular Angle) to acquire respiratory rate (RR), heart rate (HR), and seismocardiogram (SCG) signals.

The results demonstrate that compared to conventional silica fiber sensors, the polymer-based FBG sensor exhibits significantly enhanced sensitivity and is capable of stably extracting key SCG waveform features (e.g., AO, MC, IC, and AC). Compared to reference measurements, the heart rate error remained within  $\pm 3$  bpm, meeting the system's design expectations. In addition, the sensor was extended to the radial artery at the wrist, where clear pulse waveforms were successfully acquired, validating its potential for peripheral blood flow monitoring.

Compared with traditional cardiac mechanical function assessment tools, the proposed system offers advantages such as non-invasiveness, lightweight construction, low cost, and suitability for continuous dynamic monitoring. These characteristics indicate strong potential for future medical applications.

**Keywords:** CYTOP fiber; fiber Bragg grating (FBG); femtosecond laser inscription; heart rate (HR); respiratory rate (RR); seismocardiogram (SCG)

## Table of Contents

ABSTRACT .....	vi
LIST OF TABLES .....	x
LIST OF FIGURES .....	xi
LIST OF ABBREVIATIONS .....	xvi
1    Introduction .....	1
1.1    Research Background and Significance: .....	1
1.2    Current Research Status of Fiber: .....	2
1.3    Research Content and Structure .....	3
2    Literature review .....	5
2.1    Optical fiber applications in cardiac signal detection .....	5
2.2    The material properties and current applications of CYTOP optical fibers .....	10
2.3    The Application of Femtosecond Laser Processing Technology in Sensor Fabrication.....	14
2.4    The Application of 3D Printing Technology in Sensors .....	20
2.5    The Application of Polymer Materials in Packaging .....	23
3    Research Theory and Methodology .....	26
3.1    Generation and Transmission of Cardiac Mechanical Signals .....	26
3.2    Characteristics and Sensing Principle of Fiber Bragg Grating (FBG) .....	28
3.2.1    Basic Structure and Transmission Characteristics of Optical Fiber .....	28
3.2.2    Optical Properties of Fiber Bragg Gratings (FBG) .....	31
3.2.3    Coupled-Mode Theory of Fiber Bragg Gratings .....	33
3.3    Demodulation Methods of FBG Sensors .....	37
3.4    FBG Sensor Application Mechanism in Cardiac Signal Detection .....	42
4    Fabrication of CYTOP Fiber FBG Sensors .....	44
4.1    CYTOP Optical Fiber and Fabrication Process of FBG .....	44

4.1.1	Characteristics of CYTOP Optical Fiber .....	44
4.1.2	Fabrication Process of FBG .....	46
4.2	Fabrication of FBGs Using Femtosecond Laser Technology .....	53
4.3	Application of 3D Printing and Polymer Materials for Packaging .....	60
5	Results and Discussion .....	66
5.1	Experimental setup .....	66
5.1.1	Overview of system architecture design .....	66
5.1.2	Integrated FBG Demodulation System .....	67
5.1.3	Vibration Platform and Excitation System .....	68
5.2	Preliminary experiments: Influence of structural parameters on FBG sensitivity	
	70	
5.2.1	Influence of pre-strain on FBG sensitivity .....	70
5.2.2	Effect of packaging on sensing performance .....	74
5.3	Vibration frequency response testing .....	77
5.3.1	Low-frequency range (0.1–0.9 Hz): Response under large-amplitude excitation .....	78
5.3.2	Mid-frequency range (1–10 Hz): Response under moderate-amplitude excitation .....	82
5.3.3	High-frequency range (10–100 Hz): Response under micro-amplitude excitation .....	86
5.3.4	Summary of vibration response across all frequencies .....	90
5.4	In Vivo Cardiac Signal Monitoring Experiments .....	91
5.4.1	Experimental Setup and Background .....	91
5.4.2	Signal Acquisition and Data Analysis Pipeline .....	93
5.4.3	Preliminary Experiment: Sensor Positioning and Sensitivity Verification	
	94	
5.4.4	Cardiac Signal Analysis at Thoracic Sites .....	99

5.4.5	Pulse Signal Detection at the Wrist.....	115
5.4.6	Signal Analysis and Evaluation .....	118
5.4.7	Experimental Summary .....	122
	Conclusion and Outlook .....	123
	BIBLIOGRAPHY .....	125

## **LIST OF TABLES**

Table 1: Measured heart rate, reference heart rate, and error statistics across different test sites .....	118
--	-----

## LIST OF FIGURES

Figure 1: Single-mode-multimode-single-mode (SMS) fiber structure [33] .....	6
Figure 2: Sensor (FOS) system based on single-mode fiber Mach-Zehnder Interferometer (MZI) and coupler [34] .....	6
Figure 3: SMS Structure-Based SCG Sensing Schematic Diagram [35] .....	7
Figure 4: Ballistocardiography (BCG) FBG sensor array [39] .....	9
Figure 5: Smart mattress structure with embedded FBG sensors [40] .....	10
Figure 6: POF-FBG sensing system within an aircraft wing [42] .....	11
Figure 7: Experimental setup for characterizing the CYTOP fiber-based curvature sensor for human activity simulation [48] .....	13
Figure 8: CYTOP fiber FBG brain temperature sensor unit [51] .....	14
<b>Figure 9:</b> Different methods of femtosecond laser direct writing: (a) P-b-P; (b) L-b-L; .....	16
Figure 10: Timing control system for femtosecond laser P-b-P grating writing [56] .....	17
<b>Figure 11:</b> Schematic of two femtosecond laser L-b-L grating writing methods: .....	18
Figure 12: Schematic of femtosecond laser Pl-b-Pl method for creating CTFBG in single-mode fiber [59] .....	19
Figure 13: Sensor packaging: (a) placing the FBG on the ABS lower layer; (b) reprinting and curing the encapsulated FBG sensor [62] .....	21
Figure 14: 3D-printed maxillary model: (a) FBG sensor demodulation system; (b) Hyrax expander before activation; (c) Hyrax expander after activation [63] .....	22
Figure 15: PDMS-coated single-mode fiber – no-core fiber – single-mode fiber (SMF-NCF-SMF) structure [64] .....	24
Figure 16: Fabrication methods for pressure sensors combining SMF with PDMS in different ratios [65] .....	24
Figure 17: Elastic cardiopulmonary monitoring sensor made of PDMS material [66] ..	25
Figure 18: Optic Fiber Foundation Structure .....	29

Figure 19: Light Propagation in Optical Fiber .....	29
Figure 20: Structure of Fiber Bragg Grating .....	31
Figure 21: Schematic Diagram of Spectrometer Demodulation Method .....	38
Figure 22: Schematic Diagram of the Edge Filter Demodulation Method .....	39
Figure 23: Schematic Diagram of the Matched FBGFilter Method .....	40
Figure 24: Schematic Diagram of Tunable F-P Filter Demodulation Method .....	41
Figure 25: Schematic Diagram of Tunable Narrowband Light Source Demodulation ..	42
Figure 26: Chemical Structure of CYTOP Material .....	44
Figure 27: Schematic Diagram of the Amplitude Splitting Interference Method .....	48
Figure 28: Schematic Diagram of Femtosecond Laser Inscription .....	50
Figure 29: Phase Mask Method Schematic .....	51
Figure 30: FBGProcessing Fixture .....	55
Figure 31: Schematic Diagram of Grating Inscription Structure .....	55
Figure 32: Complete Femtosecond Laser Processing System .....	56
Figure 33: CYTOP Optical Fiber FBG (Pl-by-Pl Inscription) .....	57
Figure 34: Experimental Setup of Fiber Butt-coupling .....	57
Figure 35: FBG reflection spectrum in CYTOP fiber .....	58
Figure 36: Silica Single-Mode Fiber FBG (P-by-P Inscription) .....	59
Figure 37: FBG reflection spectrum in SMF-28 fiber .....	60
Figure 38: Sensor Packaging Substrate Model .....	61
Figure 39: PDMS Material Preparation Process .....	62
Figure 40: Layout of the FBG Sensing Unit .....	63
Figure 41: Encapsulation Process of the FBG Sensor .....	63
Figure 42: Optical Fiber FBG-Based Cardiac Sensor .....	65
Figure 43: Designed Structure of the FBG Sensing and Demodulation System .....	66
Figure 44: Simplified Structure of the Integrated Demodulation System .....	67

Figure 45: Reflection Spectra of Dual-Channel FBGs .....	68
Figure 46: Structure of the Excitation System and Vibration Platform .....	69
Figure 47: Fiber attachment methods with different pre-strain levels .....	71
Figure 48: Initial reflection spectra under varying pre-strain conditions .....	72
Figure 49: Baseline stability test under no excitation .....	72
Figure 50: FBG wavelength responses to 1 Hz sine-wave excitation.....	73
Figure 51: FBG wavelength responses to 1 Hz square-wave excitation.....	73
Figure 52: Sensor installation in Normal and Reversed Placements .....	75
Figure 53: Reflection spectra of FBGs under different placements .....	75
Figure 54: Dynamic responses of FBG in different placements: (a) Normal Placement; (b) Reversed Placement .....	76
Figure 55: Wavelength responses under 0.1–0.9 Hz sine wave excitation .....	79
Figure 56: Average wavelength shift ( $\Delta\lambda$ ) under 0.1-0.9Hz sine wave excitation .....	79
Figure 57: Sensitivity ratio ( $\Delta\lambda_{CYTOP} / \Delta\lambda_{SMF-28}$ ) under 0.1-0.9Hz sine wave excitation	80
Figure 58: Wavelength responses under 0.1–0.9 Hz square wave excitation .....	80
Figure 59: Average wavelength shift ( $\Delta\lambda$ ) under 0.1-0.9Hz square wave excitation .....	81
Figure 60: Sensitivity ratio ( $\Delta\lambda_{CYTOP} / \Delta\lambda_{SMF-28}$ ) under 0.1-0.9Hz square wave excitation .....	81
Figure 61: Wavelength responses under 1-10 Hz sine wave excitation .....	83
Figure 62: Average wavelength shift ( $\Delta\lambda$ ) under 1-10Hz sine wave excitation .....	83
Figure 63: Sensitivity ratio ( $\Delta\lambda_{CYTOP} / \Delta\lambda_{SMF-28}$ ) under 1-10Hz sine wave excitation ....	84
Figure 64: Wavelength responses under 1-10 Hz square wave excitation .....	84
Figure 65: Average wavelength shift ( $\Delta\lambda$ ) under 1-10Hz square wave excitation .....	85
Figure 66: Sensitivity ratio ( $\Delta\lambda_{CYTOP} / \Delta\lambda_{SMF-28}$ ) under 1-10Hz square wave excitation	85
Figure 67: Wavelength responses under 10-100 Hz sine wave excitation.....	87
Figure 68: Average wavelength shift ( $\Delta\lambda$ ) under 10-100Hz sine wave excitation .....	87

Figure 69: Sensitivity ratio ( $\Delta\lambda_{CYTOP} / \Delta\lambda_{SMF-28}$ ) under 10-100Hz sine wave excitation	88
Figure 70: Average wavelength shift ( $\Delta\lambda$ ) under 10-100Hz square wave excitation .....	88
Figure 71: Average wavelength shift ( $\Delta\lambda$ ) under 10-100Hz square wave excitation .....	89
Figure 72: Sensitivity ratio ( $\Delta\lambda_{CYTOP} / \Delta\lambda_{SMF-28}$ ) under 10-100Hz square wave excitation .....	89
Figure 73: Sensitivity ratio (CYTOP vs. SMF-28) across all frequency bands .....	90
Figure 74: Layout at selected body sites .....	92
Figure 75: FBG-based system workflow for in vivo cardiac signal acquisition and processing .....	93
Figure 76: Initial signal comparison between multi-point SMF-28 FBG array and CYTOP FBG at the same location .....	95
Figure 77: Raw and filtered signals collected by CYTOP and center SMF-28 FBGs ....	96
Figure 78: Enlarged HR waveform comparison: CYTOP vs. SMF-28 .....	97
Figure 79: Enlarged SCG waveform comparison: CYTOP vs. SMF-28 .....	98
Figure 80: Response at the inferior apical region under sitting posture with normal breathing .....	100
Figure 81: Response at the inferior apical region under standing posture with normal breathing .....	101
Figure 82: Response at the inferior apical region under sitting posture with breath-hold .....	102
Figure 83: Response at the inferior apical region under standing posture with breath-hold .....	103
Figure 84: Response at the left parasternal region under sitting posture with normal breathing .....	104
Figure 85: Response at the left parasternal region under standing posture with normal breathing .....	105
Figure 86: Response at the left parasternal region under sitting posture with breath-hold .....	106

Figure 87: Response at the left parasternal region under standing posture with breath-hold .....	107
Figure 88: Response at the midsternal region under sitting posture with normal breathing .....	108
Figure 89: Response at the midsternal region under standing posture with normal breathing .....	109
Figure 90: Response at the midsternal region under sitting posture with breath-hold .	110
Figure 91: Response at the midsternal region under standing posture with breath-hold .....	111
Figure 92: Response at the medial inferior scapular angle under sitting posture with normal breathing .....	112
Figure 93: Response at the medial inferior scapular angle under standing posture with normal breathing .....	113
Figure 94: Response at the medial inferior scapular angle under sitting posture with breath-hold .....	114
Figure 95: Response at the medial inferior scapular angle under standing posture with breath-hold .....	115
Figure 96: Bragg wavelength response of CYTOP FBG at the wrist under relaxed condition .....	116
Figure 97: Bragg wavelength response of CYTOP FBG at the wrist under fist-clenching condition .....	117
Figure 98: Detailed SCG waveform and annotated feature points at the Inferior Apical Region .....	120
Figure 99: Detailed SCG waveform and annotated feature points at the Left Parasternal Region .....	120
Figure 100: Detailed SCG waveform and annotated feature points at the Midsternal Region .....	121

## **LIST OF ABBREVIATIONS**

CUT	Cyprus University of Technology
CVD	Cardiovascular disease
ECG	Electrocardiography
BCG	Ballistocardiography
SCG	Seismocardiography
PWV	Pulse Wave Velocity
PCG	Phonocardiography
FBG	Fiber Bragg Grating
CYTOP	Cyclic Transparent Optical Polymer
POF	Polymer Optical Fiber
bpm	Beats Per Minute
MZI	Mach-Zehnder interferometer
HRV	heart rate variability
PDMS	Polydimethylsiloxane
SMF	Single-mode Fiber
MMF	multi-mode fibers
RR	respiratory rate
HR	heart rate

# 1 Introduction

## 1.1 Research Background and Significance:

Cardiovascular disease (CVD) is the most prevalent illness and the leading cause of death, remaining a major global health threat. According to WHO, in 2019 alone, CVDs accounted for an estimated 17.9 million deaths, representing 32% of all global fatalities, with heart attacks and strokes responsible for 85% of these cases [[Cardiovascular diseases \(CVDs\)](#)]. This alarming toll continues to place immense pressure on public health systems and significantly affects the quality of life for millions, highlighting the urgent need for effective prevention and treatment strategies.

The heart, as one of the core organs of the human body, plays a vital role in supplying blood and oxygen to the entire body. The proper functioning of the heart is directly linked to human health and serves as a key indicator for evaluating the condition of the cardiovascular system. Information such as heart rate, cardiac output, and blood pressure reflects the health status of the circulatory system and can provide early warnings of diseases such as hypertension, coronary artery disease, and arrhythmias [1]-[10]. Therefore, real-time and accurate monitoring of cardiac activity is crucial for health management, disease prevention, and clinical treatment. With advancements in biomedical technology, modern medicine now offers various precise methods for monitoring cardiac activity, including the following:

**Electrocardiography (ECG)** [11]-[12]: ECG records the electrical signals generated by the heart using electrode patches, providing a detailed waveform of the heart's electrical activity. By analyzing these waveforms, doctors can monitor heart rate and rhythm and diagnose issues such as arrhythmias and myocardial ischemia.

**Ballistocardiography (BCG)** [13]-[14]: BCG utilizes subtle body motion signals caused by heartbeats to indirectly reflect the heart's mechanical activity. By detecting these small movements induced by cardiac pumping, this technique evaluates cardiac output and blood circulation, offering excellent temporal resolution.

**Seismocardiography (SCG)** [15]-[16]: SCG captures micro-vibrations of the chest wall induced by the mechanical activity of the heart. By detecting vibrations generated by myocardial contraction, valve motion, and blood flow, SCG reflects the mechanical

properties of the heart. This technique enables the assessment of cardiac contractile function and mechanical compliance, offering high temporal resolution.

Pulse Wave Velocity (PWV) [17]-[18]: PWV measures the blood pressure waveforms propagating through arteries, reflecting vascular health and cardiac activity. This method provides insights into arterial elasticity and blood pressure variation, making it especially important for monitoring hypertension patients.

Phonocardiography (PCG) [19]-[20]: PCG records the sounds produced by heart valve opening and closing to analyze cardiac health. These heart sounds help identify murmurs and valve abnormalities, providing critical information about the structural and functional aspects of the heart.

Although these methods each have certain advantages, their application is often limited by environmental interferences, such as electromagnetic noise and lack of portability [21]-[23]. These challenges can compromise the stability and accuracy of signals in certain scenarios. Moreover, early cardiac conditions, such as arrhythmias, premature beats, or mild valve abnormalities, require higher precision in cardiac data monitoring. High-resolution cardiac signals are essential for detecting subtle and transient abnormalities in cardiac electrical activity, which may go unnoticed in traditional low-resolution detection methods. This capability is critical for diagnosing acute conditions like cardiomyopathy or latent myocardial ischemia.

Therefore, developing more portable, stable, interference-resistant, and highly precise monitoring technologies is of paramount importance.

## 1.2 Current Research Status of Fiber:

Fiber optic sensing technology has gradually gained attention in modern health monitoring [24]-[26], with examples of its applications including heart monitoring systems based on Fiber Bragg Grating (FBG) sensors. FBG sensors can precisely measure subtle physical changes, such as temperature and pressure variations, through the reflective properties of light, indirectly reflecting cardiac physiological activities. One prominent advantage of this technology is its excellent resistance to electromagnetic interference, making it particularly suitable for environments with complex electromagnetic conditions, such as hospitals.

Additionally, fiber optic sensors are extremely compact and lightweight, enabling easy integration into various wearable devices for real-time monitoring [27]-[29]. This non-invasive measurement approach reduces patient discomfort, is suitable for prolonged use, and allows simultaneous monitoring of multiple physiological parameters such as heart rate and respiratory rate. The reliability of fiber optic sensors in extreme conditions, such as high temperatures in fire scenes or strong magnetic fields in MRI environments [30]-[31], also makes them ideal for remote real-time detection and medical health monitoring.

By reducing reliance on traditional electrodes, fiber optic technology demonstrates significant advantages in improving signal stability and accuracy, paving the way for future advancements in health monitoring technologies.

Therefore, cardiac health monitoring sensor research has been conducted based on fiber optic sensors. By leveraging the advantages of various materials, structures, and fabrication techniques for FBG sensors, efforts are made to continually enhance sensor sensitivity and optimal detection capability. Additionally, through testing and comparing different sensors, this research provides a foundation and reference for future cardiac health monitoring technologies. This will contribute to the development of more reliable and effective monitoring systems to meet the growing demands for health management.

### 1.3 Research Content and Structure

This paper primarily focuses on the research of cardiac health monitoring sensors based on CYTOP (Cyclic Transparent Optical Polymer) FBG, exploring the application of this technology in cardiac signal monitoring and optimizing it through innovative manufacturing processes and novel materials. The paper is divided into six chapters, with the specific content and structure as follows:

**Chapter 1** is the introduction. It first presents the research background and significance of cardiac signal detection, highlighting the importance of cardiac health monitoring in medical diagnosis. Then, it lists several commonly used cardiac diagnostic signals in clinical practice and discusses their applications in clinical settings. Finally, it provides an overview of the latest research progress of FBG technology in cardiac signal

monitoring, with a focus on its current applications in sensor environments, accuracy enhancement, and other application fields.

**Chapter 2** is a literature review that primarily presents the latest methods for heart signal detection. It reviews the current research status of heart signal detection, with a focus on the application and progress of FBG technology in this field. In addition, the material properties of CYTOP fibers and their current applications in sensors are discussed in detail. Finally, the chapter briefly covers the application of special processes and novel materials in sensor fabrication and packaging, laying the foundation for subsequent research work.

**Chapter 3** focuses on the fundamental theories and methodologies of the research, primarily introducing the theoretical studies on heart signal detection based on FBG sensors. It begins with an analysis of the basic mechanisms of heart signal sensing, followed by a brief introduction to the basic principles of optical fibers. The chapter then emphasizes the working mechanism and response characteristics of FBG sensors. Finally, it provides a detailed analysis of the signal demodulation methods for FBG sensors, offering theoretical support for the subsequent experimental research.。

**Chapter 4** discusses the fabrication methods of FBG sensors based on CYTOP optical fibers. It begins by providing a detailed explanation of various FBG fabrication processes. Next, it elaborates on the process of writing FBGs in CYTOP optical fibers using femtosecond laser processing technology. The chapter then demonstrates the process of modeling and printing special structures using 3D printing technology, followed by the encapsulation of FBG sensors with PDMS materials.

**Chapter 5** is the Results and Discussion, providing a detailed explanation of the overall sensing structure for heart health monitoring based on CYTOP FBG sensors. It begins with the design of the experimental system, followed by the preparation and parameter settings for the related experiments. Next, it compares the vibration responses of CYTOP fiber FBG sensors and silica-based fiber FBGs. Afterward, heart signals are tested, and the collected data are processed and analyzed in comparison with ECG signals, discussing the performance of the sensors in practical applications.

The final section is the **Conclusion and Outlook**. It begins by summarizing the research findings of this paper, reviewing the development process and experimental

validation of the CYTOP FBG-based heart health monitoring sensor. Lastly, it looks ahead to future research directions and potential applications of this technology, offering suggestions for further improving sensor performance and system integration.

**In summary**, this paper systematically explores the heart health monitoring technology based on CYTOP FBG sensors, from theoretical research and experimental verification to data processing, demonstrating the application potential of this technology in the field of health monitoring.

## 2 Literature review

### 2.1 Optical fiber applications in cardiac signal detection

Cardiac signal detection plays a crucial role in cardiovascular health monitoring, as it provides real-time, non-invasive data on heart health, which is essential for the prevention and diagnosis of CVDs. In recent years, research in this field has advanced rapidly worldwide, particularly with innovations in wearable and implantable sensors that have significantly driven progress in cardiac signal detection technologies.

Due to their high sensitivity, strong resistance to electromagnetic interference, and capabilities for miniaturization and lightweight design, fiber optic sensor technologies have received extensive attention in recent years. The excellent corrosion resistance and biocompatibility of fiber optic materials enable stable long-term operation in physiological environments, giving rise to numerous applications in biomedicine [32]. Additionally, fiber optic sensors possess distributed measurement capabilities, making them well-suited for multipoint monitoring requirements.

Irawati et al.[33] proposed and developed a heart rate monitoring sensor system based on a single-mode-multimode-single-mode (SMS) fiber structure, as shown in **Figure 1**. Experimental results demonstrated that the sensor exhibited a good linear frequency response within a working range of 50 to 200 beats per minute (bpm) when tested with artificially generated ECG signals simulating heartbeat pulses. The sensor achieved a sensitivity of 0.014 dBm/bpm, with high signal stability and repeatability. The SMS fiber structure detects pulse vibrations by monitoring changes in optical power intensity.

This type of fiber optic sensor features advantages such as fast response and low manufacturing cost, making it suitable for long-term, high-stability heart rate

monitoring. It shows great potential for widespread application in hospitals and other settings.

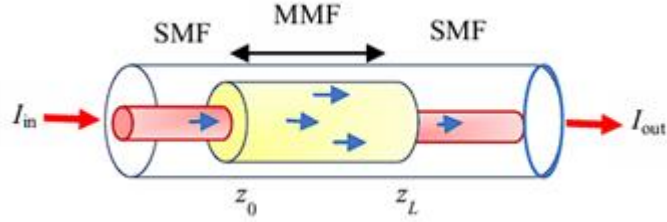


**Figure 1:** Single-mode-multimode-single-mode (SMS) fiber structure [33]

Lyu et al. [34] proposed a low-cost fiber optic sensor (FOS) system based on a single-mode fiber Mach-Zehnder interferometer (MZI) and coupler. The system places the FOS under a mattress, with three electrodes connected to the chest and abdomen to collect multimodal signals for BCG and ECG via a multimodal signal acquisition board, as illustrated in **Figure 2**. This system enables long-term stable measurement of cardiac vibrations (BCG) and short-term heart rate variability (HRV) analysis.

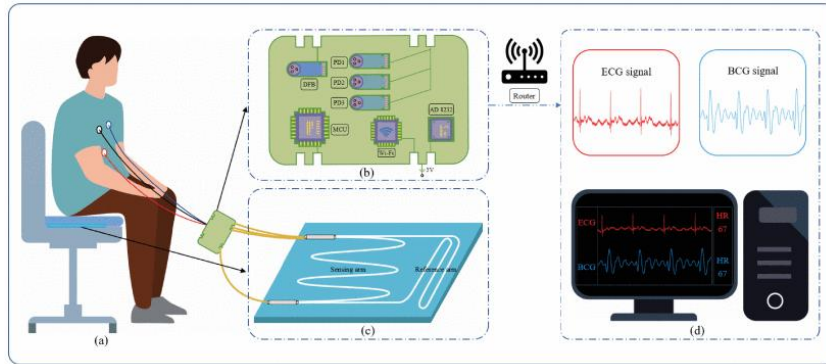


**Figure 2:** Sensor (FOS) system based on single-mode fiber Mach-Zehnder Interferometer (MZI) and coupler [34]

The system uses a low-cost distributed feedback (DFB) laser to couple light into the MZI sensor, where vibrations caused by breathing and heartbeats induce phase shifts in the light, resulting in interference intensity changes. These changes are detected by three photodetectors (PDs). The study demonstrated a high correlation between BCG-derived interbeat intervals (IBI) and those derived from ECG, indicating the system's high accuracy.

The research revealed an inverse relationship between BCG HRV amplitude and breathing frequency, noting that a 0.1 Hz breathing rate induces larger respiratory sinus arrhythmia (RSA) amplitudes and resonance breathing effects. Moreover, at 0.1 Hz and 0.25 Hz, time-domain, frequency-domain, and nonlinear analysis results of BCG HRV were highly correlated with ECG HRV. The BCG monitoring system based on this FOS offers the unique advantage of flexible configuration and allows for non-contact, continuous, and accurate heart rate monitoring, providing additional options for cardiac health assessment.

F.R. Agustiyanto et al. [35] proposed a SCG monitoring method based on a single-mode–multimode–single-mode (SMS) fiber structure, as shown in **Figure 3**. This method utilizes a simple intensity modulation system for detection. The experimental study investigated the vibration response of the SMS fiber structure as a sensor. The results demonstrated that the SMS fiber structure exhibits a linear vibration response within the frequency range of 0–180 Hz, making it suitable for SCG monitoring, which typically requires a low-frequency range of 0–25 Hz. Furthermore, the SCG signals extracted from the optical power of the SMS fiber structure, after filtering, met medical detection requirements.

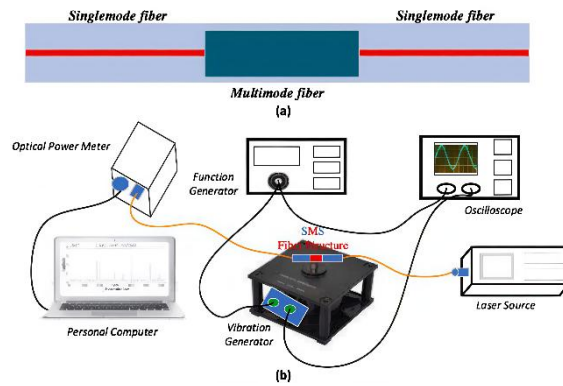


**Figure 3:** SMS Structure-Based SCG Sensing Schematic Diagram [35]

FBG sensing technology, known for its high sensitivity, immunity to electromagnetic interference, and multipoint monitoring capability, has become an ideal choice for precise measurement applications. It has seen rapid development and widespread application across various sensing fields [36]. Due to its sensitivity to physical parameters such as temperature and strain, as well as its ease of integration for remote monitoring and real-time feedback, FBG sensing has emerged as a research hotspot in

health monitoring. Specifically, in monitoring critical physiological parameters like heart rate, blood pressure, and respiration, FBG technology provides innovative solutions for personal health management and chronic disease monitoring[37].

In cardiovascular monitoring, FBG sensors excel at capturing real-time signals such as heart rate and blood pressure. Yuki Haseda et al. [38] developed a pulse wave velocity (PWV) detection system based on plastic optical fiber Bragg gratings (POF-FBG), positioning the sensors over the radial artery to replace traditional silica FBGs. This system effectively records subtle fluctuations in pulse waves, significantly enhancing the signal-to-noise ratio (SNR), with POF-FBG achieving at least eight times the SNR of silica FBG. The signals recorded by POF-FBG closely resemble those obtained via the acceleration plethysmography (APG) method, offering an efficient solution for non-invasive blood pressure monitoring.

Dziuda et al. [39] proposed a method for Ballistocardiogram (BCG) signal acquisition using FBG sensors, capturing subtle mechanical vibrations from the human body to measure cardiac output and blood flow dynamics. The layout of individual and arrayed FBG sensing units is shown in **Figure 4**. By placing an elastic board embedded with FBG sensors between the body and a soft surface, the system detects BCG signals through pressure-induced deformations of the board caused by body movements. The BCG signals are extracted by measuring variations in Bragg wavelength. Experimental results showed a relative error of less than 6.8% between heart rates obtained from BCG signals and reference ECG signals, with statistical analyses confirming satisfactory results.

Compared to traditional strain gauges, the designed FBG sensors demonstrate superior performance in high electromagnetic radiation environments, making them suitable for workplaces like radio operators, radar and sonar operators, and power plant staff. Although the current system's heart rate measurement accuracy requires further optimization, it has successfully been employed for vital sign monitoring during MRI scans without interfering with image quality.

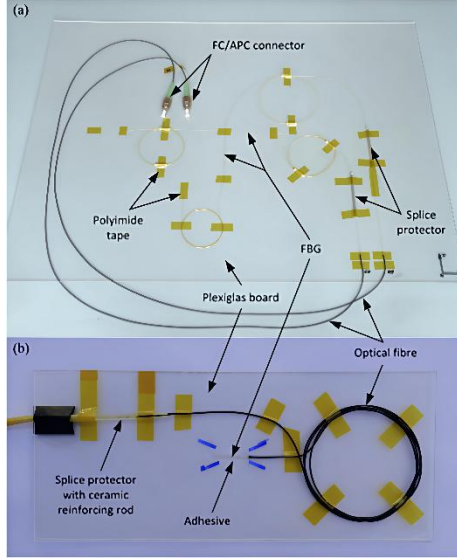


**Figure 4:** Ballistocardiography (BCG) FBG sensor array [39]

There is a physiological connection between breathing and heartbeat, known as Respiratory Sinus Arrhythmia (RSA). During inhalation, the heart rate slightly accelerates, while during exhalation, it slows down. This variation reflects HRV and represents the heart's response to the autonomic nervous system, including the sympathetic and parasympathetic branches. This close relationship between respiratory and cardiac health highlights the importance of their combined monitoring and management in comprehensive health assessments. Respiratory abnormalities and diseases not only affect oxygen supply but also place direct or indirect pressure on the heart, potentially leading to cardiac dysfunction or exacerbating existing heart conditions.

In respiratory monitoring, FBG sensors have been applied due to their sensitive mechanical response characteristics. These sensors can monitor chest and abdominal displacements, providing assessments of respiratory rate and quality. Francesca De Tommasi et al. [40] developed a smart mattress based on FBG technology to monitor respiratory rate (RR), specifically designed for long-term monitoring of patients with sleep-disordered breathing. The mattress incorporates 13 FBG sensing elements embedded in multilayer silicone for user comfort, as shown in **Figure 5**. Test results demonstrate that the mattress can accurately measure RR with an error of less than 0.65 breaths per minute, regardless of sleeping position. This system offers a high-precision,

non-invasive solution for respiratory monitoring, with potential applications in both home and clinical settings.

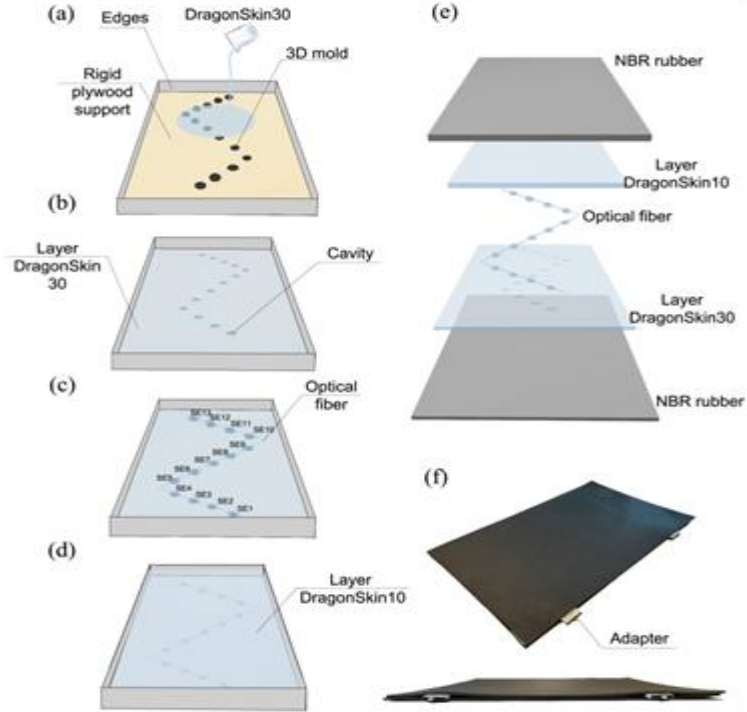


**Figure 5:** Smart mattress structure with embedded FBG sensors [40]

## 2.2 The material properties and current applications of CYTOP optical fibers

In recent years, Polymer Optical Fiber (POF) technology has seen significant advancements. Initially developed as a cost-effective solution for future Fiber-to-the-Home (FTTH) transmission networks, POF has demonstrated unique advantages in the field of sensing due to its material properties [41]. POF offers excellent electromagnetic interference (EMI) resistance, making it particularly effective in environments where signal integrity is critical. Applications include industrial automation sensor networks, extreme environment communication, environmental monitoring, and medical health monitoring.

Pedro C. Lallana et al. [42] investigated the use of POF for sensing applications in aircraft. As shown in **Figure 6**, a sensing array was deployed on the aircraft wing to measure various parameters, including strain, elongation, vibration, temperature, and

liquid levels. The study highlighted the advantages of POF in these diverse sensing tasks. Furthermore, its superior EMI resistance effectively addresses challenges posed by traditional detection methods, such as damage caused by lightning or electrical faults, ensuring reliable performance in such high-risk environments.

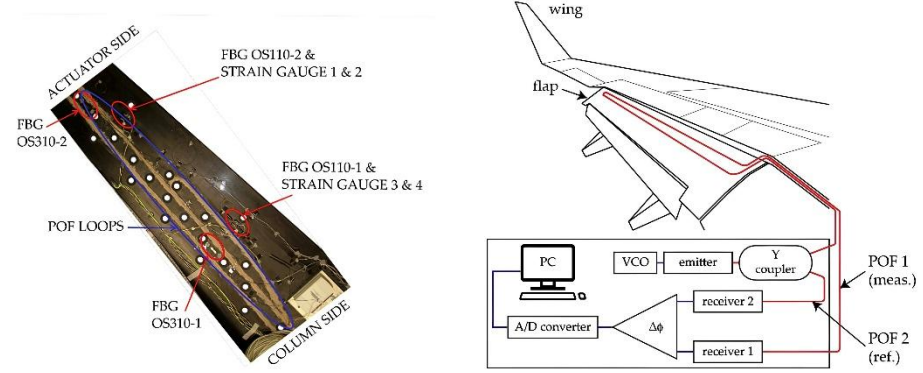


**Figure 6:** POF-FBG sensing system within an aircraft wing [42]

At the same time, the flexibility and bendability of POF make it particularly suitable for applications requiring flexible wiring, such as sensing systems in complex or confined spaces. However, due to its multimode nature, POF tends to suffer from mode mixing and signal interference, which can affect the precision and reliability of sensing. To address these challenges, FBG technology can be integrated into POF, significantly improving performance. By combining FBG with POF, it is possible to accurately monitor parameters such as temperature, pressure, and strain, leading to widespread applications in fields like smart buildings and structural health monitoring of bridges [43], as well as real-time monitoring of health metrics such as respiratory rate and heart rate.

Despite these advantages, POF has a significant drawback in the near-infrared (NIR) wavelength range, where its transmission loss is relatively high, often exceeding 100 dB/m [44]. This high loss limits the working length of the sensors, especially for PMMA (Polymethyl Methacrylate) POF, which can only maintain an effective transmission distance of around 10 cm, severely restricting its practical applications.

Research by Ma et al. [45] on the molecular structure of POF materials revealed that this high loss is primarily due to the high spring constant and small mass characteristics

of the hydrogen atoms in the polymer's molecular backbone. These properties increase the transmission loss of the fiber in the NIR wavelength range.

In response, researchers from AGC Inc. (Asahi Glass Co., Ltd.) in Japan proposed substituting hydrogen with fluorine in the polymer backbone. This modification resulted in a significant reduction in absorption loss within the NIR wavelength range. As a result, CYTOP (perfluorinated polymer) optical fiber, made from this fluorine-substituted material, was developed. It exhibits higher transparency and lower loss, with a loss of less than 60 dB/km at 1300 nm [46].

As a high-performance POF material, CYTOP has gained increasing attention due to its significant advantages over traditional PMMA POF. Its lower transmission loss makes it highly suitable for long-distance and high-precision optical signal transmission in the visible to NIR range (such as 1310 nm and 1550 nm) [47].

In addition, CYTOP optical fiber has higher bending resistance and flexibility, with a low Young's modulus, making it well-suited for applications where frequent bending occurs. Arnaldo et al. [48] used an experimental setup, as shown in **Figure 7**, to simulate the bending movements of the human lower limb. This study explored the unique characteristics of CYTOP optical fiber, demonstrating that its low Young's modulus provides enhanced bending resistance and flexibility, enabling it to maintain excellent optical performance even in complex wiring environments. This experiment confirmed that even when the fiber undergoes bending or deformation, the transmission loss of the optical signal remains relatively low, and the signal stability is high. These findings present a new approach for clinical gait analysis, where the fiber's ability to retain its performance under bending conditions makes it a promising tool for monitoring human movement and posture in a non-invasive and reliable manner.

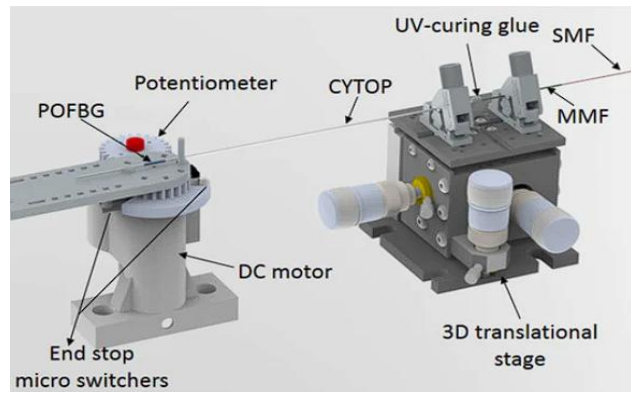


**Figure 7:** Experimental setup for characterizing the CYTOP fiber-based curvature sensor for human activity simulation [48]

Due to its superior chemical stability, Liu et al. [49] studied the Bragg grating performance of CYTOP and PMMA optical fibers under temperature variations. The results showed that, under a temperature change of 60 ° C, the wavelength shift of the CYTOP Bragg grating was less than 10 nm, much lower than that of PMMA, confirming its heat resistance stability. At the same time, the polymeric nature of POF makes it sensitive to humidity (RH). Andreas et al. [50] investigated the use of CYTOP polymer optical fiber Bragg grating (POFBG) sensors for relative humidity (RH) monitoring in concrete. The study showed that CYTOP polymer optical fibers exhibited excellent humidity responsiveness and, after being inscribed with FBGs using femtosecond laser technology, demonstrated excellent sensitivity to relative humidity, temperature, and strain. The experimental results showed that these polymer optical fiber sensors could accurately and stably monitor humidity changes over an eight-day period, demonstrating excellent performance in structural health monitoring. The humidity sensitivity of polymer optical fibers makes them ideal for humidity monitoring, offering a non-electromagnetic interference alternative to traditional electronic sensors, while being scalable and easy to install, making it ideal for monitoring critical parts of building structures. Even considering the few-mode characteristics of the fiber, the sensor response remained highly stable during testing.

Moreover, CYTOP's high biocompatibility makes it an ideal choice for the medical field. It has been widely applied in biomedical sensors and implantable devices to monitor physiological signals like heart rate and respiration. Sui et al. [51] developed FBG-based brain temperature sensor using CYTOP optical fiber. The sensor was fabricated by directly inscribing FBG on the fiber end-face using femtosecond laser technology, followed by packaging with waterproof materials, as shown in **Figure 8**. This sensor was verified to have low optical loss and high flexibility, achieving a measurement accuracy of 0.1 ° C. The sensor was able to measure brain temperature at multiple depths and showed a strong time correlation with body temperature fluctuations. The research indicated that the sensor could accurately measure temperature differences across different regions of the brain while effectively avoiding

interference from humidity and micro-strain. This study further promoted the use of CYTOP materials in biomedical sensing, particularly in medical devices that require high precision, flexibility, and biocompatibility.

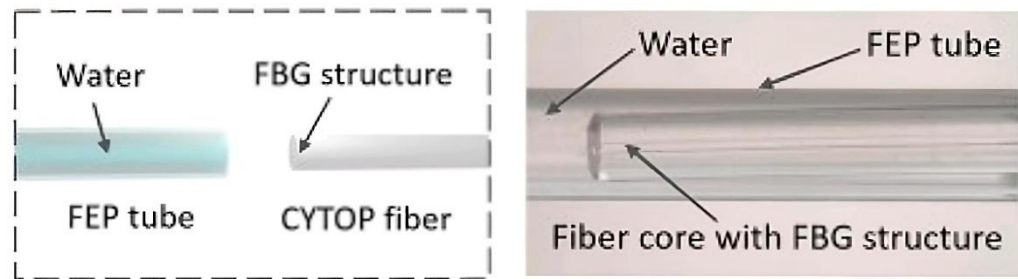


**Figure 8:** CYTOP fiber FBG brain temperature sensor unit [51]

Polymer optical fiber (POF) sensors have been studied for over 20 years. However, their practical application has been limited primarily due to high transmission losses. With the continuous advancement of technology, CYTOP optical fiber, with its exceptional properties, has minimized these losses, expanding the application range of POF. This development has opened up broad prospects for applications in fields such as health monitoring, intelligent sensing, and optical communication. As demonstrated in the current research, a rich variety of applications has been achieved. This paper will explore the application of CYTOP optical fiber in heart signal detection, leveraging its advantages for further research.

### 2.3 The Application of Femtosecond Laser Processing Technology in Sensor Fabrication.

The concept of femtosecond lasers dates back to the 1960s and 1970s, when the main focus of ultrashort pulse laser research was on how to generate shorter pulse widths. In 1981, R.L. Fork and his team at Bell Labs in the United States directly generated a 90 femtosecond pulse using a dye laser, marking the beginning of the femtosecond era, also known as the ultrafast era. A key breakthrough in femtosecond laser amplification occurred in 1985, when Gérard Mourou and his graduate student Donna Strickland proposed Chirped Pulse Amplification (CPA). This technique involves first stretching

femtosecond pulses to nanosecond durations, then amplifying them in a gain medium, and finally removing the chirp and compressing the pulses back to femtosecond durations. CPA solved the technical challenges faced in directly amplifying femtosecond pulses [52]. Since then, femtosecond laser technology has been widely applied in material processing, precision measurement, and biomedical fields.

The unique advantage of femtosecond lasers lies in their pulse width, which is typically in the range of  $10^{-15}$  seconds (1 femtosecond =  $10^{-15}$  seconds). This provides extremely high time resolution and precision, allowing for the release of large amounts of energy in very short time intervals, enabling precise control of the micro-processing of materials without inducing the thermal damage commonly seen in traditional laser processing. This makes femtosecond lasers widely used in material processing and micro-structure manufacturing [53].

In the sensor field, femtosecond lasers can be used for the precise fabrication of microstructures. For instance, in the production of optical FBG sensors, femtosecond lasers can precisely inscribe periodic structures in optical fibers due to the photosensitivity of the fiber material. This leads to the creation of high-quality fiber gratings, thereby enhancing the sensitivity and stability of the sensors.

Traditional FBG fabrication methods often use long-pulse lasers (such as UV or CO<sub>2</sub> lasers) to etch one-dimensional periodic refractive index modification regions within optical fibers. These methods typically require phase mask techniques to precisely modulate the laser beam into a specific grating pattern, which is then projected onto the fiber core to induce refractive index modulation. Using a phase mask allows for precise, low-error grating structures, making it an essential technique in FBG fabrication. However, the phase mask method has limitations in high-temperature environments and material flexibility. In contrast, femtosecond laser technology overcomes these limitations. The direct writing method for FBG fabrication using femtosecond lasers,

first published by A. Martinez et al [54]. In 2004, demonstrated a phase-mask-free approach suitable for a variety of fibers and application scenarios. The femtosecond laser direct writing method is efficient, requires low pulse energy, and can modulate grating parameters such as center wavelength, grating pitch, and length according to sensor requirements. The writing methods are typically divided into three types: point-by-point (P-b-P), line-by-line (L-b-L), and plane-by-plane (Pl-b-Pl) [55]. **Figure 9** below clearly illustrates the features of these three methods: (a) P-b-P; (b) L-b-L; (c) Pl-b-Pl. Each method has its advantages depending on the specific sensing requirements, achieved by adjusting laser parameters such as beam size, energy, scanning speed, and focusing mode.

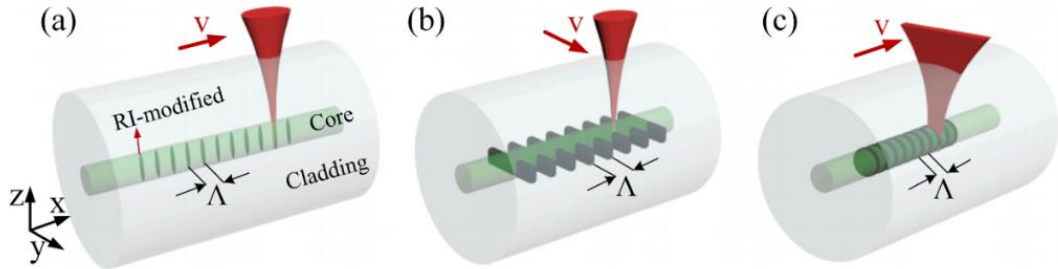


**Figure 9:** Different methods of femtosecond laser direct writing: (a) P-b-P; (b) L-b-L; (c) Pl-b-Pl [55]

The point-by-point (P-b-P) writing method is suitable for manufacturing high-precision gratings, especially for small-range optical fiber Bragg gratings (FBGs). It allows for the creation of detailed periodic structures. This method is ideal when precision is the primary concern, enabling the production of finely tuned grating structures with high accuracy; The line-by-line (L-b-L) method improves production efficiency and is suitable for manufacturing longer, more uniform FBGs. This approach balances precision with efficiency, making it easier to produce gratings with consistent characteristics over extended lengths. The operation is relatively simple compared to other methods; The plane-by-plane (Pl-b-Pl) method is designed for large-scale FBG production, particularly for applications requiring high throughput and consistency. This method allows for the rapid creation of high-quality grating structures, making it ideal

for multi-functional sensors or long-distance applications where large quantities of gratings are needed.

In a study by Graham D. Marshall et al. [56], they demonstrated a timing control system for point-by-point (P-b-P) FBG writing using femtosecond lasers, as shown in **Figure 10**. The system generates two trigger signals from a clock source: one main trigger signal and one delayed trigger signal. By adjusting the delay size and switching between the two trigger signals, they achieved precise control over the refractive index modulation position for each grating, thus enabling the accurate fabrication of the grating structure. By fine-tuning local phases, amplitudes, and spacing of the grating refractive index modulation, they were able to produce fiber gratings with complex transmission and reflection spectra, tailored to specific requirements;

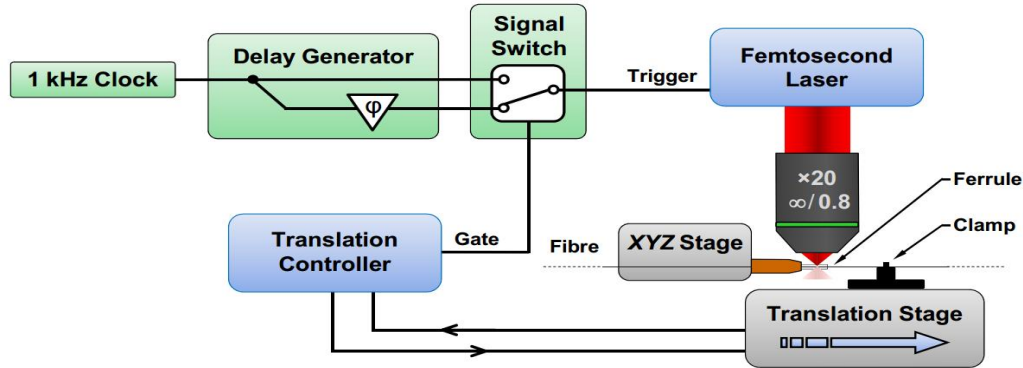


**Figure 10:** Timing control system for femtosecond laser P-b-P grating writing [56]

Femtosecond laser writing of FBGs (Fiber Bragg Gratings) demonstrates exceptional flexibility in controlling the position of each refractive index modulation (RIM), which is crucial for creating FBGs with complex refractive index distributions, such as apodized FBGs, chirped FBGs, and phase-shifted FBGs. He et al. [57] utilized line-by-line (L-b-L) femtosecond laser writing to manufacture apodized FBGs with suppressed side lobes. The L-b-L method was selected because, while individual laser pulses can form small RIM regions, the point-by-point (P-b-P) method is less suitable for manufacturing high-reflection FBGs in large mode field fibers. The L-b-L method has proven effective in expanding the RIM area [58].

In this work, He et al. controlled the length or lateral position of each laser-written index-modified path with precision, flexibly achieving various apodization modulation

curves, as shown in **Figure 11**. This L-b-L technique for apodization is an efficient and adaptable method for manufacturing FBGs with high side mode suppression ratio (SMSR), promising improvements in the performance of filters, fiber lasers, and sensors.

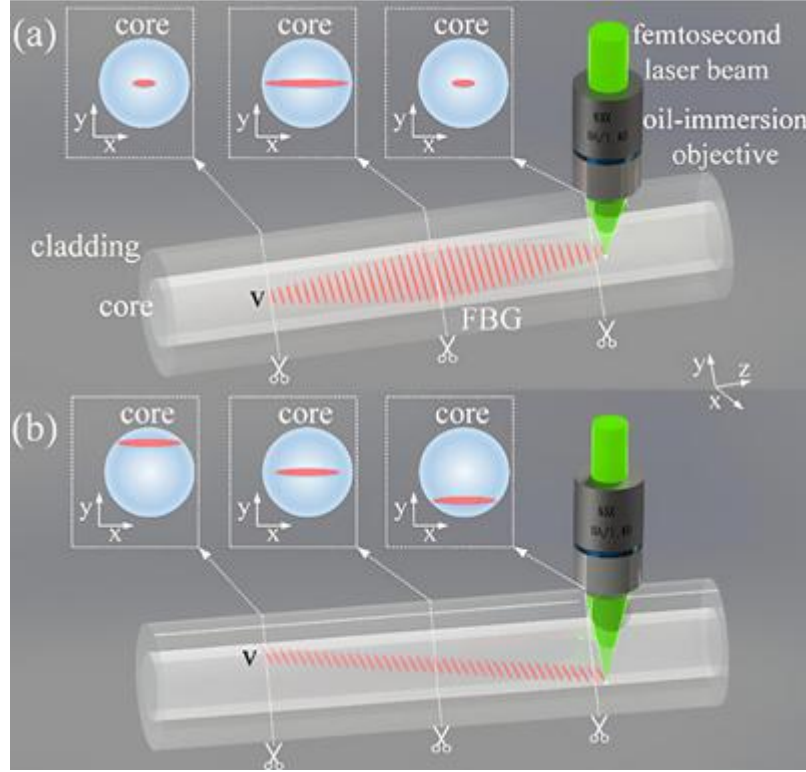


**Figure 11:** Schematic of two femtosecond laser L-b-L grating writing methods:

(a) controlling the track length; (b) controlling the track position [58]

The point-by-point (P-b-P) and line-by-line (L-b-L) methods are often time-consuming, requiring longer durations to fabricate a single grating. More importantly, the localized thermal effects generated by the concentrated energy in smaller regions during the process can result in certain signal losses. To address these issues, Duan et al. [59] proposed the use of the Pl-b-Pl (plane-by-plane) method, combined with slit shaping, for the fabrication of chirped fiber Bragg gratings (CFBGs) and chirped tilted fiber Bragg gratings (CTFBGs), as shown in **Figure 12**. In this method, a rotatable slit is added to the light path between the focusing objective lens, shaping the laser beam. This technique provides a broad modulation coverage across the fiber core, effectively mitigating loss and other issues. Additionally, it offers shorter writing times and higher efficiency compared to the P-b-P and L-b-L methods. This approach allows for more efficient manufacturing of complex and high-performance gratings.

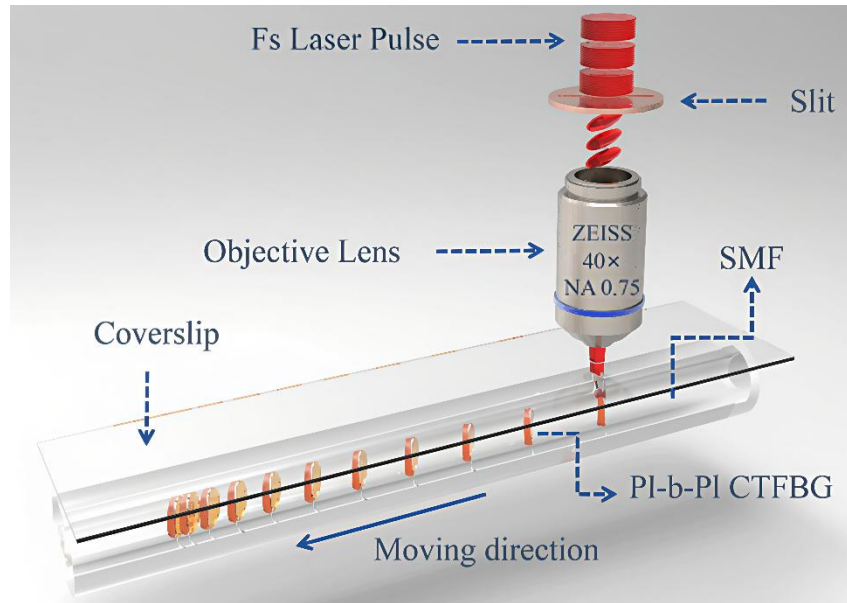


**Figure 12:** Schematic of femtosecond laser Pl-b-Pl method for creating CTFBG in single-mode fiber [59]

The application of femtosecond laser writing technology in polymer optical fibers (POFs) has been gaining increasing attention and exploration. In 2016, the Photonics and Optical Sensors Research lab team at Cyprus University of Technology proposed a strategy during the fabrication of FBGs, where they controlled the spatial dimensions of the grating within the core of the fiber. This strategy limited multimode excitation, enabling the creation of high-performance single-mode gratings. In recent years, the team has advanced the application of femtosecond laser processing technology in combination with the advantages of CYTOP optical fibers, bringing this technology into various sensing fields.

The team used multimode gradient-index CYTOP fibers and employed the plane-by-plane (Pl-b-Pl) femtosecond laser writing method. To minimize the number of fiber modes coupled into the grating, they confined the FBG's spatial extent to the peak of the gradient-index distribution at the center of the fiber core. By doing so, they excited the strongest low-order modes, leading to the generation of a single-peak POF-FBG spectrum. Experimental results indicated that compared to traditional silica-based optical fiber FBG sensor arrays, the polymer fiber-based sensors demonstrated significantly improved sensitivity to dynamic strain [60].

The team also leveraged the gamma radiation sensitivity of CYTOP materials to explore the potential of femtosecond-laser-processed CYTOP FBG sensors for use in harsh radiation environments. Research showed that these CYTOP-based FBG sensors could operate stably in high-radiation environments, offering broad application prospects, particularly in nuclear energy, waste storage, and medical fields. By validating their performance in these extreme conditions, the team further confirmed the reliability of these sensors, providing a new technological approach for future industrial and environmental monitoring [61].

## 2.4 The Application of 3D Printing Technology in Sensors

3D Printing (Three-Dimensional Printing) is an additive manufacturing technology that constructs three-dimensional objects by layer-by-layer material deposition. First introduced by Charles Hull in the 1980s, he invented Stereolithography (SLA) technology and patented it in 1986. Over time, 3D printing evolved into several types, including Fused Deposition Modeling (FDM), Selective Laser Sintering (SLS), and Electron Beam Melting (EBM). Today, 3D printing has become a driving force in personalized manufacturing and rapid prototyping due to its advantages in production flexibility, material waste reduction, and shortening product development cycles.

Recent advancements in 3D printing technology, particularly in sensor structures, have shown significant progress. This technology enables the precise creation of complex and customized sensor structures, catering to personalized needs while also allowing efficient mass production. In the field of medical sensors, 3D printing can manufacture sensors with specific geometries, microstructures, or biocompatibility requirements. Furthermore, 3D printing plays a crucial role in sensor packaging, structural optimization, and the integration of sensor systems. For example, 3D-printed multifunctional sensor housings and packaging materials can greatly enhance the flexibility, adaptability, and anti-interference properties of sensors. Moreover, 3D printing can be used to create testing devices that closely match real-world conditions,

enabling experiments and validations under more realistic scenarios. As 3D printing materials and technologies continue to advance, their application in sensor manufacturing will become even more widespread, driving sensors toward miniaturization, higher performance, and multifunctionality.

An example of this is the work of M. Fajkus et al. [62], who used 3D printing technology to encapsulate a FBGsensor between two layers of MRI-compatible material, Acrylonitrile-Butadiene-Styrene (ABS), as shown in **Figure 13**. This specially encapsulated sensor was used to monitor vital signs on the chest. It was designed to detect strain and temperature dependence, and its measurements were compared to traditional ECG standards over extended trials. According to the Bland-Altman (B-A) method of objective analysis, the results demonstrated that the sensor had high reliability ( $>95\%$ ) for cardiac activity monitoring. Given its use of a single optical fiber cable, easy implementation, compact size, and light weight ( $<5g$ ), the sensor offers an alternative to traditional ECG systems in strong magnetic environments.

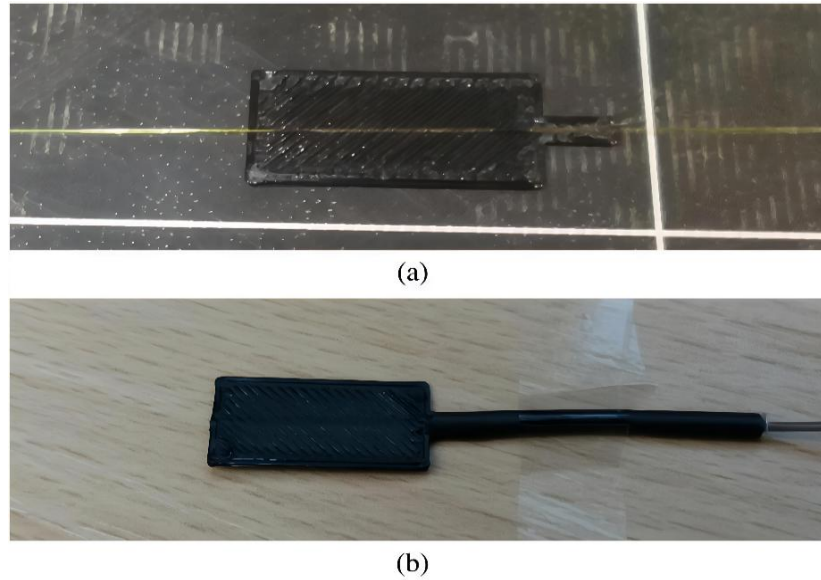


**Figure 13:** Sensor packaging: (a) placing the FBG on the ABS lower layer; (b) reprinting and curing the encapsulated FBG sensor [62]

Wagner Coimbra et al. [63] conducted a concept verification using a 3D-printed human maxillary biomechanical model, introducing a method for strain measurement during Rapid Maxillary Expansion (RME) using FBG sensors. The Hyrax expander (an orthodontic device) provided the forces needed for maxillary expansion, which were transmitted through metal wires to the teeth. As shown in **Figure 14**, the FBG sensors were attached to the posterior arms of the device for strain measurements.

The measurements focused on strain accumulation and the viscoelastic strain patterns during the RME process. It was observed that the strain increased with the number of activations of the Hyrax expander, while the strain rapidly decreased between activations. This study highlights the use of FBG sensors for the instrumentation of the Hyrax expander, which contributes to clinical research on the biomechanics and efficiency of RME. This approach could facilitate improvements in RME treatments and the development of new procedures.

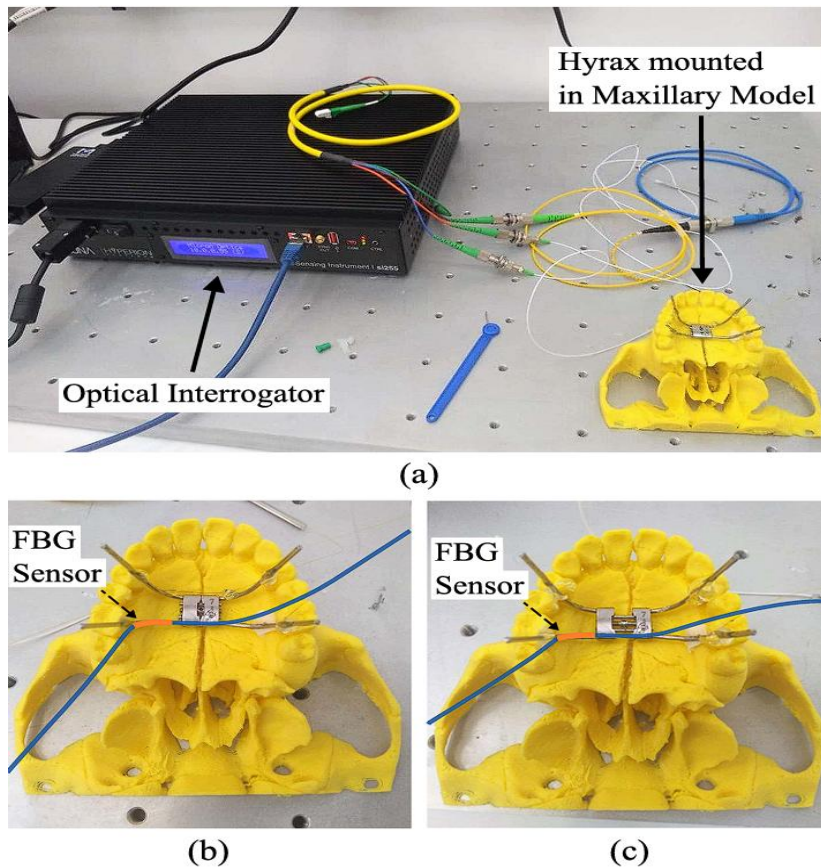


**Figure 14:** 3D-printed maxillary model: (a) FBG sensor demodulation system; (b) Hyrax expander before activation; (c) Hyrax expander after activation [63]

## 2.5 The Application of Polymer Materials in Packaging.

Polymeric materials play an essential role in sensor technology due to their unique physical and chemical properties. Compared to traditional materials, polymers offer excellent processability, flexibility, and multifunctionality, making them particularly advantageous in sensor design and fabrication. The use of polymeric materials in sensors dates back to the early 20th century, and with continuous advancements in material science and technology, the performance and variety of polymers have expanded, driving the evolution of sensor technologies.

Currently, polymeric materials are widely used in various types of sensors, such as pressure sensors, temperature sensors, and biosensors. Their main advantages lie in enabling lightweight and flexible sensors, which are especially important for wearable devices and portable electronics. Among these polymers, Polydimethylsiloxane (PDMS), known for its excellent properties, including liquid flexibility, high transparency, and biocompatibility, has proven particularly effective in biomedical and flexible sensor applications. As technology advances, the range of applications for PDMS continues to expand, covering sensors for pressure, temperature, and humidity.

Yi et al. [64] proposed a PDMS-coated fiber optic interferometer for temperature monitoring. The sensor, as shown in **Figure 15**, is constructed with a single-mode fiber - no-core fiber (NCF) - single-mode fiber cascading structure, coated with PDMS. The PDMS coating enhances the temperature sensitivity due to its excellent thermal properties compared to pure silica fiber interferometers. Additionally, the coating provides effective protection to the inherently fragile fiber structure, improving the sensor's reliability in practical applications. Experimental results demonstrated that the low-cost PDMS-coated fiber interferometer exhibited high sensitivity ( $200.2 \text{ pm}/^\circ\text{C}$ ) for temperature measurements. The sensor showed excellent consistency and repeatability during thermal cycling from  $40^\circ\text{C}$  to  $80^\circ\text{C}$ , confirming its potential for precise and reliable temperature monitoring.

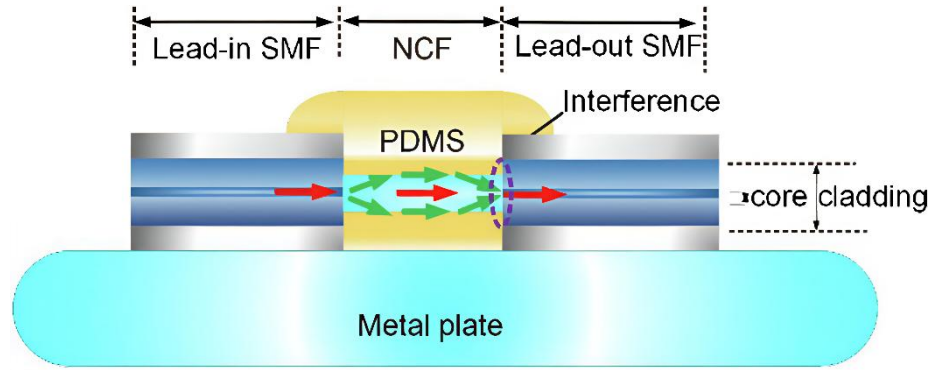


**Figure 15:** PDMS-coated single-mode fiber – no-core fiber – single-mode fiber (SMF-NCF-SMF) structure [64]

Cui et al. [65] developed a non-destructive fiber optic pressure sensor by combining two different proportions of PDMS as a substrate with single-mode fiber (SMF), as shown in **Figure 16**. The sensor design utilizes the radial elastic deformation of PDMS when external forces are applied. This deformation results in a larger elastic compressive deformation within the sensor, driving the fiber to undergo significant axial elastic deformation, thereby enhancing the optical sensitivity of the fiber. Additionally, the flexible PDMS encapsulating the exposed fiber significantly improves the environmental adaptability of the fiber optic sensor. Compared to sensors wrapped in a single proportion of PDMS, this design results in higher minimum pressure resolution and spatial resolution, making it a more sensitive and versatile solution for pressure sensing applications.

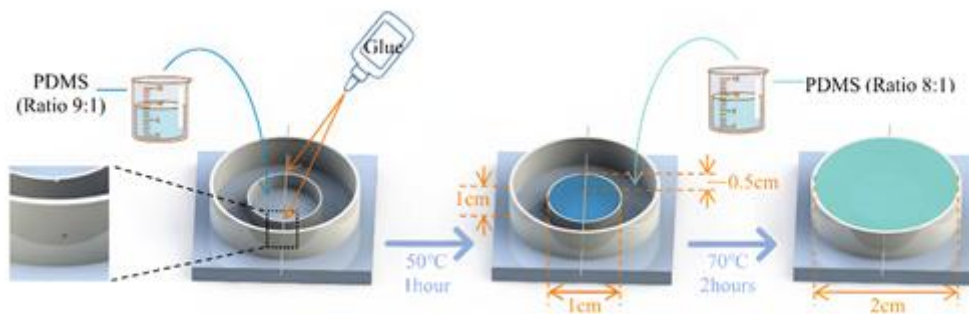


**Figure 16:** Fabrication methods for pressure sensors combining SMF with PDMS in different ratios [65]

Zha et al. [66] utilized PDMS material in combination with fiber optic sensors to achieve cardiopulmonary monitoring. The proposed stretchable elastomeric fiber optic sensor, as shown in **Figure 17**, is designed for the monitoring of RR and heart rate (HR). The study demonstrated that the elastomeric fiber optic sensor can synchronously measure RR and HR in various body positions, and successfully detect ballistocardiogram (BCG) signals while lying down. The sensor exhibited excellent accuracy and stability, with maximum errors of 1 bpm (for RR) and 3 bpm (for HR), an average weighted absolute percentage error (MAPE) of 5.25%, and a root mean square error (RMSE) of 1.28 bpm. Furthermore, the results from the Bland-Altman method indicated that the sensor showed good consistency in measuring RR through manual counting and HR through electrocardiogram (ECG).

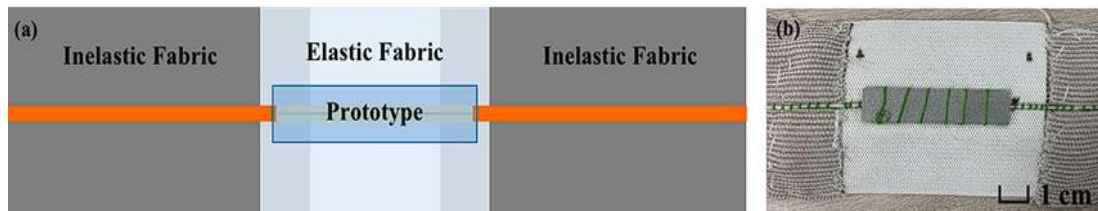


**Figure 17:** Elastic cardiopulmonary monitoring sensor made of PDMS material [66]

With the continuous development of new polymer materials and their processing techniques, future sensors are expected to achieve further breakthroughs in flexibility, intelligence, and multifunctionality. These advancements will provide more innovative solutions for biomedical, environmental monitoring, and other high-tech fields.

### **3 Research Theory and Methodology**

#### **3.1 Generation and Transmission of Cardiac Mechanical Signals**

The heart is the most vital organ in the human body, functioning as a pump to continuously drive blood circulation through rhythmic contractions and relaxations. During each cardiac cycle, several factors collectively determine the generation and characteristics of cardiac mechanical signals:

Firstly, the strong mechanical activity of myocardial cells, whose synchronization and contraction-relaxation rhythm directly influence changes in internal cardiac pressure. Secondly, the mechanical properties of the heart's structure, including the elasticity of the heart wall, the energy of valve closure, and the response characteristics of the pericardial system. Thirdly, the physiological feedback mechanisms of surrounding tissues and organs, such as the dynamic strain of subcutaneous soft tissues and the regulatory role of the vascular system. Finally, the neurohumoral regulation system optimizes cardiac function through precise temporal control and mechanical adjustments.

These factors work together to ensure the unique characteristics and stable transmission of cardiac mechanical signals. This complex physiological system not only ensures the efficiency of blood circulation but also provides rich information content for external sensing [67].

Specifically, the following factors play a key role:

- Synced contraction of the myocardium and hemodynamic effects**

When myocardial cells contract synchronously, the pressure within the heart chamber rises sharply, causing significant mechanical deformation of the myocardial wall. This deformation not only triggers the heart's own motion but also transmits signals outward through the cardiac tissue and pericardium. Additionally, during the ejection phase, the blood creates strong pulse waves, which generate shock effects at the interface between the blood and myocardium, further intensifying local mechanical vibrations.

These mechanisms collectively form the process of cardiac mechanical signal generation and propagation, ensuring the efficiency and stability of cardiac function. During the contraction phase, the pressure within the heart chamber increases dramatically, causing the myocardial wall to expand outward; during the relaxation phase, the myocardial wall returns to its original shape. This cyclic deformation guarantees normal cardiac output, maintaining functional coordination of other organs in the body through the transmission of mechanical signals and pulse waves. This dual effect allows the heart to not only effectively pump blood throughout the body but also dynamically meet the tissue's demands for oxygen and nutrients.

### ● Valve Motion and Local Vibrations

Valve motion and local vibrations are important physical phenomena in cardiovascular system monitoring, reflecting the spatial characteristics of heart activity and its physiological state. The impact at the moment of valve closure generates a typical high-frequency, transient vibration, primarily resulting from the collision between the heart valve and the heart chamber wall. This shock wave is transmitted through the chest, subcutaneous tissues, and skeletal system to the body surface, creating subtle signal changes with specific frequencies. The characteristics of these signals not only reflect the mechanical parameters of heart activity but also provide valuable information about the heart's functional state.

Furthermore, local vibration phenomena involve the inherent resonant properties of the heart and its surrounding structures. Under the impact of pulse waves, these structures produce responses at their specific resonant frequencies. This resonant signal can capture dynamic state changes in the tissues within the heart chambers, valves, and related organs, enriching the assessment of cardiac function. By analyzing these complex vibration patterns, a deeper understanding of cardiac perfusion, myocardial metabolic activity, and early signs of heart disease can be gained, providing a basis for clinical diagnosis and intervention.

### ● Tissue Conduction Effects

The mechanical signals generated by the heart must undergo a series of complex physical processes before being transmitted to the body surface. This process involves the coupling and conduction through multiple layers of tissue, including the pericardium,

chest muscles, ribs, and subcutaneous tissue. Each tissue layer has unique elastic properties and damping effects, which significantly impact the signal's amplitude, temporal characteristics, and spectral distribution. As a result, the signal gradually attenuates and filters during transmission, leading to a reduction in the amplitude detected at the body surface.

Nevertheless, these signals, after passing through multiple tissue layers, still retain important information related to the different phases of the heart. Specifically, the temporal shape of the signal can reflect major physiological activities of the heart, such as isovolumetric contraction, rapid ejection, and isovolumetric relaxation. This characteristic differentiates SCG from standard BCG in clinical settings, as SCG exhibits unique signal features. Due to tissue attenuation and filtering effects, the amplitude of SCG is typically lower, but its temporal information offers higher resolution. This makes SCG highly valuable in assessing cardiac function, detecting myocardial metabolic abnormalities, and identifying early signs of heart disease. In contrast, traditional BCG primarily reflects overall cardiac movement, while SCG captures more detailed physiological changes, providing richer and more unique cardiac information for clinical diagnosis.

## 3.2 Characteristics and Sensing Principle of Fiber Bragg Grating (FBG)

### 3.2.1 Basic Structure and Transmission Characteristics of Optical Fiber

Optical fiber, short for optical waveguide fiber, is a medium waveguide that operates in the optical wavelength range. Typically cylindrical in shape, it confines the optical energy—converted from electrical or electromagnetic energy—within its interface and guides light waves along the waveguide axis. The transmission characteristics of optical fiber are determined by its structural materials and mode distribution.

As shown in **Figure 18**, the basic structure of an optical fiber consists of three main components: the core, the cladding, and the protective layer. The core, located at the center, is responsible for transmitting optical signals. The cladding surrounds the core and has a lower refractive index, enabling total internal reflection. The protective layer,

positioned on the outermost part, enhances the mechanical strength of the fiber and shields it from external environmental influences.

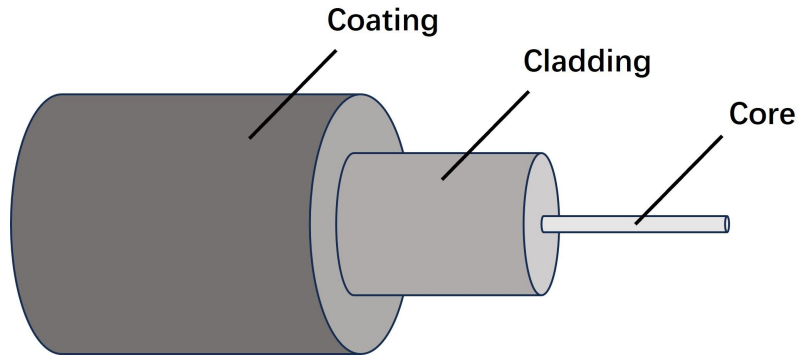


**Figure 18:** Optic Fiber Foundation Structure

The basic operating principle of optical fiber relies on the phenomenon of total internal reflection. Taking step-index fiber as an example, as shown in **Figure 19**,  $n_0$  represent the refractive index of the surrounding air,  $\theta_c$  is the critical angle for total internal reflection of a meridional ray within the core,  $\theta_i$  and  $\theta_t$  represent the incident angle and refracted angle, respectively, when light enters the core from the air.

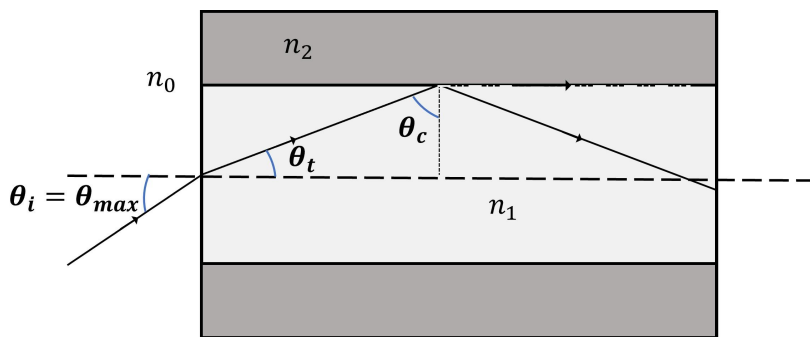


**Figure 19:** Light Propagation in Optical Fiber

According to Snell's Law, when a light wave passes from a higher refractive index medium (core) into a lower refractive index medium (cladding), the following condition is satisfied:

$$\sin\theta_c = \frac{n_2}{n_1} = \sin(90^\circ - \theta_t) = \cos\theta_t \quad (1)$$

For the interface between air and the core:

$$\frac{\sin\theta_{max}}{\sin\theta_t} = \frac{n_1}{n_0} \quad (2)$$

Under these conditions, the light wave will not refract into the cladding but will be totally reflected back into the core. This total internal reflection allows the light to propagate continuously within the core without any energy leakage.

Additionally, optical fibers can accept incident light within a certain range, which is described by the Numerical Aperture (NA):

$$NA = n_0 \sin \theta_{max} = \sqrt{n_1^2 - n_2^2} \quad (3)$$

For fibers in air (assuming the external refractive index  $n_0 \approx 1$ ), the Numerical Aperture can also be used to calculate the maximum acceptance angle:

$$\theta_{max} = \arcsin(NA) \quad (4)$$

Light can only effectively enter the core and propagate within the fiber if the incident light's angle does not exceed this maximum value. Therefore, using the principle of total internal reflection, the fiber can firmly confine the electromagnetic wave energy, in the form of light, within the core and transmit it along the fiber's axis.

When the core of an optical fiber is comparable to the wavelength of the light wave, it is necessary to use wave optics theory for analysis. The light wave transmitted through the fiber, due to the refractive index discontinuity between the core and cladding (with the core refractive index  $n_1$  greater than the cladding refractive index  $n_2$ ), must satisfy certain continuity conditions at the boundary for the electric field components. This results in a series of discrete modes, each corresponding to a different electric field distribution and propagation characteristics, collectively referred to as "modes." The mode characteristics of an optical fiber directly affect its signal transmission capabilities. For example, single-mode fibers (SMF) support only one propagation mode, while multi-mode fibers (MMF) allow multiple modes to coexist.

The normalized frequency  $V$  is a dimensionless parameter related to the frequency of the light wave and the optical fiber structure. It is used to describe the number of modes that can be supported in the fiber. The definition is as follows:

$$V = \frac{2\pi a}{\lambda} NA \quad (5)$$

where:

- $a$  is the radius of the fiber core,

- $\lambda$  is the wavelength of the incident light,
- $NA$  is the numerical aperture of the fiber.

The normalized frequency directly determines the number of modes the optical fiber can support:

- When  $V < 2.405$ , the fiber operates in single-mode transmission, supporting only the  $LP_{01}$  mode (i.e., the fundamental  $HE_{11}$  mode).
- When  $V > 2.405$ , the fiber enters multi-mode transmission, supporting multiple modes of propagation.

### 3.2.2 Optical Properties of Fiber Bragg Gratings (FBG)

In 1978, Hill et al. first discovered the photosensitivity of optical fibers, laying the theoretical foundation for the fabrication of Fiber Bragg Gratings (FBG). They used ultraviolet lasers to irradiate the fiber, inducing periodic refractive index changes within the fiber, thus forming the FBG [68]. Its structure is shown in **Figure 20**.

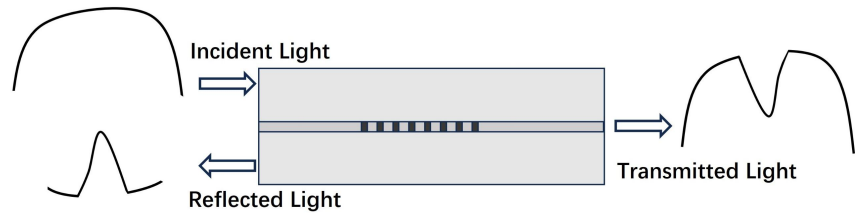


**Figure 20:** Structure of Fiber Bragg Grating

Fiber Bragg Grating is an optical waveguide with a periodic refractive index variation. The longitudinal refractive index changes lead to the coupling between different optical wave modes. This can change the spectrum of the incident light by partially or completely transferring the power of one fiber mode to another. In a single-mode fiber, the incident fundamental mode in the core can be coupled into both forward and backward propagating modes, depending on the grating and phase conditions determined by different propagation constants, as expressed by the equation:

$$\beta_1 - \beta_2 = \frac{2\pi}{\Lambda} \quad (6)$$

where  $\Lambda$  is the grating period,  $\beta_1$  and  $\beta_2$  are the propagation constants of modes 1 and 2, respectively (the constant  $\beta = \frac{2\pi n}{\lambda}$  describes the attenuation and phase shift of the electromagnetic wave during propagation). To couple a forward propagating mode into a backward propagating fundamental mode, the following condition must be met:

$$\frac{2\pi}{\Lambda} = \beta_1 - \beta_2 = \beta_{01} - (-\beta_{01}) = 2\beta_{01} \quad (7)$$

where  $\beta_{01}$  is the propagation constant of the transmission mode in a single-mode fiber. In this case, the fiber grating has a small period ( $\Lambda < 1\mu\text{m}$ ), and this short-period optical fiber grating is called a Bragg grating (FBG). It behaves similarly to an optical reflection filter, and the reflection peak wavelength is called the Bragg wavelength, denoted as  $\lambda_B$ , or the Bragg condition. When broadband light from a source propagates along the fiber to the FBG region, only the wavelengths that satisfy the Bragg reflection condition will be reflected back, while the others continue to propagate. The Bragg wavelength  $\lambda_B$  satisfies:

$$\lambda_B = 2n_{eff}\Lambda \quad (8)$$

where  $n_{eff}$  is the effective refractive index of the fiber. In another case, when a forward propagating mode is coupled into a backward propagating cladding mode,  $\beta_1$  and  $\beta_2$  are of the same sign, and the fiber grating period is larger ( $\Lambda > 100\mu\text{m}$ ). This type of optical fiber grating is called a long-period grating (LPG), and it behaves as a band-stop filter with a stopband width ranging from ten to hundreds of nanometers.

### ● FBG in Cardiac Signal Measurement:

FBGs are primarily used to measure cardiac signals based on their strain effect. When an external force is applied to the optical fiber, causing it to stretch or compress, the grating period  $\Lambda$  and the effective refractive index  $n$  change, leading to a shift in the Bragg wavelength  $\lambda_B$ . This shift is directly related to the applied axial strain  $\epsilon$ , as expressed by:

$$\frac{\Delta\lambda_B}{\lambda_B} = (1 - p_e)\Delta\epsilon \quad (9)$$

where  $p_e$  is the effective photo-elastic coefficient of the fiber, which depends on the material of the fiber and is given by:

$$p_e = -\frac{1}{n} \frac{dn}{d\epsilon} \quad (10)$$

For example:

- **Silica optical fibers ( $\text{SiO}_2$ ):** These have a low photo-elastic coefficient and are very stable.
- **Polymer optical fibers (POF):** Due to their high elasticity, the photo-elastic effect is more prominent in polymer fibers than in silica fibers, and they have a higher photo-elastic coefficient.

A higher photo-elastic coefficient means greater sensitivity to strain and faster, more pronounced responses to external dynamic pressures or vibrations. This is why polymer optical fibers are widely used in wearable sensors, biomechanical monitoring, large deformations, dynamic pressure, and high-sensitivity applications. For example, **CYTOP** (perfluoro-polymer) fibers have a slightly lower photo-elastic effect than traditional POF but still significantly higher than silica fibers. However, their lower transmission loss characteristics make them outstanding in the visible to near-infrared spectrum, making them more suitable for stable, high-precision applications.

### 3.2.3 Coupled-Mode Theory of Fiber Bragg Gratings

External physical quantities such as strain, pressure, and temperature can alter the characteristic parameters of fiber Bragg gratings (FBGs), such as the grating period and the refractive index of the fiber material. Since the refractive index of an FBG varies periodically, this causes the energy of certain guided optical modes to couple into adjacent modes, leading to changes in the reflection peak and transmission spectrum. These spectral changes can serve as indicators of variations in external physical quantities.

Therefore, when analyzing the characteristics of FBGs, the coupled-mode theory is commonly employed. Coupled-mode theory is a fundamental method for studying FBGs, providing a detailed description of optical propagation and mode coupling in waveguide media. This theory offers a deeper understanding of how FBGs respond to different external influences, serving as a theoretical foundation for the design and application of FBG-based sensors [69].

- **Basic Assumptions of Coupled-Mode Theory**

The variation in the refractive index of a FBG can be expressed as:

$$n(z) = n_{eff} + \Delta n_{eff} \cos\left(\frac{2\pi}{\Lambda}z + \varphi(z)\right) \quad (11)$$

where  $\Delta n_{eff}$  is the modulation amplitude of the effective refractive index, and  $\varphi(z)$  represents the phase perturbation.

The optical field in the  $z$ -direction can be described as a superposition of forward and backward propagating modes:

$$E^T(x, y, z, t) = \sum_m [A_m(z)e^{i\beta_m z} + B_m(z)e^{-i\beta_m z}] e_m^T(x, y)e^{-iwt} \quad (12)$$

where  $A_m(z)$  and  $B_m(z)$  represent the mode amplitudes of forward and backward propagating waves along the  $z$ -axis, respectively;  $\beta_m$  is the propagation constant of the mode; and  $e_m^T(x, y)$  represents the transverse mode. This implies that, under ideal conditions, no energy exchange occurs between the core, cladding, and radiation modes, meaning they remain mutually orthogonal.

### ● Inter-Mode Coupling Equations

Due to the periodic variation in the refractive index of the grating, mode coupling occurs between forward and backward propagating modes. Based on Maxwell's equations and the wave equation theory, the coupled-mode equations can be expressed as:

$$\frac{dA_m}{dz} = i \sum_q A_q C_{qm}^T e^{i(\beta_q - \beta_m)z} + i \sum_q B_q (C_{qm}^T + C_{qm}^L) e^{-i(\beta_q + \beta_m)z} \quad (13)$$

$$\frac{dB_m}{dz} = -i \sum_q A_q (C_{qm}^T - C_{qm}^L) e^{i(\beta_q + \beta_m)z} - i \sum_q B_q C_{qm}^T e^{-i(\beta_q - \beta_m)z} \quad (14)$$

where  $C_{qm}^T$  represents the transverse mode coupling coefficient, and  $C_{qm}^L$  represents the longitudinal mode coupling coefficient. When the phase-matching condition (Equation 6) is satisfied, energy exchange between modes reaches an optimal state.

### ● Calculation of Coupling Coefficients

The coupling coefficient is a crucial parameter in Coupled Mode Theory (CMT), describing the energy exchange between modes. It is typically derived using Perturbation Theory and depends on the characteristics of fiber Bragg gratings (FBGs)

or coupled waveguide structures. The longitudinal and transverse mode coupling coefficients are given by:

$$C_{qm}^T = \frac{\omega}{4} \iint \Delta\epsilon(x, y, z) e_q^T(x, y) e_m^T(x, y) dx dy \quad (15)$$

$$C_{qm}^L = \frac{\omega}{4} \iint \Delta\epsilon(x, y, z) e_q^L(x, y) e_m^L(x, y) dx dy \quad (16)$$

where  $\Delta\epsilon(x, y, z)$  represents the medium perturbation. In practical scenarios,  $C_{qm}^T \gg C_{qm}^L$ , meaning that the longitudinal coupling coefficient has a negligible effect on inter-mode coupling. Additionally, during fiber grating fabrication, the refractive index of the cladding remains unchanged, and the core refractive index variation is small and uniform. The perturbation can be approximated as:

$$\Delta\epsilon(x, y, z) \approx 2n_{eff}\Delta n_{eff} \quad (17)$$

Thus, the coupling coefficient simplifies to:

$$\xi_{qm}(z) = \omega \frac{n_{co}}{2} \overline{\Delta n_{co}}(z) \iint_{core} e_q^T(x, y) dx dy \quad (18)$$

$$\kappa(z) = \frac{s}{2} \xi_{qm}(z) \quad (19)$$

where  $\xi_{qm}$  is the self-coupling coefficient and  $\kappa$  is the cross-coupling coefficient.

Under these conditions, the transverse mode coupling coefficient simplifies to:

$$C_{qm}^T = \zeta_{qm}(z) + 2k(z)\cos\left[\frac{2\pi}{\Lambda}z + \varphi(z)\right] \quad (20)$$

For a uniform fiber Bragg grating (Uniform FBG), the cross-coupling coefficient  $\kappa$  remains constant, allowing further simplification of the coupled-mode equations.

### ● Coupled-Mode Equations for Uniform Fiber Bragg Gratings

When a light beam enters a uniform fiber Bragg grating (FBG), coupling occurs between the forward and backward propagating modes that are symmetrically positioned around the central wavelength. This interaction is described by the coupled-mode equations:

$$\frac{dA}{dz} = i\xi^+ A(z) e^{i\delta_z - \frac{\varphi}{2}} + i\kappa B(z) e^{-i\delta_z + \frac{\varphi}{2}} \quad (21)$$

$$\frac{dB}{dz} = -i\xi^+ B(z) e^{-i\delta_z + \frac{\varphi}{2}} - i\kappa A(z) e^{i\delta_z - \frac{\varphi}{2}} \quad (22)$$

Here, the sub-coupling coefficient  $\xi^+$  is a DC component and is given by:

$$\xi^+ = \delta_d + \zeta_1 - \frac{1}{2} \frac{d\varphi}{dz} \quad (23)$$

The detuning parameter  $\delta_d$  describes the phase mismatch between the wave and the grating and is expressed as:

$$\delta_d = \beta - \frac{\pi}{\Lambda} = 2\pi n_{eff} \left[ \frac{1}{\lambda} - \frac{1}{\lambda_B} \right] \quad (24)$$

where  $\lambda_B$  is the Bragg wavelength, defined as the central wavelength when the fiber's effective refractive index variation is approximately zero.

Under the condition of no phase variation (i.e.,  $\frac{d\varphi}{dz} = 0$ ), the reflection coefficient RRR can be derived as:

$$R = \rho^2 = \frac{\sinh^2 \sqrt{\kappa^2 - (\xi^+)^2} L}{\frac{(\xi^+)}{\kappa^2} + \cosh^2 \sqrt{\kappa^2 - (\xi^+)^2} L} \quad (25)$$

If the self-coupling coefficient  $\xi^+ = 0$ , the maximum reflection coefficient of the fiber Bragg grating is given by:

$$R_{max} = \tanh^2(\kappa L) \quad (26)$$

The peak reflection wavelength is given by:

$$\lambda_{max} = \left( 1 + \frac{\Delta n_{eff}}{n_{eff}} \right) \lambda_B \quad (27)$$

Due to modulation depth variations,  $\lambda_B$  does not exactly equal  $\lambda_{max}$ . The reflection bandwidth  $\Delta\lambda_0$ , defined as the wavelength spacing between the first two zero-reflection points on either side of  $\lambda_{max}$ , is given by:

$$\frac{\Delta\lambda_0}{\lambda} = \frac{s\overline{\Delta n_{eff}}}{n_{eff}} \sqrt{1 + \left( \frac{\lambda_B}{s\overline{\Delta n_{eff}}L} \right)^2} \quad (28)$$

For weak and strong gratings, the bandwidth expressions simplify as follows:

$$\begin{cases} \frac{\Delta\lambda_0}{\lambda} \approx \frac{\lambda_B}{n_{eff}L} = \frac{2\Lambda}{L} \\ \frac{\Delta\lambda_0}{\lambda} \approx S \frac{\Delta n_{eff}}{n_{eff}} \end{cases} \quad (29)$$

For weak gratings, the refractive index change is negligible, and the bandwidth is primarily determined by the grating length. In contrast, for strong gratings, the

reflection bandwidth is significantly influenced by the refractive index modulation depth.

### 3.3 Demodulation Methods of FBG Sensors

The optical characteristics and coupled-mode theory of Fiber Bragg Gratings (FBG) explained earlier illustrate their core working principle: using the shift of the Bragg wavelength to sense changes in environmental parameters. When external factors such as temperature, strain, or pressure act on the grating, the spectral reflection characteristics of the FBG change. Therefore, accurate measurement of Bragg wavelength shifts enables monitoring of environmental parameters.

However, the output signal of an FBG sensor is an optical signal, while most applications require conversion into an electrical signal for analysis. Thus, accurate and stable demodulation of Bragg wavelength shifts is a critical aspect of FBG sensing systems.

FBG demodulation techniques primarily focus on wavelength measurement, i.e., efficiently and accurately detecting the central wavelength of the FBG reflection or transmission spectrum and converting its variations into corresponding physical quantities. Depending on specific application requirements, demodulation methods can be categorized into various types, including:

- **Spectrometer Demodulation**

The spectrometer-based demodulation method is the most direct approach for FBG demodulation. Its structure is shown in **Figure 21**, consisting of a Broadband Light Source (BBS), an isolator (which prevents back-reflected light from interfering with the laser source), and a circulator, which directs uniform spectral illumination to the FBG. The reflected (or transmitted) spectrum from the FBG is then analyzed using an Optical Spectrum Analyzer (OSA) or an integrated spectrometer-based demodulation instrument.

**Basic Principle:** When an FBG is subjected to external strain, temperature, or other influences, the Bragg wavelength shifts accordingly. By collecting the FBG spectrum using a spectrometer and detecting changes in the central wavelength, the corresponding physical quantity can be determined. With high-precision spectrometers, it is possible to

achieve picometer (pm)-level wavelength resolution, ensuring high-accuracy measurements.

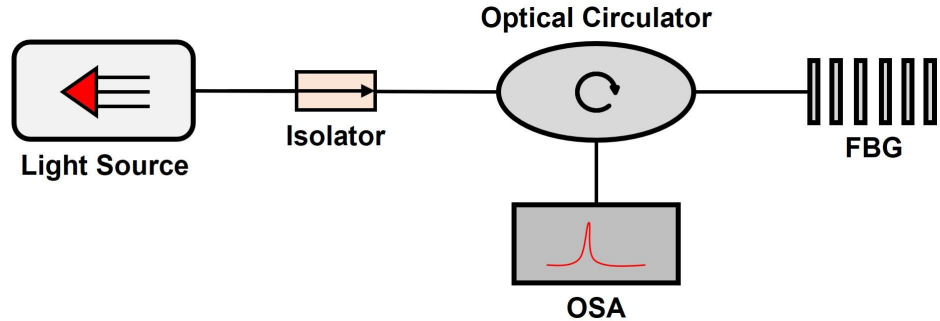


**Figure 21:** Schematic Diagram of Spectrometer Demodulation Method

The characteristics of this method are as follows: it offers high measurement accuracy, with the ability to achieve picometer (pm) level resolution using a high-resolution spectrometer; it is also suitable for multi-channel measurements, allowing multiple FBG sensors with different wavelengths to be measured and demodulated simultaneously in a single spectrum, making it suitable for distributed sensor networks. Additionally, this method is the most intuitive way to reflect spectral information, as it allows direct observation of the spectral changes of the FBG, which is useful for research and calibration. In recent years, the development of miniaturized, high-speed spectrometers has made spectrometer demodulation more widely applicable in portable measurements. Moreover, combining AI algorithms for spectral analysis can improve demodulation accuracy and signal resistance to interference.

### ● Edge Filter Demodulation

The edge filter demodulation method involves a demodulation structure as shown in **Figure 22**. It uses an edge filter with steep transmission characteristics to convert the FBG's wavelength shift into an optical intensity change. The intensity is then measured by a photodetector, and the Bragg wavelength shift is demodulated.

**Basic Principle:** The light reflected by the FBG passes through the edge filter, whose transmission rate varies with wavelength. When the Bragg wavelength of the FBG shifts, the intensity of the transmitted light also changes. By measuring the transmitted light intensity with a photodetector and using the filter's transmission curve, the wavelength shift can be inferred.

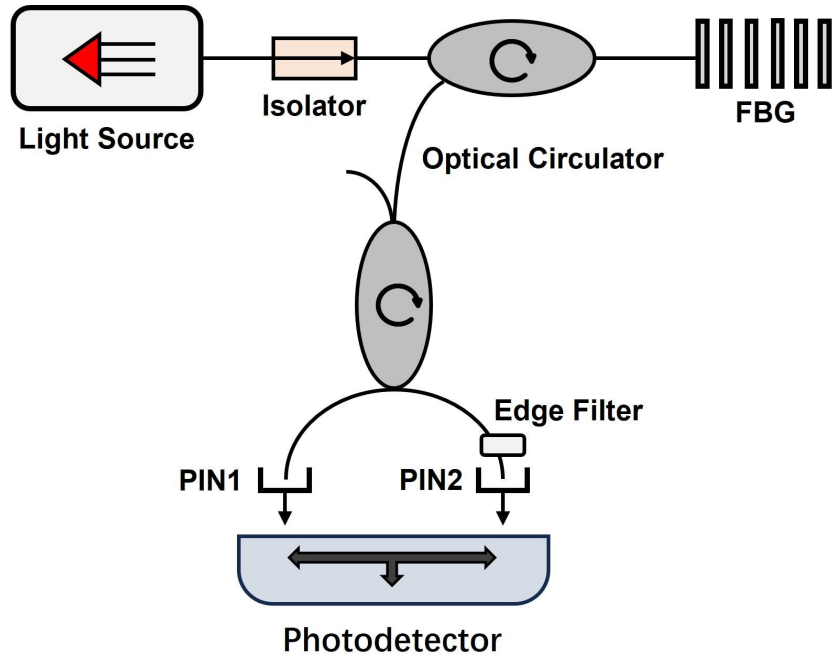


**Figure 22:** Schematic Diagram of the Edge Filter Demodulation Method

The edge filter method has better real-time performance. Compared to spectrometer-based demodulation, it enables high-speed signal detection, making it more suitable for dynamic measurements. Due to its simple system structure, it does not require a complex optical spectrum analyzer, relying only on a photodetector and a filter. This results in a compact setup with lower equipment costs, making it ideal for large-scale applications. With advancements in miniaturized optoelectronic components and signal processing algorithms, the edge filter demodulation method is being optimized for higher resolution and lower noise. Additionally, research on multi-channel multiplexing technology has expanded its capability to demodulate multiple sensing units simultaneously, broadening its application scope.

### ● Matched FBG Filter Method

The structure of the matched FBG filter method is shown in **Figure 23**. This method utilizes a reference FBG (Matched FBG) as a filter. When the Bragg wavelength of the sensing FBG shifts, the wavelength deviation is determined by comparing the transmission or reflection intensity changes of the matched FBG.

**Basic Principle:** A reference FBG with a known central wavelength is placed in the system, with its Bragg wavelength close to the initial wavelength of the sensing FBG.

When the Bragg wavelength of the sensing FBG shifts, a change in intensity occurs due to the spectral response of the matched FBG. A photodetector (PD) is used to measure the intensity variation, and signal processing algorithms are applied to demodulate the wavelength shift.

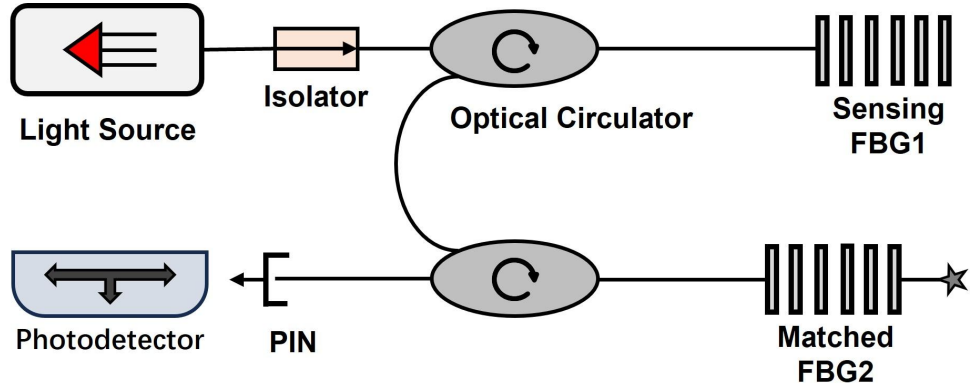


**Figure 23:** Schematic Diagram of the Matched FBGFilter Method

The spectral response of the matched FBG in the matched FBG filter method is similar to that of the measured FBG, enhancing demodulation accuracy. Since it does not involve mechanical moving parts and only requires a matched FBG as a filter, the system is compact and easy to integrate. Compared to demodulation methods based on tunable filters, this approach offers greater stability, making it widely used for long-term monitoring.

### ● Tunable Fabry-Perot Filter Demodulation

The Fabry-Perot (F-P) filter demodulation method utilizes a tunable Fabry-Perot interference filter (Tunable F-P Filter) as a wavelength selector to demodulate Bragg wavelength shifts by scanning the reflection or transmission spectrum of the FBG. The basic process is illustrated in **Figure 24**.

**Basic Principle:** The broadband light source (BBS) is incident on the FBG sensor. The reflected or transmitted light from the FBG enters the F-P filter, which has a tunable transmission peak. By adjusting the cavity length of the F-P filter (via voltage or piezoelectric drive), the transmission spectrum is scanned, and the intensity variations are recorded. Based on the transmission spectrum curve of the F-P filter, the Bragg wavelength shift of the FBG is calculated.

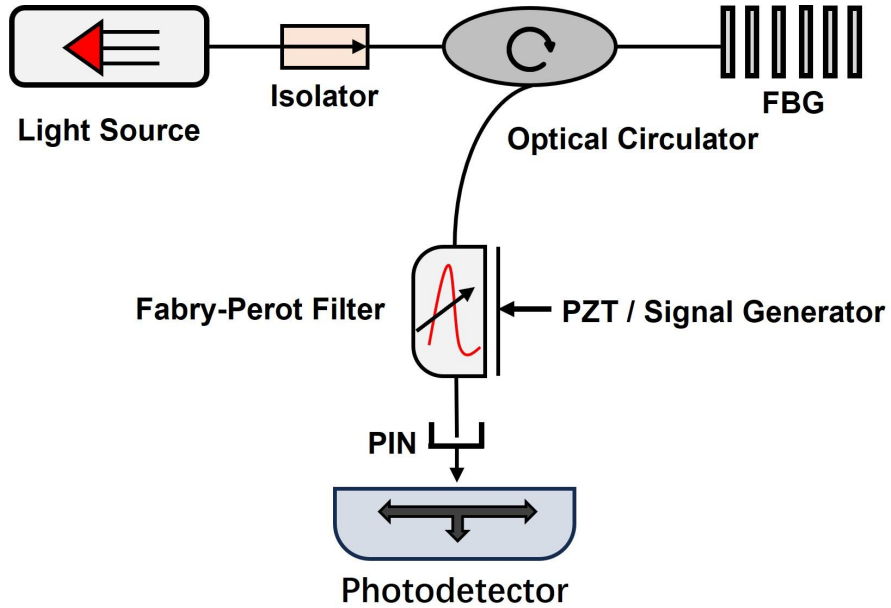


**Figure 24:** Schematic Diagram of Tunable F-P Filter Demodulation Method

This demodulation method enables high-resolution wavelength detection, as the narrowband transmission characteristics of the F-P filter allow for picometer-level wavelength demodulation. Compared to spectrometer-based demodulation, the F-P filter can perform wavelength scanning within milliseconds, making it suitable for dynamic measurements.

### ● Tunable Narrowband Light Source Demodulation

The FBG demodulation method based on a Tunable Narrowband Light Source (TNLS) is structured as shown in **Figure 25**. This method utilizes a tunable light source to gradually scan the reflection or transmission spectrum of the FBG and determines the Bragg wavelength based on the variation in transmitted or reflected optical intensity.

**Basic Principle:** The tunable narrowband light source scans the optical wave within a preset wavelength range. The FBG sensor exhibits high reflectivity only near its Bragg wavelength, while other wavelengths are transmitted. A photodetector (PD) monitors the intensity of the reflected or transmitted light. The signal processing system records the relationship between the light source wavelength and optical intensity, identifying the peak intensity corresponding to the Bragg wavelength. By calculating the shift in the Bragg wavelength, external physical parameters such as temperature and strain can be demodulated. .

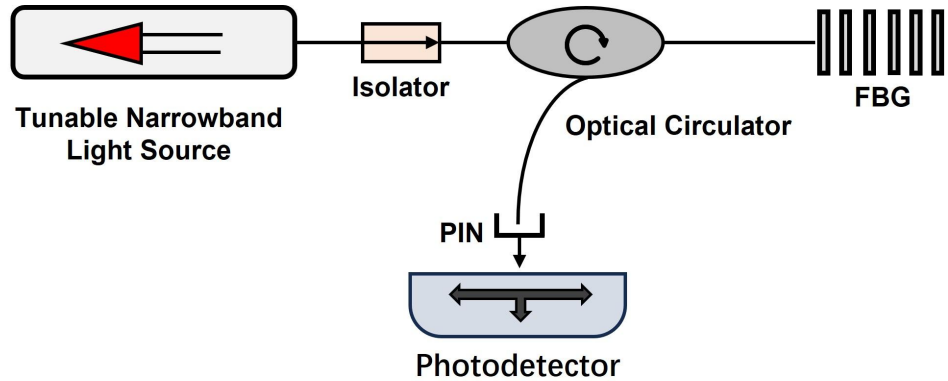


**Figure 25:** Schematic Diagram of Tunable Narrowband Light Source Demodulation

The advantages of a tunable laser include fast scanning speed, making it suitable for high-speed demodulation. It also offers high system stability and does not require a complex optical system, making it easy to integrate.

### 3.4 FBG Sensor Application Mechanism in Cardiac Signal Detection

The application of FBGsensors in cardiac signal detection primarily relies on capturing and demodulating the localized strain on the chest wall. The key steps and mechanisms mainly include the following two aspects: detection of the small deformation of the skin and signal demodulation and analysis. The key to accurately measuring cardiac signals is as follows:

- **Sensor Characteristics and Installation**

The FBG sensor can directly capture the small local skin strain caused by the mechanical vibrations generated by the heart when placed on the chest wall or skin surface. To achieve this, the sensor needs to adopt flexible packaging technologies, such as PDMS (Polydimethylsiloxane) or biocompatible polymer materials, to adapt to changes in the curvature of the human body and reduce motion artifacts.

The FBG sensor with a specially designed flexible package ensures good signal transmission performance by closely adhering to the skin. When precisely attached to the heart activity points (such as the left intercostal space, apex area, or above the sternum), the sensor can respond in real time to the tiny skin deformations caused by heartbeats, thus improving the sensitivity and accuracy of detection. In addition,

optimizing the fiber fixation method (e.g., 3D printed brackets or biological adhesive bonding) can further reduce signal drift and improve the stability of long-term monitoring.

### ● Data Preprocessing and Feature Extraction

Due to the effects of human motion, respiration, and external noise, the raw signals collected by the FBG sensor may contain a large amount of interference. To improve signal reliability, the following data processing methods are required:

- Band-pass Filtering: Remove low-frequency motion interference (below 0.5 Hz) and high-frequency environmental noise (above 100 Hz), retaining the main frequency range of the cardiac signal (1-50 Hz).
- Adaptive Filtering: Use signal decomposition techniques (such as wavelet transform or empirical mode decomposition, EMD) to separate cardiac activity signals from other noise components.
- Time-domain and frequency-domain analysis: After filtering the signal, peak detection and waveform segmentation are performed to extract the vibration characteristics of a single complete SCG signal. This allows for the calculation of physiological parameters such as heart rate.

Through these signal processing techniques, key feature parameters from different stages of the heart (such as isovolumetric contraction, rapid ejection, and isovolumetric relaxation) can be accurately extracted. This not only evaluates the basic pumping function of the heart but also assists in the early screening and remote monitoring of CVDs (such as valvular diseases, heart failure, and hypertension).

## 4 Fabrication of CYTOP Fiber FBG Sensors

### 4.1 CYTOP Optical Fiber and Fabrication Process of FBG

#### 4.1.1 Characteristics of CYTOP Optical Fiber

CYTOP is a specialized material derived from polytetrafluoroethylene (PTFE) which can be utilized as an optical fiber. With its outstanding physical, chemical, and optical properties, it demonstrates significant advantages across multiple fields. [70] Its unique molecular structure and material characteristics make it highly valuable in fiber optic sensing, communications, medical applications, and other high-precision fields.

- **Material Properties of CYTOP Optical Fiber**

Polytetrafluoroethylene (PTFE) features a highly fluorinated molecular structure, where each carbon atom is covalently bonded to four fluorine atoms, forming a stable molecular chain structure [71], as illustrated in **Figure 26**.

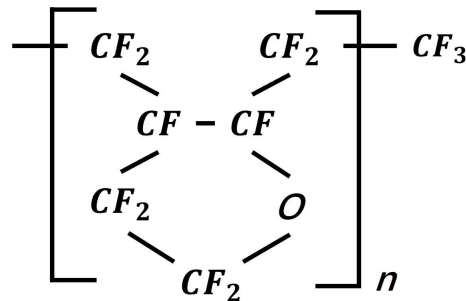


**Figure 26:** Chemical Structure of CYTOP Material

This unique chemical bonding structure endows CYTOP optical fibers with a range of distinctive material properties:

- **Low Optical Loss:** Due to the high electronegativity of fluorine atoms, CYTOP material exhibits minimal absorption of optical energy, maintaining low optical loss. This ensures that light signals experience minimal attenuation over long-distance transmission. CYTOP optical fibers demonstrate exceptionally low optical loss across the visible to near-infrared spectrum (approximately 400–1500 nm).
- **Broad Spectral Response:** CYTOP optical fibers exhibit broad spectral responsiveness, particularly in the visible and near-infrared regions. This

characteristic allows them to operate effectively under various light sources, making them suitable for diverse optical sensing applications.

- **Chemical Stability:** The strong electron-withdrawing effect of fluorine atoms results in a highly stable molecular chain, making the material resistant to chemical reactions. CYTOP exhibits outstanding corrosion resistance, enabling long-term operation in harsh environments such as exposure to acids, bases, and solvents.
- **Low Refractive Index:** The unique molecular structure of CYTOP results in a low refractive index, facilitating faster optical signal propagation and minimizing optical nonlinear effects. This low refractive index property enhances the fiber's sensitivity to minute environmental changes, making it particularly advantageous for optical fiber sensor applications.

### ● **Advantages of CYTOP Optical Fiber in Applications**

With its exceptional material properties, CYTOP optical fiber demonstrates significant value across various fields, including high-precision sensing, optical communication, medical monitoring, and industrial applications. Its low optical loss and broad spectral response make it an ideal choice for long-distance optical signal transmission and high-precision measurements, particularly in fiber optic sensors requiring high sensitivity. Additionally, CYTOP optical fiber boasts excellent chemical stability and corrosion resistance, enabling long-term operation in high-humidity, high-temperature, and highly corrosive environments, making it well-suited for demanding sensing applications. Its high mechanical strength and flexibility allow it to maintain reliable optical performance even under bending, stretching, or external force, making it widely used in wearable devices, flexible fiber sensors, and complex structural sensing systems.

- In the medical field, CYTOP optical fiber is well-suited for biosensing and in-body measurements due to its biocompatibility and outstanding optical properties. It can be used for detecting physiological signals such as heart activity, respiration, and other vital parameters. Its flexibility and stability make it particularly suitable for minimally invasive medical devices and wearable health monitoring systems, enabling accurate real-time data acquisition.
- In industrial applications, CYTOP optical fiber is extensively used in equipment health monitoring, industrial automation control, and safety warning systems due to its high-temperature resistance, chemical corrosion resistance, and mechanical

robustness. For example, in high-temperature and high-pressure pipeline inspections, structural health monitoring, and smart manufacturing systems, CYTOP optical fiber provides precise and stable sensing data, enhancing equipment safety and operational efficiency.

Moreover, the electrical insulation properties of CYTOP optical fiber effectively prevent electromagnetic interference, ensuring high stability even in complex electromagnetic environments. This makes it particularly suitable for sensing and communication systems requiring high anti-interference capability. In the field of optical communication, its ultra-low optical loss and broad spectral response characteristics provide an excellent solution for high-speed, long-distance signal transmission, playing a crucial role in next-generation fiber optic communication networks and high-speed data transmission systems.

In summary, CYTOP optical fiber, with its outstanding optical performance, stability, and environmental adaptability, has become a vital material in high-precision sensing, medical health monitoring, industrial detection, and optical communication. Its low loss, strong flexibility, corrosion resistance, and immunity to electromagnetic interference make it an ideal candidate for high-sensitivity, body-worn heart signal sensors. This study adopts CYTOP optical fiber for real-time, non-invasive, stable, and precise cardiac monitoring, providing a reliable technological foundation for heart health assessment.

#### **4.1.2 Fabrication Process of FBG**

After understanding the superior performance of the selected sensing material, CYTOP optical fiber, and its application value in high-sensitivity heart signal sensing, the key to achieving precise sensing lies in how to construct efficient and stable FBG in CYTOP optical fiber.

In fiber Bragg grating sensing, the fabrication process of the grating directly determines the performance of the sensor, including its center wavelength, reflectivity, and sensitivity to temperature, strain, and other parameters. Therefore, the method of writing the fiber Bragg grating into CYTOP optical fiber is crucial, as different writing techniques directly impact its optical properties and sensing performance. Currently, the writing methods for fiber Bragg gratings are mainly divided into internal writing and

external writing methods, with external writing methods including interference writing, point-by-point writing, and phase mask writing.

### ● Internal Writing Method

The internal writing method, also known as the internal standing wave method, is an early technique for writing fiber Bragg gratings, commonly used in ultraviolet (UV) exposure systems, especially for quartz optical fibers. This method creates an interference pattern inside the fiber to form standing waves. Due to the photosensitivity of the fiber material, the two-photon absorption effect leads to changes in the refractive index, thus forming the grating. The key to the standing wave method is generating periodic light intensity distribution inside the fiber through the interference between the laser and reflected light. These interference fringes cause periodic modulation of the refractive index in the fiber, resulting in the formation of the fiber Bragg grating. The advantage of this method lies in its ability to precisely control the grating's period and write it into the fiber with high quality. The most commonly used light source for the standing wave method is a UV laser, as UV light can effectively induce changes in the refractive index of the fiber.

### ● External Writing Method

#### 1. Interference Writing Method

The interference writing method is one of the most common external writing techniques. This method was first proposed by Meltz et al. [72], using the principle of interference to split the incident ultraviolet (UV) light into two coherent UV beams. These beams are then recombined to form an interference field that exposes the side of the photosensitive optical fiber, creating a periodic light intensity distribution in the fiber core. This induces localized changes in the refractive index of the fiber, forming the fiber Bragg grating. The main methods include amplitude splitting interference and wavefront splitting interference:

- Amplitude Splitting Interference Method

The amplitude splitting interference method uses a beam splitter or optical splitter to divide a laser beam into two or more beams. After propagating separately, these beams overlap on the fiber to form interference fringes, which then write the FBG (Fiber Bragg Grating). In experiments, *Kr-F* excimer lasers are often used as light sources, with high-

precision optical systems for beam splitting and angle control to ensure the stability of the interference fringes and the writing quality. A schematic diagram is shown in **Figure 27**. The incident light beam is split into two equal-amplitude beams by the splitter. The beams are then recombined in the target area of the fiber, forming an interference pattern. This induces a permanent refractive index modulation in the fiber core. The periodicity of the refractive index modulation depends on the angle between the two light beams, which can be adjusted using mirrors. The grating period matches the period of the interference fringes and is jointly influenced by the radiation wavelength  $\lambda$  and the angle  $\theta$  between the two intersecting light beams.

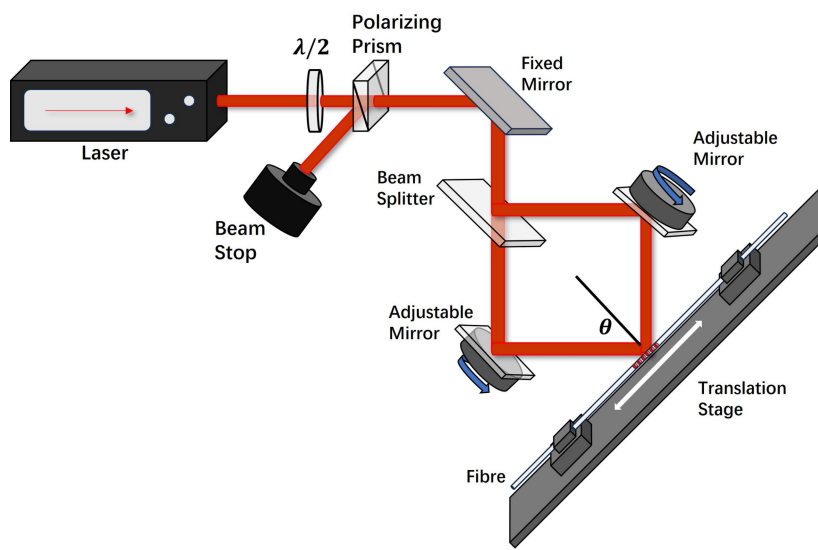


**Figure 27:** Schematic Diagram of the Amplitude Splitting Interference Method

Since the periodicity of the grating is determined by the interference fringes, the phase stability of the two light beams is crucial. However, this method is sensitive to mechanical vibrations and air disturbances, because the propagation paths of the two beams are relatively independent. Minor changes in the external environment may cause fluctuations in the optical path difference, leading to a drift in the interference fringes, which in turn affects the uniformity and precision of the grating writing. Therefore, this method requires high-precision optical alignment, particularly the stability of components such as beam splitters and mirrors, which must be high. Typically, experiments are conducted on optical vibration isolation platforms to reduce the effects of vibrations. Despite this, the method remains suitable for writing uniform FBGs (Fiber Bragg Gratings) and can precisely control the grating period.

- Wavefront Splitting Interference Method

To address the sensitivity of the amplitude splitting interference method to environmental disturbances, another method, the wavefront splitting interference method, can effectively reduce the system's dependence on mechanical vibrations and improve the stability of the interference fringes. This method divides the wavefront of the incident light beam into two or more parts, causing interference fringes to form on the fiber and writing the FBG. A common approach is to use the edge of a prism to split the beam into two equal parts, allowing them to propagate separately and form an interference pattern on the fiber surface. The primary advantage of this method is that it requires only one optical device (such as a prism), significantly reducing the sensitivity to mechanical vibrations and improving the stability of the system. Since all the beams come from the same wavefront, there is no independent propagation path, so there will be no fluctuations in the optical path difference that could cause fringe drift, thus improving the writing precision and repeatability. However, the limitation of this method lies in the supported grating length, which is mainly determined by the beam's half-width and is affected by the geometric size of the prism. Additionally, the tuning range of the Bragg wavelength is relatively small, and compared to the amplitude splitting interference method, this method has lower flexibility in manufacturing multi-wavelength gratings. In experiments, *Kr-F* excimer lasers are also used, and the wavefront is split by a prism to generate stable interference fringes for precise grating writing.

## 2. Point-by-Point Writing

Point-by-point writing is a method for fabricating fiber Bragg gratings (FBGs) by sequentially exposing the optical fiber to a focused light source along its axis. This process creates periodic refractive index modulation. A laser beam is focused onto the fiber surface through an optical system, inducing localized changes in refractive index and inscribing individual grating elements. After each element is written, the fiber is precisely translated by a distance corresponding to the grating period before the next exposure, continuing until the entire grating structure is formed. This technique dates back to 1990 when Hill et al. from the Communications Research Centre of Canada [73] successfully inscribed fiber gratings with a 590 nm period using a *Kr-F* excimer laser

(wavelength: 248 nm). Their work enabled mode coupling from fundamental to higher-order modes. However, the efficiency of UV-based inscription was relatively low, limiting broader application.

In recent years, the advancement of femtosecond laser technology has significantly improved the speed, precision, and flexibility of grating inscription [74]. Femtosecond laser pulses, characterized by their ultra-short duration (typically in the picosecond or femtosecond range) and high peak power, allow for precise refractive index modulation within the fiber core. Compared to conventional UV laser inscription, femtosecond lasers offer superior spatial and temporal resolution while minimizing thermal effects, thereby enhancing grating quality and stability. In my study, this femtosecond laser-based point-by-point writing method will be employed for sensor fabrication. The schematic diagram of the experimental setup is shown in **Figure 28**.

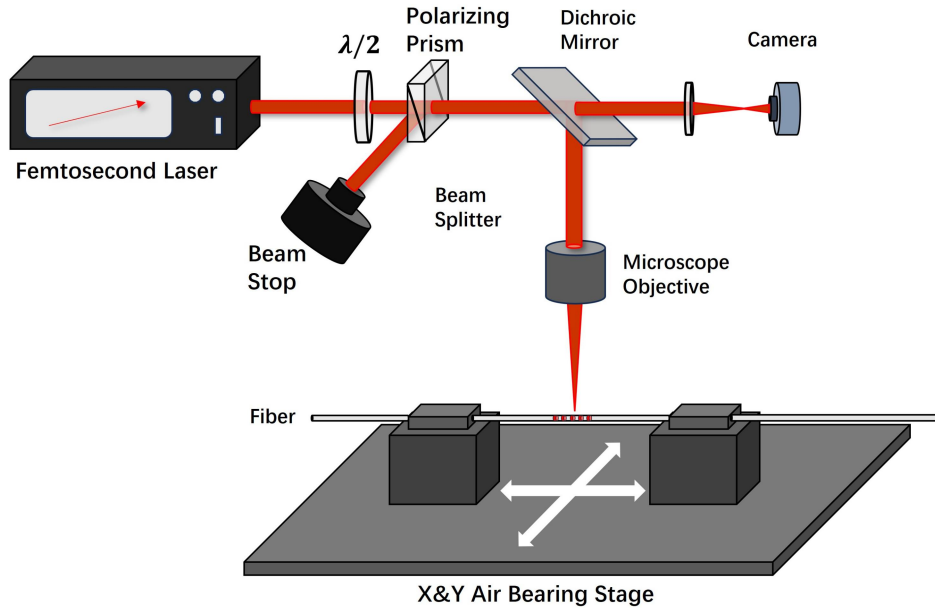


**Figure 28:** Schematic Diagram of Femtosecond Laser Inscription Method

The laser emitted from the laser source first passes through a tunable attenuator, which adjusts the laser intensity to ensure that the pulse power is suitable for grating fabrication. The adjusted laser beam then travels through a series of mirrors, including a dichroic mirror, which separates different wavelengths of light along the optical path. The laser is then precisely focused onto the fiber surface through a condenser objective,

with the focal position and spacing along the fiber axis determining the periodicity and phase of the grating.

During the inscription process, a pneumatic platform moves the fiber radially to control the grating period and overall length.

### 3. Phase Mask Writing

Similarly, the phase mask writing method is an efficient technique for mass-producing fiber Bragg gratings (FBGs), primarily using ultraviolet or femtosecond laser inscription. This method leverages the principles of diffractive optics, where a laser beam passes through a phase mask, generating periodic interference fringes that directly induce refractive index changes in the fiber core, thereby forming the grating structure. A schematic diagram is shown in **Figure 29**. Due to its simplicity, stability, and the elimination of complex interferometric optical systems, this technique is widely used for the large-scale fabrication of standard fiber Bragg gratings.

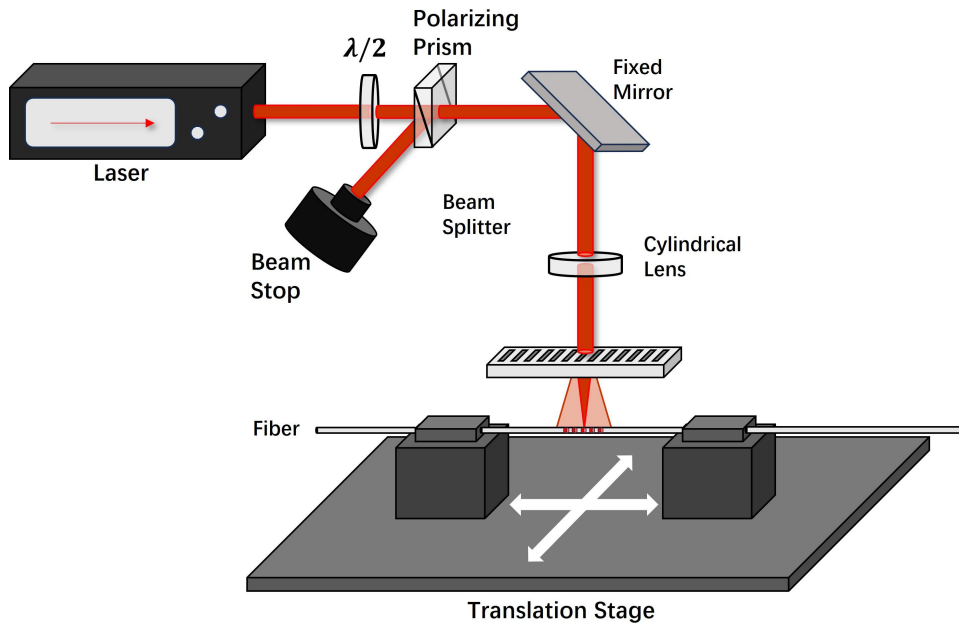


**Figure 29:** Schematic Diagram of Phase Mask Method

The greatest advantage of the phase mask method is that the period of the FBGs is determined solely by the period of the phase mask and the direction of the writing beam, independent of the beam's wavelength. This simplifies the fabrication process, ensures high repeatability and yield, and makes it well-suited for large-scale production. Compared to other techniques, the phase mask method has lower requirements for the

temporal coherence and monochromaticity of the light source. Additionally, the interference fringes formed by the near-field diffraction of the phase mask are independent of the beam's incidence position on the mask, making this method ideal for writing uniform, long-period gratings. It significantly reduces the complexity of the FBG fabrication system, as a single optical component can create strong and stable gratings, minimizing potential instability.

Although the phase mask method is less affected by geometric and temporal coherence compared to traditional interferometric techniques, spatial coherence remains crucial for ensuring high-quality gratings. To achieve maximum refractive index modulation, the fiber must be placed in close proximity to the phase mask. Thus, the distance between the fiber and the phase mask is a critical parameter in the writing process. This is especially important when using ultraviolet sources with poor spatial coherence, such as excimer lasers, where minimizing the fiber-to-mask distance is essential for maintaining writing quality and grating stability.

However, due to its reliance on a fixed mask pattern, the phase mask method lacks the flexibility of the point-by-point writing technique in customizing grating structures. Adjustments to the grating period and refractive index modulation distribution are limited, making it less suitable for fabricating finely tailored gratings that meet specific application requirements.

### ● **FBG Writing in CYTOP Optical Fiber**

In conventional silica optical fibers, ultraviolet (UV) exposure techniques are highly effective for fabricating high-quality fiber Bragg gratings (FBGs). This method relies on UV-induced refractive index changes in the fiber material, forming the grating structure within the fiber core. However, for CYTOP optical fibers, which are fluoropolymer-based, traditional UV inscription techniques encounter significant challenges. CYTOP fibers exhibit extremely low absorption in the UV range and possess poor UV photosensitivity, making it difficult to induce refractive index changes as effectively as in silica fibers. As a result, the application of UV-based inscription techniques in CYTOP fibers is considerably limited.

Femtosecond laser technology overcomes this limitation. Unlike UV inscription, femtosecond lasers utilize nonlinear multi-photon absorption to directly induce

refractive index modulation inside CYTOP fibers without requiring additional photosensitization treatments. This approach, leveraging ultra-short laser pulses, enables precise energy deposition within the fiber, facilitating high-resolution grating inscription while minimizing thermal effects and structural damage [75].

However, femtosecond laser inscription can lead to localized energy accumulation at both the surface and interior of the fiber. In CYTOP fibers, the point-by-point inscription method concentrates energy at discrete positions, which may result in unstable refractive index changes or even localized material damage. Moreover, achieving single-peak FBGs in multimode CYTOP fibers remains a challenge.

To address these issues, the Photonics and Optical Sensors Research lab at Cyprus University of Technology proposed the plane-by-plane femtosecond laser inscription method in 2017 [76]. This technique ensures more stable grating inscription in wide-core fibers such as CYTOP by uniformly distributing laser energy at each writing step, effectively avoiding the excessive local excitation and structural non-uniformities often associated with point-by-point inscription. It also enables precise refractive index modulation within a confined region of the fiber core, thereby optimizing coupling conditions and facilitating the generation of single-peak FBG spectra in CYTOP fibers. Moreover, this method allows for accurate three-dimensional control of the refractive index profile, enabling the fabrication of customizable grating structures that are difficult to achieve using conventional phase mask or interferometric approaches.

Owing to the mechanical flexibility of polymer optical fibers, the plane-by-plane inscription technique effectively minimizes cumulative errors and ensures uniformity in both fiber structure and refractive index. This results in the formation of more stable and higher-quality FBGs. By leveraging the unique optical and mechanical properties of polymer fibers, this method has enabled the broad development of polymer-based FBG sensors, which can be flexibly tailored to operate at any desired wavelength [77].

## 4.2 Fabrication of FBGs Using Femtosecond Laser Technology

The material properties of CYTOP fibers and the challenges of inscribing fiber Bragg gratings (FBGs) within them, as well as the analysis of common FBG inscription

techniques, were discussed in the previous section. The following section will detail the femtosecond laser inscription method we used for FBG fabrication and explore its experimental process and technical advantages.

In this experiment, we used the femtosecond laser system (HighQ Laser femtoREGEN), which has a central wavelength of 517 nm and a pulse duration of 220 fs. The laser beam is transmitted through a series of mirrors and is ultimately focused by a long working distance microscope objective (Mitutoyo, 50 $\times$ , NA 0.42), as shown in Figure 3.3. Meanwhile, a high-precision air-bearing translation stage (Aerotech) was used to hold and move the fiber, enabling accurate alignment with the laser focus.

The laser polarization is set to linear polarization during the experiment. To minimize inscription losses, visible light (517 nm) is selected. During the inscription process, the pulse energy is set in the range of 100–125 nJ/pulse, and the corresponding optical energy density (fluence) is calculated as follows:

$$F = \frac{E}{\pi r^2} \quad (30)$$

where  $E$  is the pulse energy, and  $r$  is the beam radius.

During preparation, the fiber samples to be processed are fixed on a glass slide and immersed in refractive index matching oil. Two auxiliary fibers are placed on either side of the target fiber to support a thin glass cover slip on top and to prevent jitter or displacement during processing, as shown in **Figure 30**. This setup effectively reduces lensing effects caused by the fiber's cylindrical geometry, thereby minimizing astigmatism and improving inscription precision. Moreover, since the refractive index of the matching oil closely approximates that of the fiber cladding, this method eliminates the need to remove the fiber coating and mitigates focal shift during focusing.

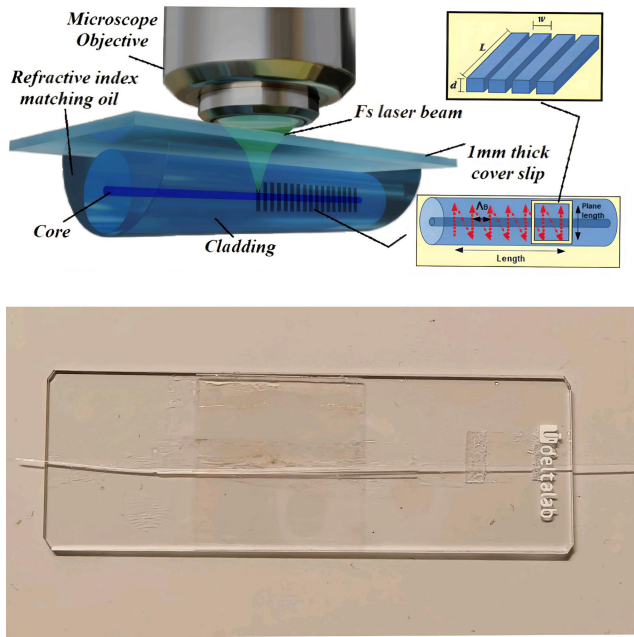


**Figure 30:** FBG Processing Fixture

The pulse energy is controlled via an adjustable attenuator, with a range from nJ to  $\mu$ J, and the repetition frequency is set by an internal pulse picker. During the plane-by-plane inscription process, the width of each inscription plane is set to R according to the type of fiber and experimental requirements. The inscription depth and length can be optimized by adjusting the parameters of the air-bearing platform to ensure the formation of a three-dimensional refractive index change region for the grating, as shown in **Figure 31**.

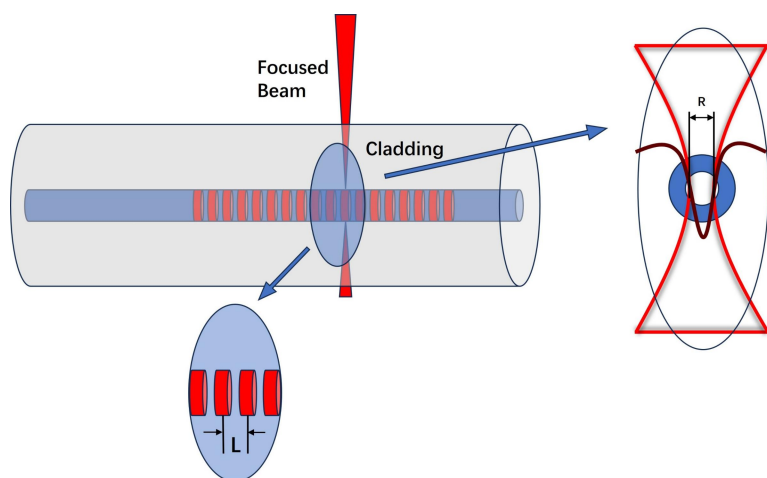


**Figure 31:** Schematic Diagram of Grating Inscription Structure

The movement of the air-bearing translation platform (Aerotech) during the entire inscription process is controlled by a computer, with synchronization programming using G-code. This setup allows for the inscription of complex trajectories, such as tilting and curves. The complete system is shown in **Figure 32**. The light beam path is illustrated in the diagram, with the red line indicating the propagation path of the laser from the light source to the microscope objective, and the green line representing the optical path of the camera.

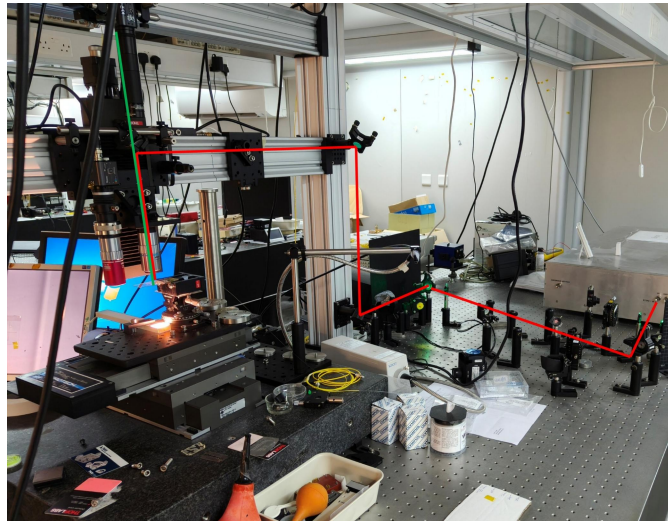


**Figure 32:** Complete Femtosecond Laser Processing System

The CYTOP optical fiber used in this experiment is manufactured by *Chromis Technology*, with a core diameter of 25  $\mu\text{m}$  and a graded refractive index profile (effective refractive index 1.34). The total diameter of the fiber is 250  $\mu\text{m}$ , and it is coated with a polycarbonate sheath to provide additional mechanical protection. Femtosecond laser pulses are generated by the HighQ femtoREGEN laser system (operating wavelength 517 nm, pulse duration 220 fs, repetition rate 2 kHz, pulse energy 20 nJ) and focused through a long working distance objective lens (50 $\times$  magnification, numerical aperture 0.42, Mitutoyo). The objective lens is less sensitive to fiber curvature effects, allowing for grating inscription without the need to remove the fiber's protective sheath. The inscribed FBG, shown in **Figure 33**, has a grating width of 5  $\mu\text{m}$ .

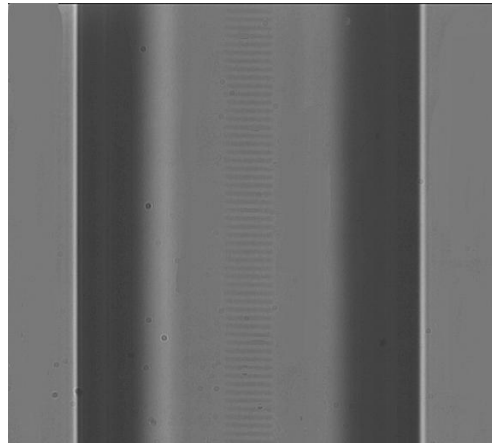


**Figure 33:** CYTOP Optical Fiber FBG (Pl-by-Pl Inscription)

Subsequently, the butt-coupling method was employed to connect the inscribed CYTOP polymer optical fiber (POF) to a standard single-mode silica fiber (SMF) equipped with an FC/APC output connector. As shown in **Figure 34**, the CYTOP fiber was first positioned at the center of the fiber coupling fixation stage, with its end face in direct contact with the cleaved facet of the SMF.

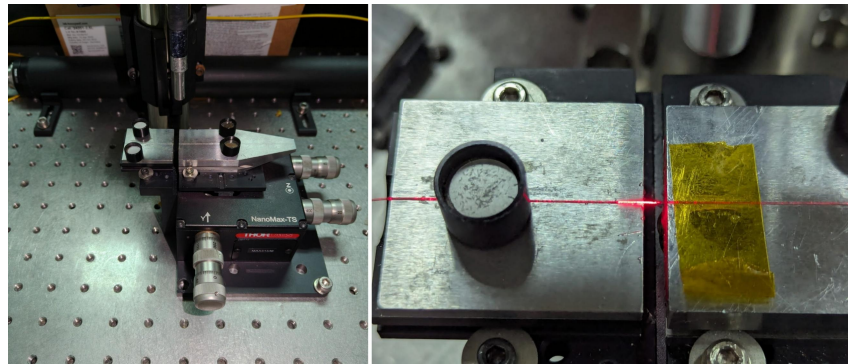


**Figure 34:** Experimental Setup of Fiber Butt-coupling.

To ensure stable coupling and minimize signal loss, a high-precision XYZ-axis micro-positioning stage was used to finely align and secure the two fibers in three dimensions, achieving optimal core-to-core alignment. At the same time, the SMF was connected to a spectrometer to enable real-time monitoring of the reflection spectrum from the CYTOP FBG, which guided the alignment process. Once a stable butt-coupling was achieved, UV-curable adhesive was applied at the interface and cured to ensure long-term mechanical stability.

This step is intended to facilitate selective excitation of the fundamental mode in the multimode CYTOP fiber by leveraging the smaller core diameter of the SMF. Compared with wider-core fibers, the more confined optical field output from the SMF allows for more efficient coupling into the fundamental mode of the CYTOP fiber while suppressing higher-order modes. As a result, the reflected signal exhibits improved purity and stability, and the adverse effects of mode mismatch are significantly reduced [78].

The reflection spectrum of the FBG inscribed in the CYTOP fiber is shown in **Figure 35**. The femtosecond laser system was configured to target a Bragg wavelength of 1550 nm, and a distinct reflection peak is observed at approximately 1550.78 nm, with a peak reflection power of around -20 dBm. The spectrum exhibits a high signal-to-noise ratio and a well-defined single-peak profile, indicating high inscription quality with minimal sidelobes and good spectral symmetry.

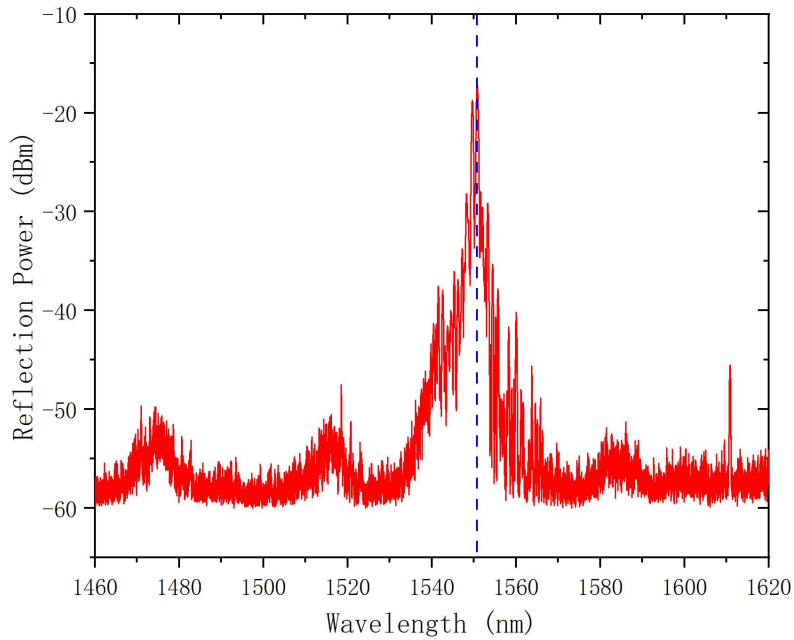


**Figure 35:** FBG reflection spectrum in CYTOP fiber

As a comparative experiment, Corning SMF-28 single-mode silica optical fiber was also used, with a core diameter of 8  $\mu\text{m}$ , a refractive index of 1.45, and an overall fiber diameter of 250  $\mu\text{m}$ . The same fabrication equipment was employed, but FBGs were

inscribed using the traditional point-by-point method with repetition rate 1 kHz, pulse energy 600nJ. This method was selected because SMF-28 is a Ge-doped silica fiber with strong UV photosensitivity, making point-by-point inscription sufficiently efficient. Furthermore, for SMF-28, which features a small core diameter of only 8  $\mu\text{m}$ , the point-by-point technique eliminates the need for complex procedures such as beam shaping and focus adjustment required to maintain uniform phase modulation. Instead, the grating structure can be accurately inscribed directly. The resulting FBG is shown in **Figure 36**. To achieve a Bragg reflection intensity (in dB) comparable to that of the FBG inscribed in the CYTOP fiber, multiple exposures were applied to the SMF fiber.



**Figure 36:** Silica Single-Mode Fiber FBG (P-by-P Inscription)

To meet the experimental requirements, three FBGs were inscribed along the SMF-28 silica fiber at 8 cm intervals, forming an FBG array. The femtosecond laser system was configured to target Bragg wavelengths of 1525 nm, 1550 nm, and 1575 nm. As shown in **Figure 37**, three distinct reflection peaks were observed at 1524.76 nm, 1549.01 nm, and 1573.54 nm, respectively. Through multiple exposure steps, all reflection peaks reached a peak power of approximately -20 dBm, achieving the desired reflection performance, which is comparable to that of the FBG in the CYTOP fiber. Each peak exhibits a high signal-to-noise ratio and a well-defined single-peak profile, indicating high inscription quality with minimal sidelobes and good spectral symmetry. The rationale for this wavelength configuration will be discussed in the following section.

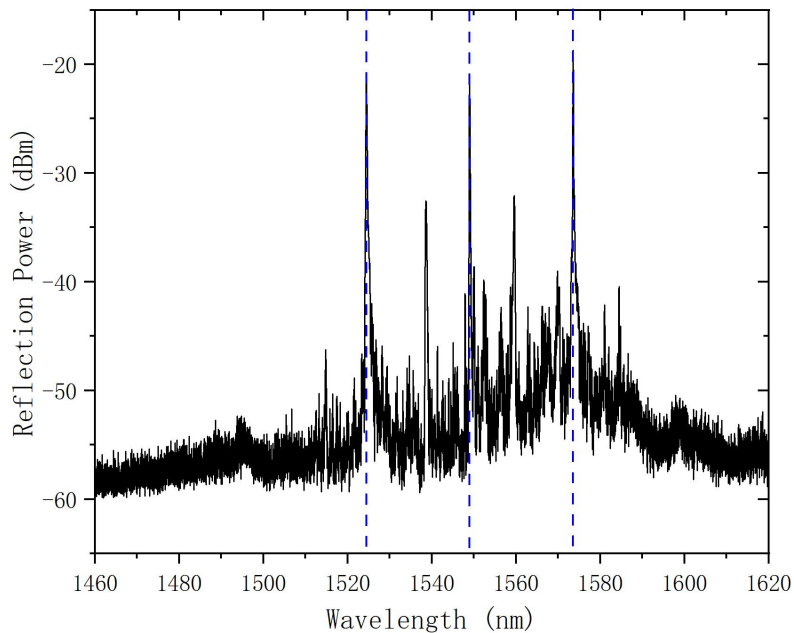


**Figure 37:** FBG reflection spectrum in SMF-28 fiber

### 4.3 Application of 3D Printing and Polymer Materials for Packaging

After the fabrication of the sensing unit, packaging it according to the specific application scenario is a critical step in transitioning FBG fiber sensors from theoretical research to practical applications. A well-designed packaging approach not only protects the optical fiber sensing element from external environmental disturbances, such as mechanical stress, humidity changes, and temperature drift, but also enhances the sensor's sensitivity and long-term stability, ensuring accurate and reliable data acquisition in various measurement environments.

To meet the requirements of heart signal monitoring, this study employs 3D printing technology combined with polymer materials for the packaging design of the FBG sensor.

The 3D printing system used in the experiment is the 30M laboratory-grade printer provided by **HYREL 3D**, which meets the required precision for the experiment. The modeling process is carried out using **Autodesk Fusion 360**, and the model is

subsequently sliced using **Repetrel** to generate a G-code file for controlling the printer platform.

The designed 3D-printed model is shown in **Figure 38**. The internal dimensions of the cavity are 80 mm × 36 mm × 4 mm. Three symmetrical grooves, each with a diameter of 0.3 mm and a depth of 1.6 mm, are embedded on both sides to secure the FBGs at the central position of the sensing unit.



**Figure 38:** Sensor Packaging Substrate Model

During the 3D printing process, preparation of the PDMS material was carried out. The PDMS used in this experiment was SYLGARD® 184 silicone elastomer. The detailed procedure is shown in **Figure 39**.

First, the base and curing agent were mixed at a mass ratio of 10:1. Based on the mold volume, a total of 55 g of PDMS was prepared, consisting of 50 g of base and 5 g of curing agent. The components were thoroughly stirred after mixing to ensure uniformity and stable material performance.



**Figure 39:** PDMS Material Preparation Process

To improve the quality of the PDMS, a vacuum chamber can be used to remove air bubbles generated during the mixing process. This helps reduce internal defects after curing and ensures uniform transmission of cardiac vibrations.

PDMS can be cured either at room temperature or by heating. Room temperature vulcanization (RTV) requires approximately 24 hours for complete curing. In contrast, thermal curing can significantly accelerate the process, with temperatures ranging from 60 °C to 100 °C and curing times between 15 minutes and 1 hour, depending on the material's thickness and ambient conditions.

Subsequently, the FBG sensing unit was arranged as shown in **Figure 40**. As illustrated, the CYTOP fiber FBG was initially placed at the center of the mold, while the SMF-28 silica fiber was arranged in a bent configuration. Three FBGs were inscribed along the SMF-28 fiber, sequentially positioned at three designated measurement points within the mold, with a spacing of 1 cm between each FBG. Among them, the FBG located at the center (designed Bragg wavelength: 1550 nm) was placed parallel to the CYTOP FBG for comparative analysis.

This layout was designed to identify the optimal sensing position for cardiac signal acquisition by simultaneously recording the waveform responses of the three FBGs on the SMF-28 fiber, based on Bragg wavelength shifts induced by strain. By comparing the response intensities at the three positions, the location with the strongest signal was selected as the primary sensing point. The sensor was then repositioned accordingly, relocating the CYTOP FBG to this optimal point, where it served as the main sensing element for subsequent signal acquisition.

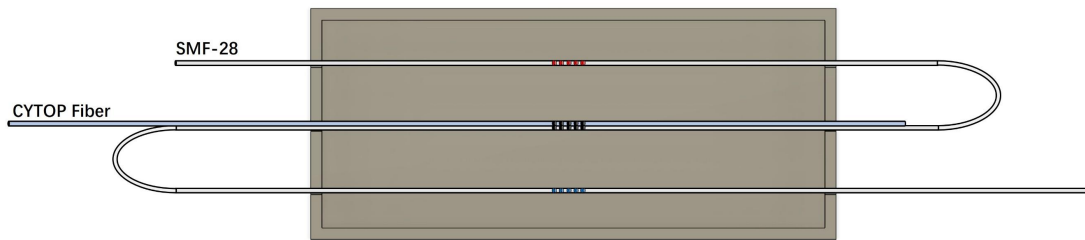


**Figure 40:** Layout of the FBGs Sensing Unit

Finally, the PDMS mixture was poured into the 3D-printed mold to complete the encapsulation. The packaging process is illustrated in **Figure 41**.

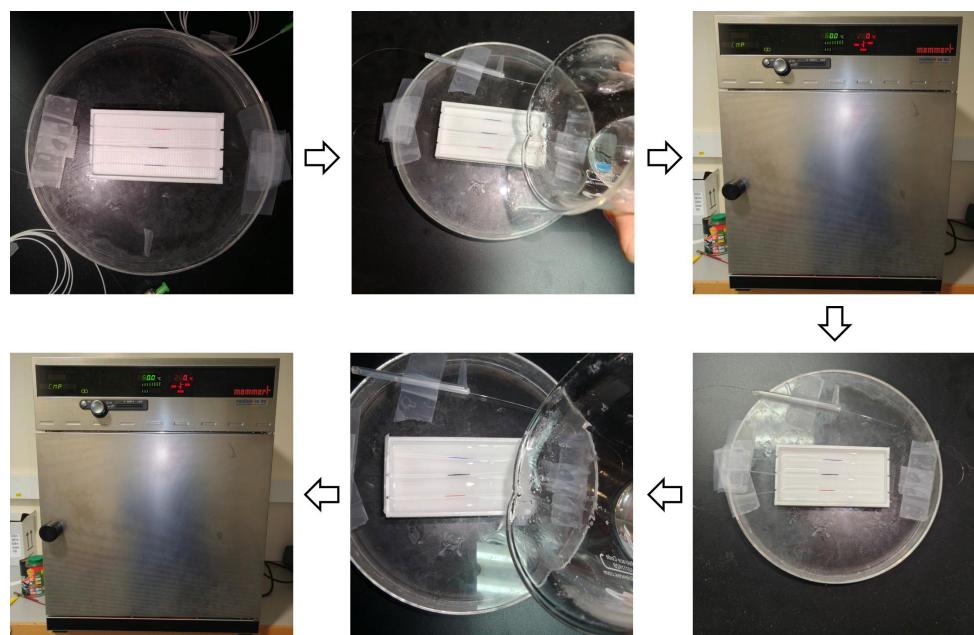


**Figure 41:** Encapsulation Process of the FBG Sensor

After arranging the optical fiber along the designated path, both ends of the fiber were secured with tape to ensure that the FBGs remained taut throughout the encapsulation process. This design not only enhances the sensor's strain sensitivity along the longitudinal direction, but also effectively prevents variations in initial strain caused by fiber displacement or inconsistent fixation, which could otherwise compromise the response consistency among the FBGs and degrade overall sensing performance.

Subsequently, the pre-treated PDMS material was slowly poured into the mold to fill its lower half, allowing the FBG array to float above the PDMS surface. This ensured that all FBGs remained in the same horizontal plane. To eliminate air bubbles and ensure uniformity within the material, the mold surface was gently tapped during pouring.

The mold was then placed in a 60 °C oven and heated for 30 minutes to cure the lower PDMS layer. After cooling, the mold was removed, the upper half was filled with additional PDMS, and the heating procedure was repeated until the entire structure was fully cured. This two-step casting process ensures that the region around the FBG remains close to the surface, resulting in a thinner PDMS layer above the sensor, which facilitates more efficient strain transmission.

After curing, use a knife to gently cut along the edges of the PDMS, and then extract the fully encapsulated sensing unit. As shown in **Figure 42**, the final sensor surface exhibits visible stripes caused by the layered texture of the 3D-printed mold. However, the top sensing surface—designed to be in direct contact with the skin—is smooth and free of bubbles or surface irregularities, indicating that the encapsulation process did not introduce any structural defects. This ensures reliable skin contact and effective transmission of cardiac vibration signals.

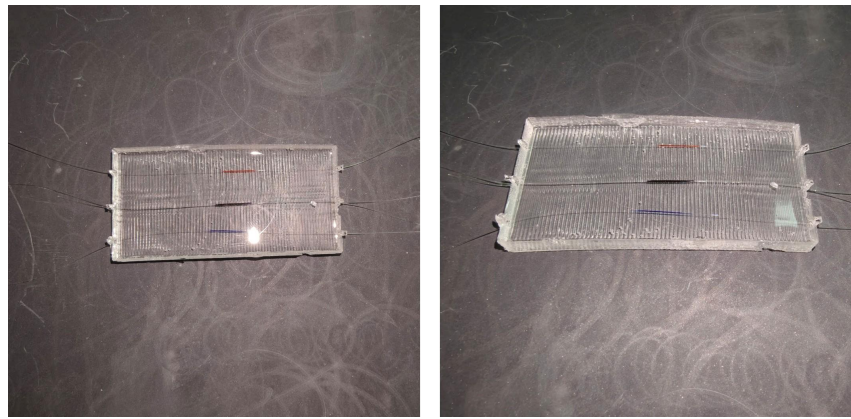


**Figure 42:** Optical Fiber FBG-Based Cardiac Sensor

Through the aforementioned method, the sensor was functionally optimized in two key aspects during the packaging process. First, the high-precision capability of 3D printing allows the encapsulation structure to be customized for specific application scenarios, which improves the sensor's adaptability to the measurement environment. Second, the polymer material PDMS offers excellent flexibility, enabling low-loss and low-latency transmission of cardiac vibrations while protecting the sensor. This ensures long-term stability in signal acquisition. Its outstanding biocompatibility also allows the sensor to be safely attached to human skin.

Compared with traditional packaging methods, this approach—combining 3D printing with polymer materials—provides greater design flexibility and supports rapid iteration for packaging structure optimization. The use of polymer materials further enhances the sensor's sensitivity and durability, making it suitable for signal detection under various environmental conditions.

## 5 Results and Discussion

### 5.1 Experimental setup

#### 5.1.1 Overview of system architecture design

To evaluate the sensor's performance in practical applications , We designed a complete FBG spectral demodulation and dynamic response testing system , The setup is shown in **Figure 43**. It includes a broadband light source, a fiber optic isolator, a  $1\times 2$  fiber coupler, a fiber circulator, an encapsulated sensing unit, an FBG demodulator, and a computer for data collection and analysis.

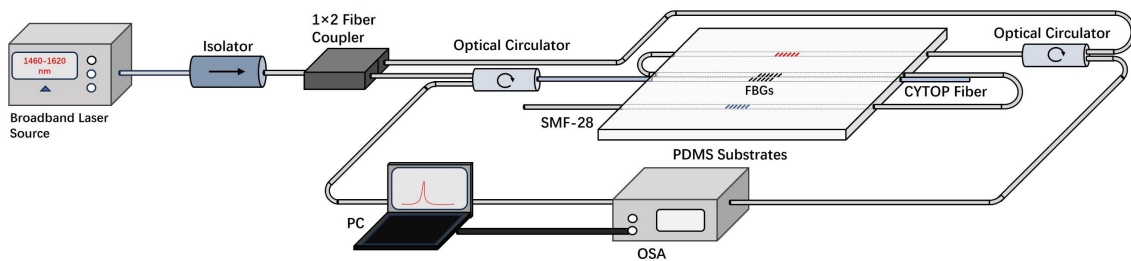


**Figure 43:** Designed Structure of the FBG Sensing and Demodulation System

In the designed system, the light source is a broadband source with a central wavelength range of 1460–1620 nm. It provides a stable, high-intensity, and continuous spectrum for signal input. A fiber optic isolator is placed after the source to prevent reflected light from returning to the laser, ensuring stable and safe operation. It also helps reduce system noise.

The optical signal then enters a  $1\times 2$  fiber coupler, which splits the beam into two paths: one for the CYTOP FBG and one for the SMF-28 FBG. This allows parallel excitation and signal detection through both sensing channels. Each reflected signal is directed by a fiber circulator into the spectrometer for wavelength analysis.

### 5.1.2 Integrated FBG Demodulation System

However, in the actual implementation of this system, an integrated solution was adopted using a modular light source (DL-BP1-1501A SLED). This module combines a broadband source, fiber isolator, and circulator within a compact unit. It supports multi-channel output and greatly simplifies connections between optical components compared to traditional systems. This integration improves system stability and enhances optical power management efficiency.

The reflected signals were received by a high-resolution spectrometer (SM125, Micron Optics). This demodulator has a wavelength resolution of 1 pm and uses a peak-tracking algorithm to monitor the Bragg wavelength in real time. With a sampling interval of 1 ms (1000 Hz), it effectively captures small high-frequency wavelength shifts in dynamic signals such as heartbeats and respiration. Thus, it meets the requirements for high temporal and spatial resolution in this experiment.

All optical paths are connected using FC/APC fiber jumpers. This helps reduce insertion loss and improves overall optical stability and demodulation accuracy. The simplified integrated sensing system is shown in **Figure 44**.

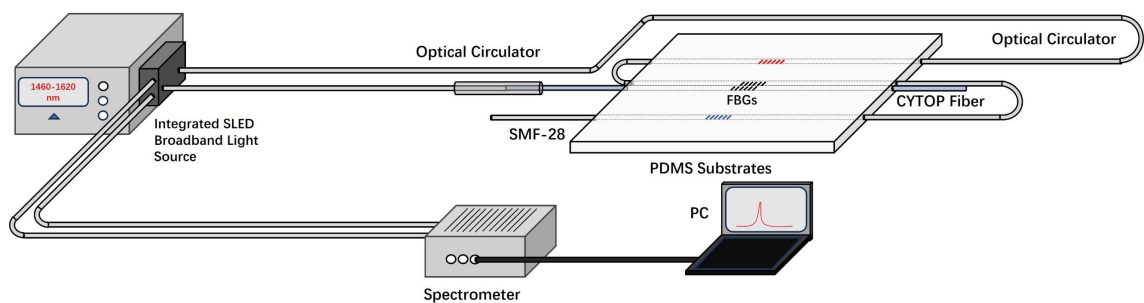


**Figure 44:** Simplified Structure of the Integrated Demodulation System

After the system was assembled, both the CYTOP FBG and the SMF-28 FBG were connected to the demodulation unit for simultaneous spectral detection. As shown in

**Figure 45**, the Bragg reflection peak of the CYTOP FBG (red curve) and that of the SMF-28 FBG (black curve) appear in two separate wavelength channels. The spacing between them is sufficient, and both peaks remain stable and clearly distinguishable.

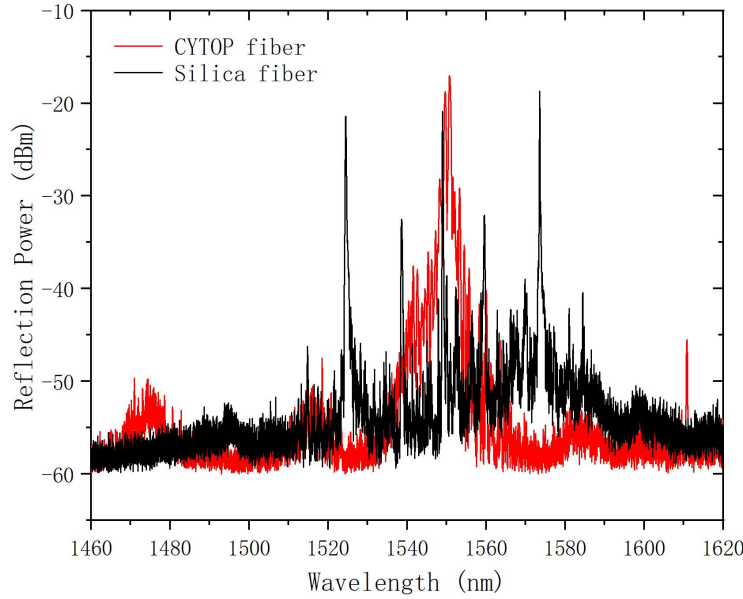


**Figure 45:** Reflection Spectra of Dual-Channel FBGs

The demodulator independently tracks the Bragg wavelength shifts in real time using peak tracking. The two reflection channels do not interfere with each other, which ensures accurate signal acquisition and channel separation. This setup lays a solid foundation for synchronized monitoring and sensitivity comparison in later experiments.

### 5.1.3 Vibration Platform and Excitation System

To simulate the dynamic response characteristics of the FBG sensors at different frequencies, a function generator and an electric vibration platform were introduced into the experimental setup. They formed a vibration excitation module with adjustable frequency and good repeatability. As shown in **Figure 46**, the FBG sensor was fixed onto the top surface of the vibration platform using adhesive tape. The function generator and vibration platform were connected via a standard interface, forming a complete dynamic testing unit.

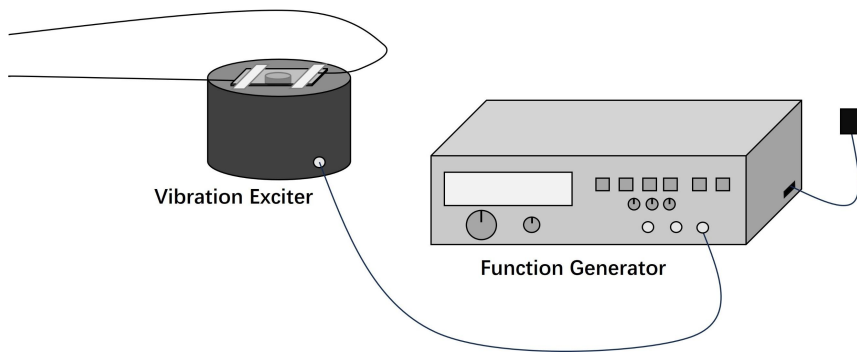


**Figure 46:** Structure of the Excitation System and Vibration Platform

In this experiment, we used a **GW Insteek GFG-8020H** function generator. This generator provides an output frequency ranging from 0.1 Hz to 2 MHz and supports multiple waveform signals, including sine wave, square wave, and triangle wave. The sine wave was mainly used to simulate continuous physiological processes such as respiration and heartbeat, while the square and triangle waves were chosen to test the sensor's dynamic response to abrupt loading or linear displacement changes.

For mechanical excitation, we used a B&K Type 4809 electric vibration platform. This platform supports a frequency response from DC to 10 kHz, thus covering most frequency components involved in human cardiac and respiratory signals.

The frequency and voltage output range of the entire excitation system covered the following three typical frequency bands related to cardiac signals:

- Low-frequency band (0.1–0.9 Hz, high amplitude): Represents respiratory rhythms and slow cardiac activities in resting conditions, corresponding to low-frequency displacement signals caused by periodic expansion and contraction of the chest.
- Mid-frequency band (1–10 Hz, moderate amplitude): Covers typical heartbeat frequencies and includes major mechanical features in SCG signals, such as overall cardiac movements during ventricular systole and diastole.
- High-frequency band (10–100 Hz, micro vibrations): Represents rapid and localized cardiac vibrations, including high-frequency transient events like aortic

valve opening (AO peak), often used to analyze detailed mechanical changes in heart conditions.

Combined with the FBG demodulation system, our experimental setup allowed continuous frequency scanning and specific-frequency excitation. This enabled real-time observation of reflected wavelength responses and facilitated the analysis of sensor sensitivity and bandwidth characteristics across different frequencies.

## **5.2 Preliminary experiments: Influence of structural parameters on FBG sensitivity**

Before conducting cardiac signal measurements on the human body, we performed two basic experiments. These preliminary tests were designed to evaluate how key structural parameters influence the sensitivity and stability of the FBG response. The experiments focused on the following two aspects:

### **Influence of pre-strain loading on FBG sensitivity:**

We investigated the wavelength responses of FBGs to external periodic vibrations under different initial stretching conditions.

### **Effect of packaging on sensing performance:**

We compared the responses when the top and bottom surfaces of the packaged FBG faced the vibration platform. This allowed further analysis of how differences in PDMS packaging thickness affect strain transmission.

These preliminary experiments provided essential structural guidance for the subsequent formal measurements. They also allowed us to verify the performance differences between CYTOP and SMF-28 FBGs under identical packaging conditions, laying a solid foundation for future comparative tests.

### **5.2.1 Influence of pre-strain on FBG sensitivity**

The response of FBG sensors closely depends on the pre-strain applied during installation. Proper pre-strain can enhance strain transfer efficiency, increasing sensor sensitivity and signal stability. This section evaluates the responses of CYTOP and SMF-28 FBG under different pre-strain conditions to determine the optimal setting.

- **Experimental design**

We used bare CYTOP and SMF-28 fibers attached to a vibration platform. As shown in **Figure 47**, the fibers were secured using tape. Low pre-strain was achieved with a single tape layer, while high pre-strain used two layers to induce distinct stretching conditions.

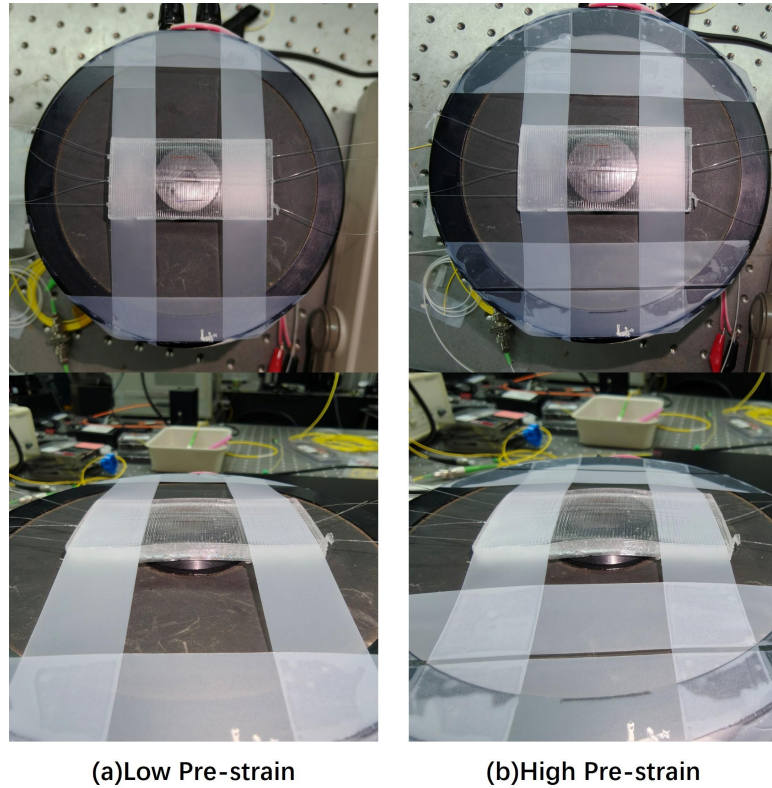


**Figure 47:** Fiber attachment methods with different pre-strain levels

The initial reflection spectra were recorded using the spectrometer (**Figure 48**). Fig. 48(a) shows the reference spectrum. In low pre-strain conditions (Fig. 48(b)), the CYTOP FBG peak shifted from 1550.78 nm to 1551.01 nm, and SMF-28 shifted from 1549.01 nm to 1549.82 nm. In high pre-strain conditions (Fig. 48(c)), the CYTOP peak shifted to 1554.50 nm, and SMF-28 shifted to 1550.07 nm. These shifts confirmed successful pre-strain application.

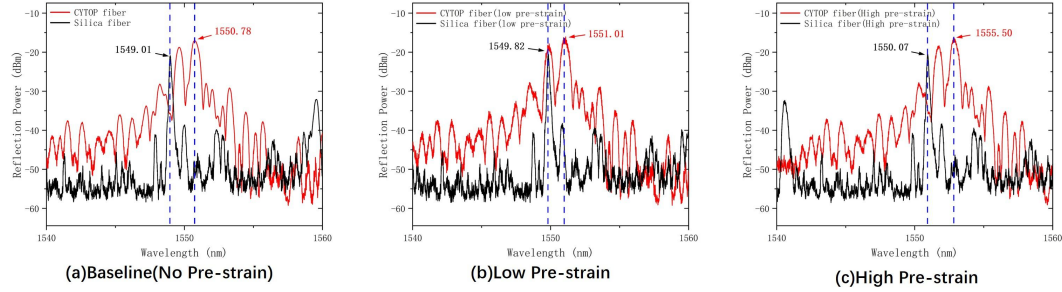


**Figure 48:** Initial reflection spectra under varying pre-strain conditions

To verify fiber attachment stability, we recorded baseline spectra for 5 seconds without excitation (**Figure 49**). Both low and high pre-strain conditions showed stable wavelength baselines without noticeable drift, indicating secure attachment.

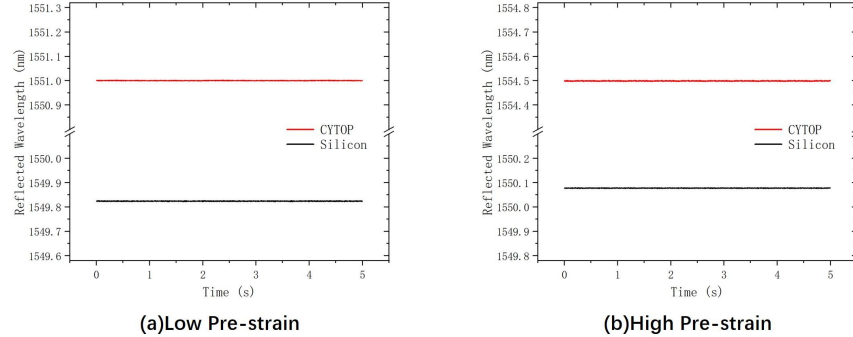


**Figure 49:** Baseline stability test under no excitation

### ● Dynamic response tests

With stable fiber attachment, the platform was driven by 1 Hz, 15 V sine and square wave signals, and wavelength responses were measured.

Under sine excitation (**Figure 50**), CYTOP response improved from 0.18 nm (low) to 0.36 nm (high pre-strain), nearly doubling. SMF-28 response increased from 0.04 nm to 0.16 nm, tripling.

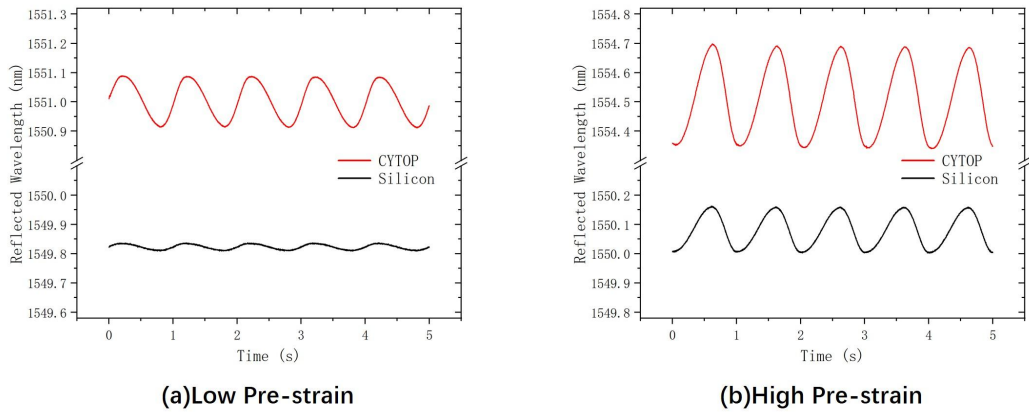


**Figure 50:** FBG wavelength responses to 1 Hz sine-wave excitation

Under square excitation (**Figure 51**), CYTOP response increased from 0.19 nm to 0.37 nm, while SMF-28 increased from 0.04 nm to 0.16 nm.

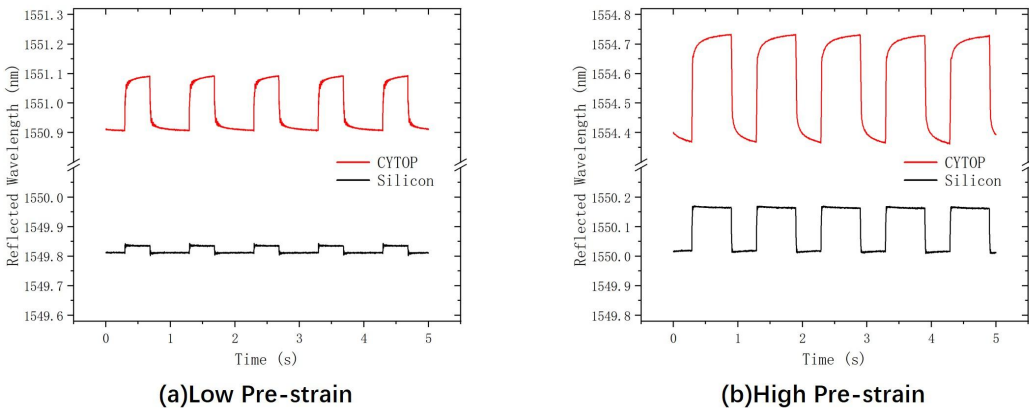


**Figure 51:** FBG wavelength responses to 1 Hz square-wave excitation

The square-wave tests showed CYTOP had slower recovery with noticeable trailing edges, while SMF-28 showed sharper and quicker responses. This difference arises mainly from the mechanical properties: the flexibility and viscoelasticity of CYTOP lead to slower strain recovery, whereas silica fiber responds more rapidly.

### ● Results and conclusions

Under the same pre-strain, CYTOP had significantly higher static strain sensitivity than SMF-28. However, CYTOP showed limited dynamic response improvement, while

SMF-28 showed more noticeable enhancement. This is likely due to uneven stress distribution and rapid strain release within the CYTOP material.

Nevertheless, CYTOP still had higher overall dynamic sensitivity. Considering both sensitivity and stability, all subsequent experiments adopted double-layer tape for pre-strain and applied moderate PDMS stretching as the standard installation method. This ensured high sensitivity and stability for subsequent testing and human experiments.

### **5.2.2 Effect of packaging on sensing performance**

In the two-step casting process described earlier, the fiber was successfully embedded at different depths within the PDMS package. Since the PDMS thickness affects strain transfer efficiency, further evaluation of its influence on sensor sensitivity was necessary.

To investigate this, we designed a comparative experiment. Under consistent pre-strain conditions, sensors were tested in two orientations:

**Normal Placement:** thin PDMS layer facing downward, FBG closer to the vibration platform.

**Reversed Placement:** thick PDMS layer facing downward, FBG farther from the platform.

By comparing the wavelength responses under identical excitations, we analyzed how PDMS thickness influenced strain transfer efficiency.

- **Experimental design**

As shown in **Figure 52**, sensors in Normal and Reversed Placements were fixed to the vibration platform using double-layer tape. This setup prevented movement during excitation and ensured consistent pre-strain by adjusting tape positioning.

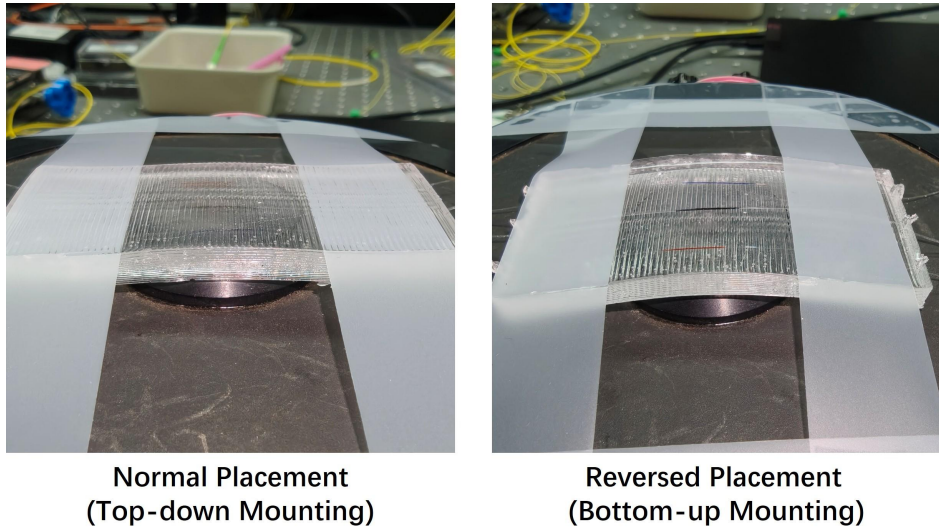


**Figure 52:** Sensor installation in Normal and Reversed Placements

**Figure 53** presents reflection spectra of CYTOP and SMF-28 FBG in both placements. Initial wavelength shifts were nearly identical in both orientations (CYTOP: 1548.744 nm and 1548.743 nm; SMF-28: 1548.512 nm and 1548.514 nm). Slight anomalies in wavelength shift direction were possibly due to uneven packaging stress or micro-bending during tape fixation. However, these minor deviations did not significantly impact overall experimental conclusions. The consistent geometric placement provided structural comparability for subsequent sensitivity testing.

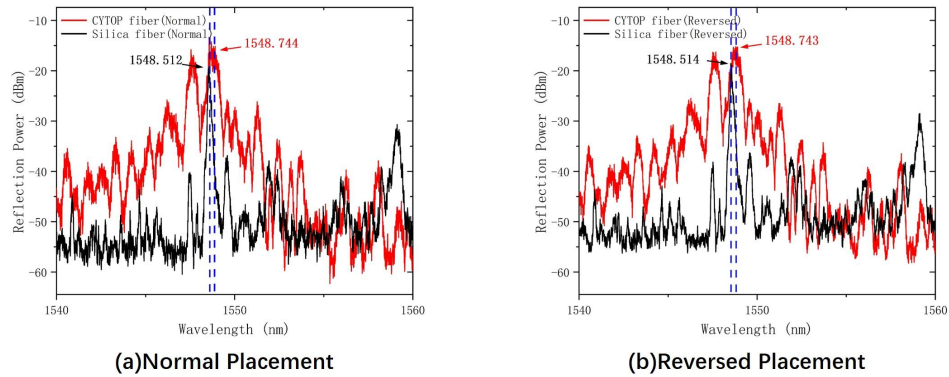


**Figure 53:** Reflection spectra of FBGs under different placements

- **Dynamic response testing**

After stable fixation, the platform was driven by 1 Hz, 15 V sine wave and square wave signals. Dynamic wavelength responses were measured (**Figure 54**):

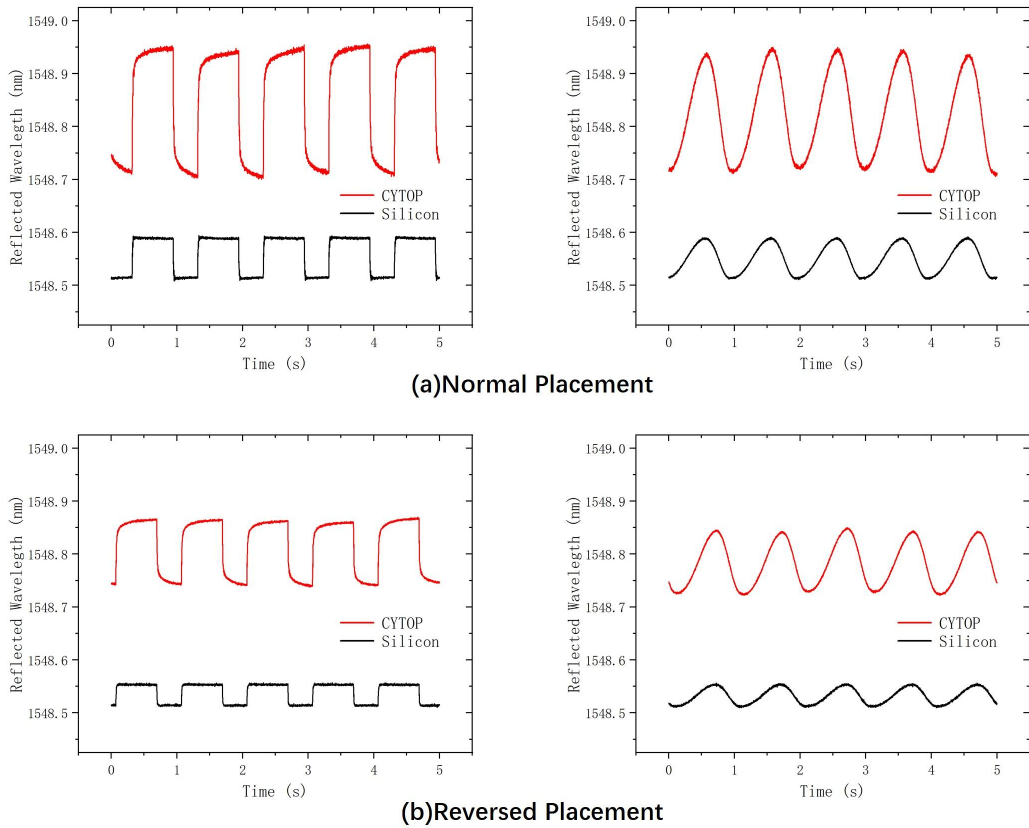


**Figure 54:** Dynamic responses of FBG in different placements: (a) Normal Placement; (b) Reversed Placement

### Normal Placement:

CYTOP response ~0.25 nm (square wave), ~0.23 nm (sine wave);

SMF-28 response ~0.09 nm (square wave), ~0.08 nm (sine wave).

### Reversed Placement:

CYTOP response reduced to ~0.14 nm (square wave), ~0.13 nm (sine wave);

SMF-28 response reduced to ~0.05 nm (both waves).

## ● Results and conclusions

The results clearly show that PDMS thickness significantly affects strain transfer efficiency. Placing the thin PDMS layer near the excitation source (Normal Placement) led to better strain transfer and larger wavelength responses. Conversely, thicker PDMS layers reduced strain transfer efficiency and lowered response amplitudes.

This observation aligns with the rationale of our two-step casting process, placing fibers near the side to shorten the strain transmission path and enhance sensitivity with enough PDMS package thickness for protection. Thus, Normal Placement was adopted as the standard orientation for all subsequent experiments, ensuring high sensitivity and stability.

### 5.3 Vibration frequency response testing

After evaluating the effects of pre-strain and packaging on FBG sensitivity and stability, we further conducted dynamic excitation experiments under different frequency and amplitude conditions. These tests aimed to verify the sensor's dynamic response capability and signal detection stability in physiological monitoring scenarios.

The frequency ranges of typical cardiorespiratory signals are as follows: respiratory signals generally fall between 0.1–0.5 Hz; heartbeats are typically in the range of 0.7–3 Hz [79]; and seismocardiogram (SCG) signals mainly occupy the 5–30 Hz range, with some high-frequency components extending up to 100 Hz [80]. These ranges formed the basis for the dynamic excitation design in this section.

To cover the full spectrum of physiological signal features, we applied three representative excitation conditions that correspond to respiration, heartbeat, and SCG frequency bands. The excitation voltage decreased with increasing frequency to reflect the natural relationship between physiological frequency and mechanical amplitude:

- Low-frequency range (0.1–0.9 Hz): 10 V excitation to simulate respiratory rhythms and slow cardiac motion with large displacements.
- Mid-frequency range (1–10 Hz): 5 V excitation to represent typical heart rates and SCG components related to ventricular motion.
- High-frequency range (10–100 Hz): 2 V excitation to simulate rapid, localized myocardial vibrations such as aortic valve opening (AO peak).

This strategy of reducing excitation amplitude at higher frequencies was based on two main considerations:

**Physiological relevance:** Respiratory movements cause the largest chest displacement, while SCG signals are much smaller—often just a few microns. Lower excitation at

high frequencies better reflects real physiological conditions and tests the sensor's limit in detecting micro-movements.

**Experimental stability:** Applying large amplitudes at high frequencies can cause unwanted disturbances such as tape loosening, PDMS resonance, and structural artifacts from platform inertia. These effects introduce noise, spectral artifacts, or peak tracking errors that obscure true wavelength shifts and interfere with accurate analysis of FBG responses.

### 5.3.1 Low-frequency range (0.1–0.9 Hz): Response under large-amplitude excitation

- **Experimental design**

Respiration and resting heartbeats often produce slow, high-amplitude periodic chest wall motion, typically below 1 Hz. These signals have clear periodicity and recognizable waveform patterns. To evaluate sensor performance under such conditions, we conducted low-frequency excitation tests using relatively large amplitudes.

Setting up the function generator output 10 V sine and square waves within 0.1–0.9 Hz. These signals drove the vibration platform to produce periodic displacement. The Bragg wavelength responses of CYTOP and SMF-28 FBGs were recorded over a 25-second period and analyzed to assess their sensitivity to low-frequency signals.

- **Wavelength response and sensitivity**

The Bragg wavelength responses under sine wave excitation are shown in **Figure 55**.

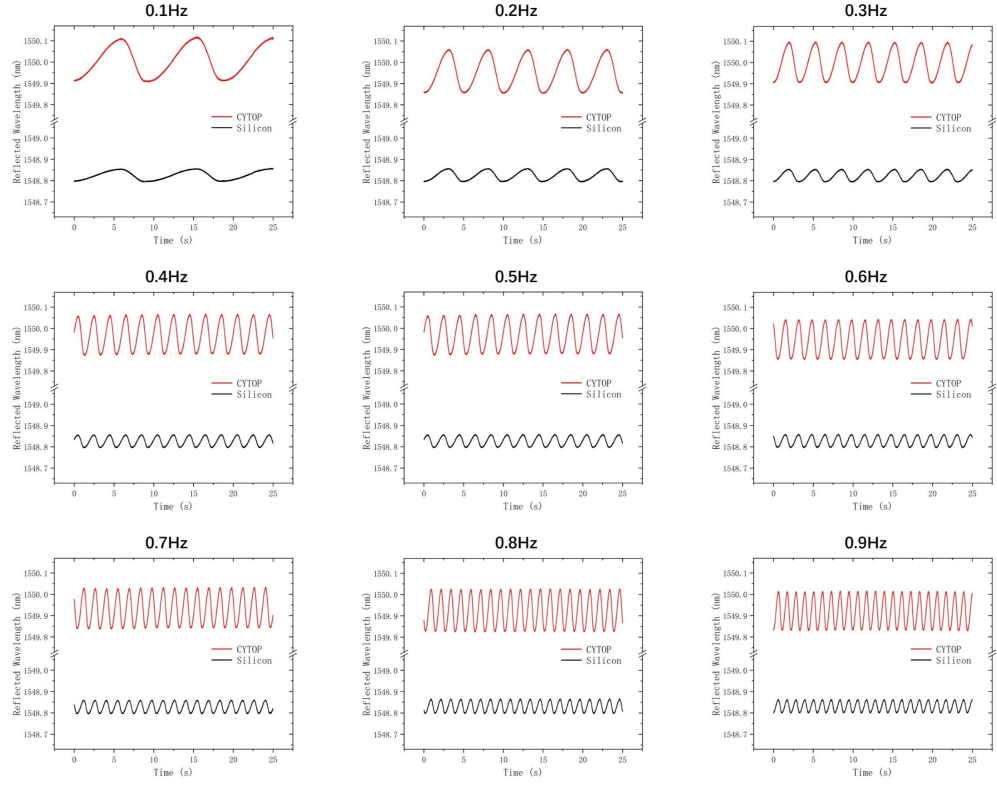


**Figure 55:** Wavelength responses under 0.1–0.9 Hz sine wave excitation

The peak and trough of each cycle were extracted to calculate the average wavelength shift ( $\Delta\lambda$ ), as summarized in **Figure 56**.

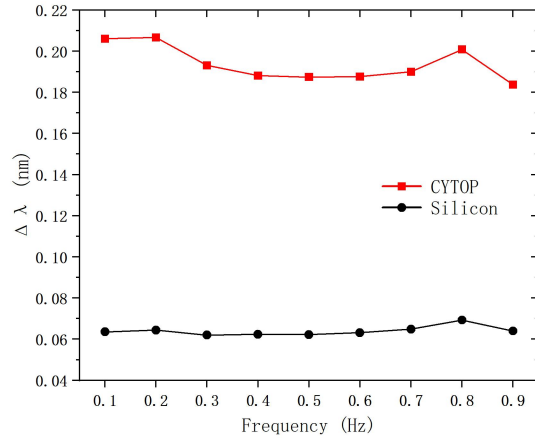


**Figure 56:** Average wavelength shift ( $\Delta\lambda$ ) under 0.1-0.9Hz sine wave excitation

To directly compare sensor sensitivity, the ratio of  $\Delta\lambda_{CYTOP}$  to  $\Delta\lambda_{SMF-28}$  was calculated (**Figure 57**). Across all frequencies, the ratio remained between 2.8 and 3.3, indicating significantly higher sensitivity of CYTOP to low-frequency sine wave signals.

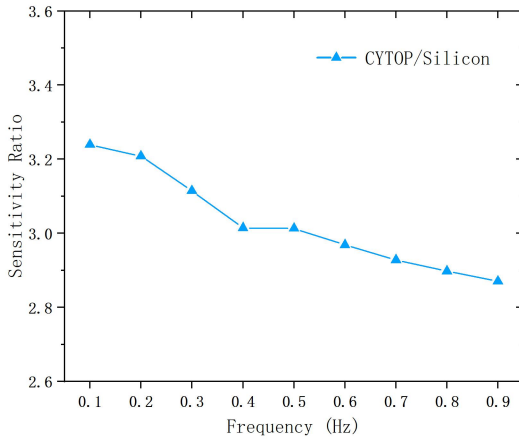


**Figure 57:** Sensitivity ratio ( $\Delta\lambda_{CYTOP} / \Delta\lambda_{SMF-28}$ ) under 0.1–0.9Hz sine wave excitation

When the excitation was switched to square waves, the responses of both sensors are shown in **Figure 58**;

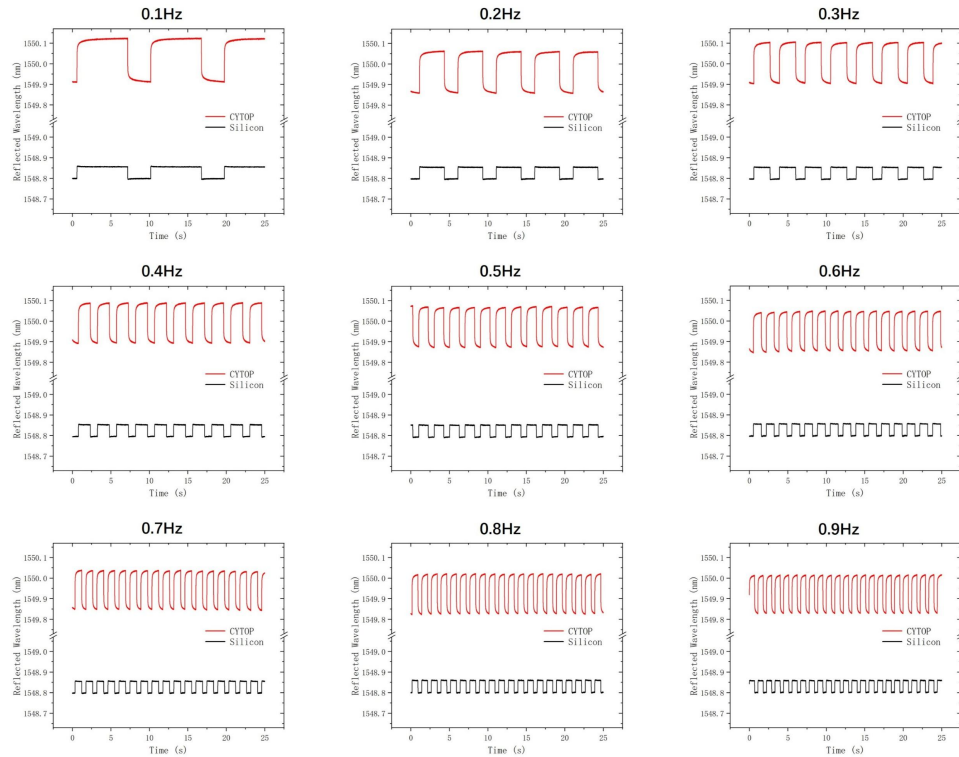


**Figure 58:** Wavelength responses under 0.1–0.9 Hz square wave excitation

And the average wavelength shifts are summarized in **Figure 59**. Compared to the sine wave results (Fig. 55), both fibers showed larger wavelength shifts under square wave excitation.

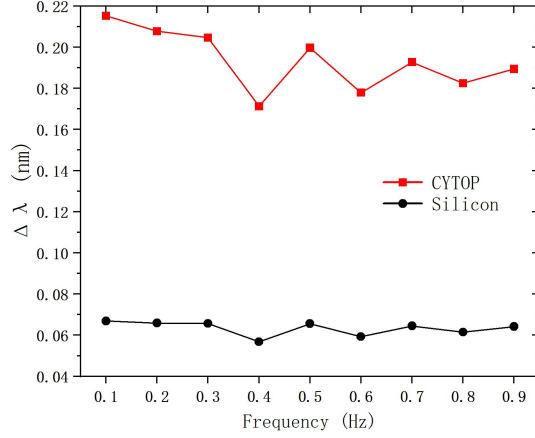


**Figure 59:** Average wavelength shift ( $\Delta\lambda$ ) under 0.1-0.9Hz square wave excitation

The sensitivity ratio under square wave input is shown in **Figure 60**. The results confirm the superior low-frequency response of the CYTOP FBG.

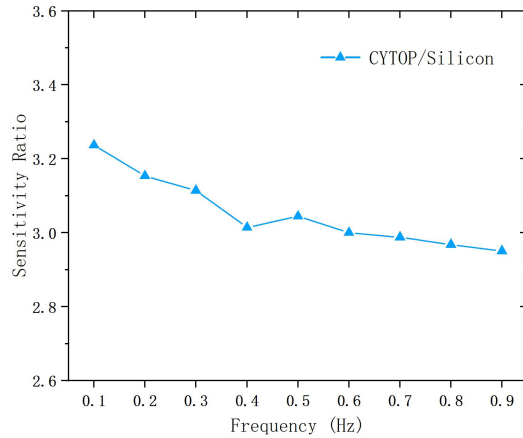


**Figure 60:** Sensitivity ratio ( $\Delta\lambda_{\text{CYTOP}} / \Delta\lambda_{\text{SMF-28}}$ ) under 0.1-0.9Hz square wave excitation

## ● Results and conclusion

In the 0.1–0.9 Hz range, the CYTOP FBG consistently exhibited larger wavelength shifts than SMF-28. The sensitivity ratio remained stable between 2.8 and 3.3. The ratio

slightly decreased with increasing frequency, but no reversal or crossover occurred. This confirms that CYTOP maintains a clear sensitivity advantage, making it better suited for detecting low-frequency physiological signals such as respiration and resting heartbeat.

### **5.3.2 Mid-frequency range (1–10 Hz): Response under moderate-amplitude excitation**

- Experimental design**

During the cardiac cycle, ventricular contraction and relaxation generate rhythmic chest wall vibrations typically within the 1–10 Hz range. This band includes not only the dominant heartbeat frequencies (1–3 Hz) but also key SCG components such as rapid filling and isovolumetric contraction. Compared to low-frequency signals, mid-frequency vibrations have shorter cycles and moderate amplitudes, posing higher demands on sensor responsiveness and spectral resolution.

To simulate such signals, we used sine and square wave excitations ranging from 1 to 10 Hz, driven at 5 V. Additionally, we included a 1 Hz excitation at 10 V as a reference. All tests were performed under consistent pre-strain and mounting conditions. Recording The Bragg wavelength shift ( $\Delta\lambda$ ) over each 10-second period.

- Wavelength response and sensitivity**

The responses under sine wave excitation are shown in **Figure 61**. The 10 V excitation at 1 Hz is included in Fig. 60 as a reference for comparison.

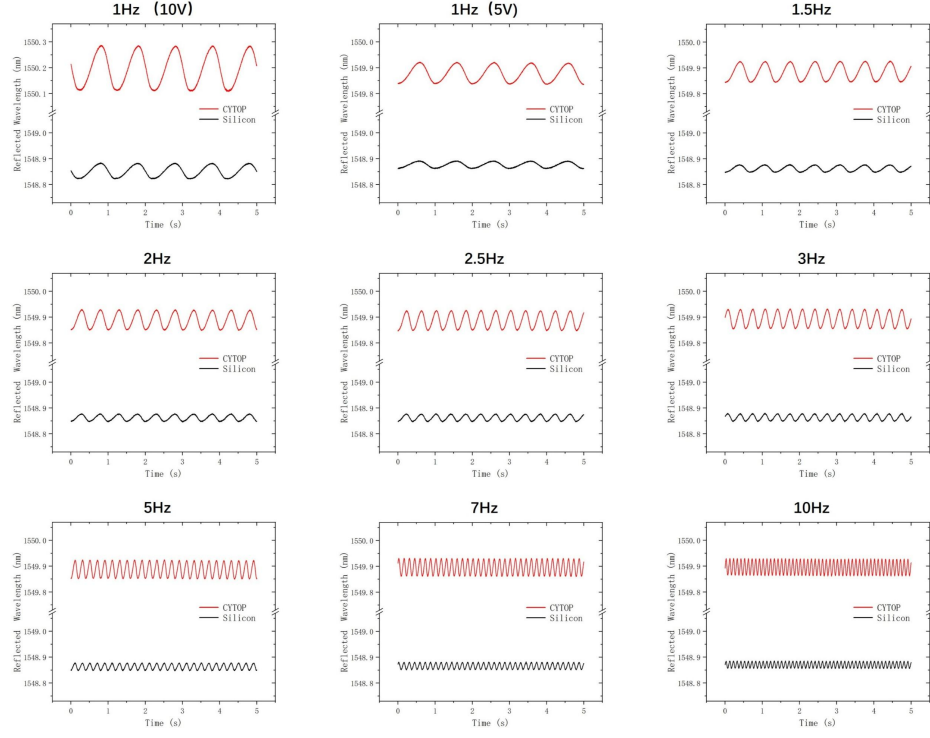


**Figure 61:** Wavelength responses under 1–10 Hz sine wave excitation

And **Figure 62** shows the average wavelength shifts of CYTOP and SMF-28 FBGs across the 1–10 Hz frequency range.

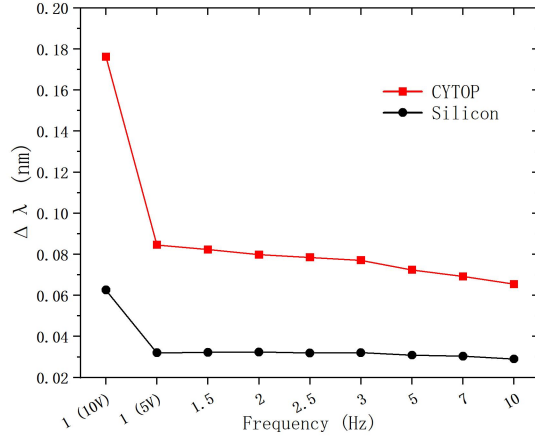


**Figure 62:** Average wavelength shift ( $\Delta\lambda$ ) under 1–10 Hz sine wave excitation

Comparing the 1 Hz responses under 5 V and 10 V, the wavelength shifts scale approximately linearly with excitation amplitude (1/2), confirming that both the

platform and the sensors maintain linear behavior. Under 5 V, both FBGs also showed stable responses across cycles. **Figure 63** presents the corresponding sensitivity ratio.

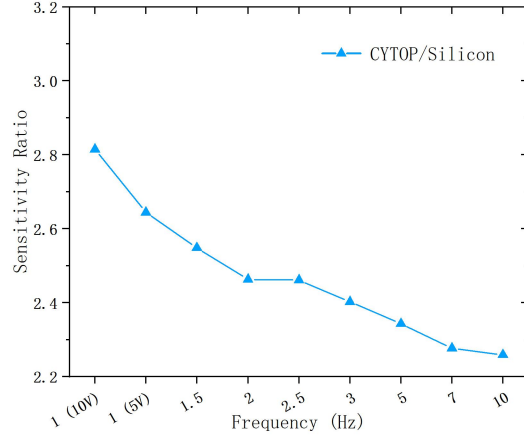


**Figure 63:** Sensitivity ratio ( $\Delta\lambda_{\text{CYTOP}} / \Delta\lambda_{\text{SMF-28}}$ ) under 1-10Hz sine wave excitation

When the excitation was changed to square waves, the response curves are shown in **Figure 64**.

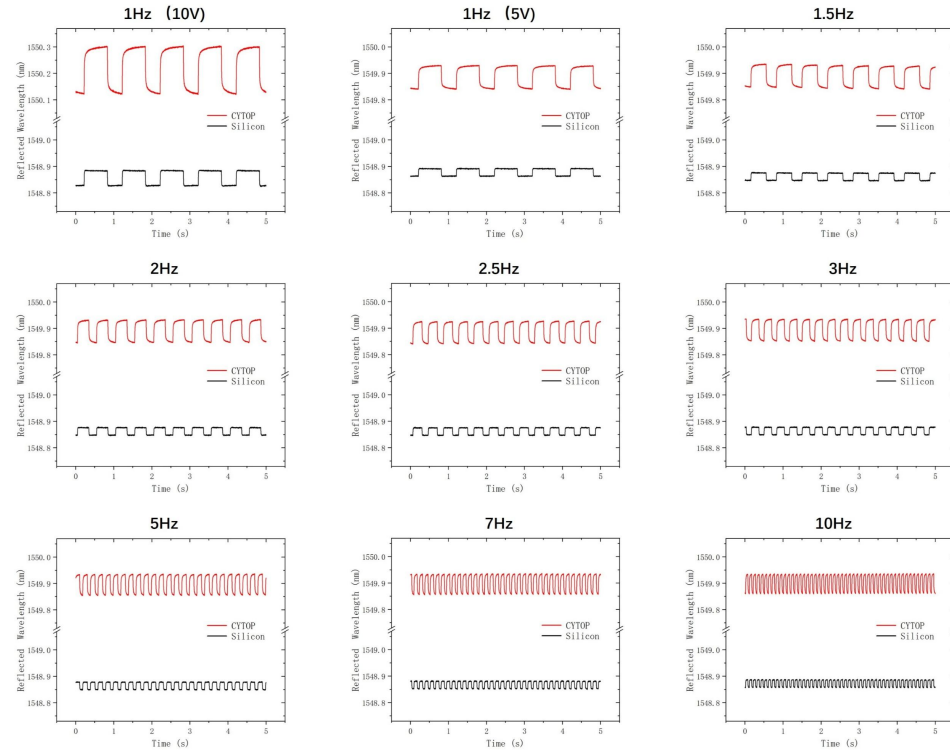


**Figure 64:** Wavelength responses under 1-10 Hz square wave excitation

And the average wavelength shifts in **Figure 65**. CYTOP FBG did not exhibit obvious trailing effects or delay under step excitation, suggesting that its viscoelastic recovery did not significantly limit performance in this frequency range.

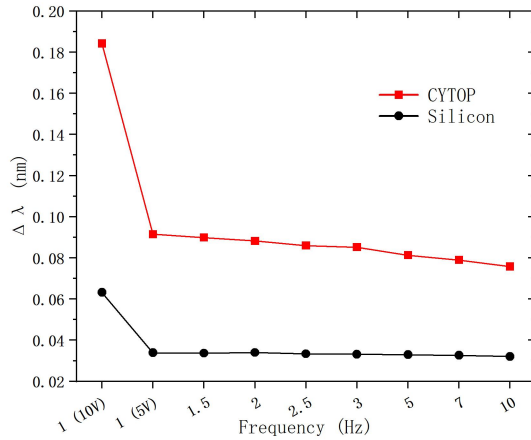


**Figure 65:** Average wavelength shift ( $\Delta\lambda$ ) under 1-10Hz square wave excitation

The corresponding sensitivity ratio is shown in **Figure 66**.

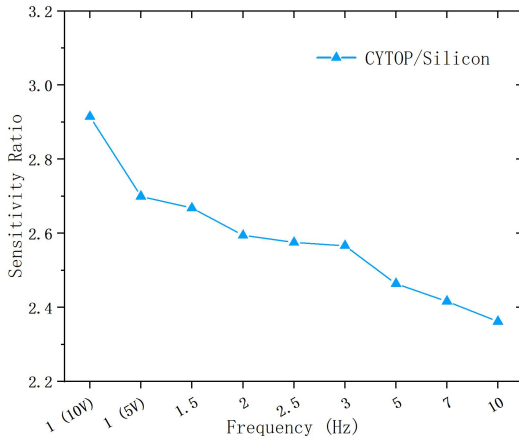


**Figure 66:** Sensitivity ratio ( $\Delta\lambda_{\text{CYTOP}} / \Delta\lambda_{\text{SMF-28}}$ ) under 1-10Hz square wave excitation

## ● Results and conclusion

CYTOP FBG consistently showed higher wavelength shifts than SMF-28 across the 1–10 Hz range. The average sensitivity ratio remained between 2.3 and 3.0. This

advantage was especially prominent in the 1–3 Hz band, which corresponds to typical heartbeat frequencies and related cardiac events.

The comparison between 10 V and 5 V excitation at 1 Hz also confirmed the linear relationship between excitation amplitude and FBG response, validating the sensor's suitability for physiological signal detection. Overall, CYTOP FBG demonstrated excellent dynamic tracking and spectral resolution in the mid-frequency range, making it suitable for detecting heartbeat and SCG features such as rapid filling and isovolumetric contraction.

### **5.3.3 High-frequency range (10–100 Hz): Response under micro-amplitude excitation**

- Experimental design**

Beyond respiratory and heartbeat signals, cardiac activity also includes higher-frequency, low-amplitude vibrations caused by brief mechanical events such as valve opening, blood ejection, and localized muscle movements. These signals typically fall within the 10–100 Hz range and represent the high-frequency components of SCG. A key feature is the AO (aortic valve opening) peak, which marks the onset of ventricular contraction.

High-frequency SCG signals have shorter cycles and smaller amplitudes, requiring higher sensor sensitivity, faster response, and better signal-to-noise ratio. To evaluate the performance of CYTOP FBG in detecting such signals, we conducted high-frequency excitation tests under the same pre-strain and setup. The excitation voltage was reduced to 2 V to avoid nonlinear responses of experimental system and better simulate the real amplitude of micro-vibrations. The Bragg wavelength responses were recorded over a 0.5-second period.

- Wavelength response and sensitivity**

**Figure 67** shows the Bragg wavelength responses of CYTOP and SMF-28 FBGs under high-frequency sine wave excitation.

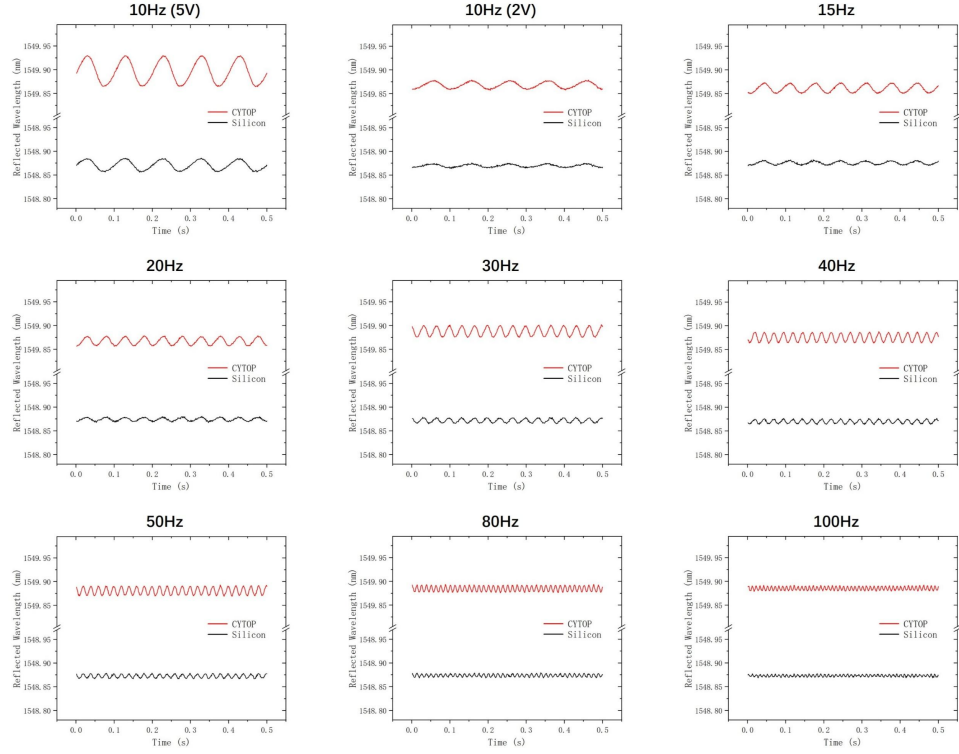


**Figure 67:** Wavelength responses under 10-100 Hz sine wave excitation

The average wavelength shifts across frequencies are summarized in **Figure 68**.

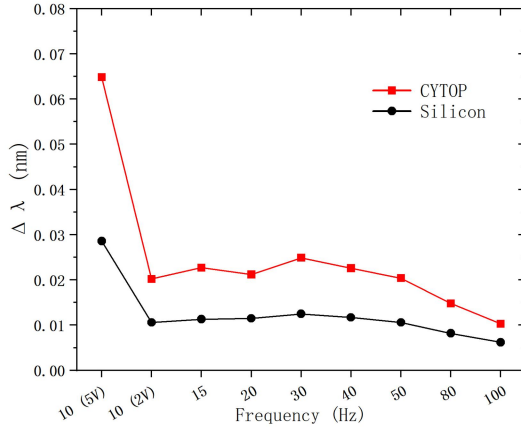


**Figure 68:** Average wavelength shift ( $\Delta\lambda$ ) under 10-100Hz sine wave excitation

At 10 Hz, the comparison test still confirmed a linear relationship between the excitation amplitude and the wavelength shift of the CYTOP FBG. When the vibration amplitude was reduced, the wavelength response also decreased proportionally to approximately 1/5 of the original value, indicating that the linear behavior remained consistent even

under high-frequency excitation. At 10-100 Hz, the CYTOP FBG response exhibited some fluctuations and was less stable compared to the SMF-28 FBG. However, it still showed higher sensitivity across all tested frequencies. The corresponding sensitivity ratio is shown in **Figure 69**.

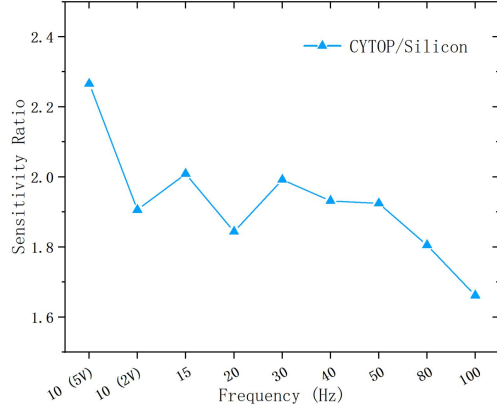


**Figure 69:** Sensitivity ratio ( $\Delta\lambda_{\text{CYTOP}} / \Delta\lambda_{\text{SMF-28}}$ ) under 10-100Hz sine wave excitation

Repeated the test with square wave input. The Bragg wavelength responses are presented in **Figure 70**.

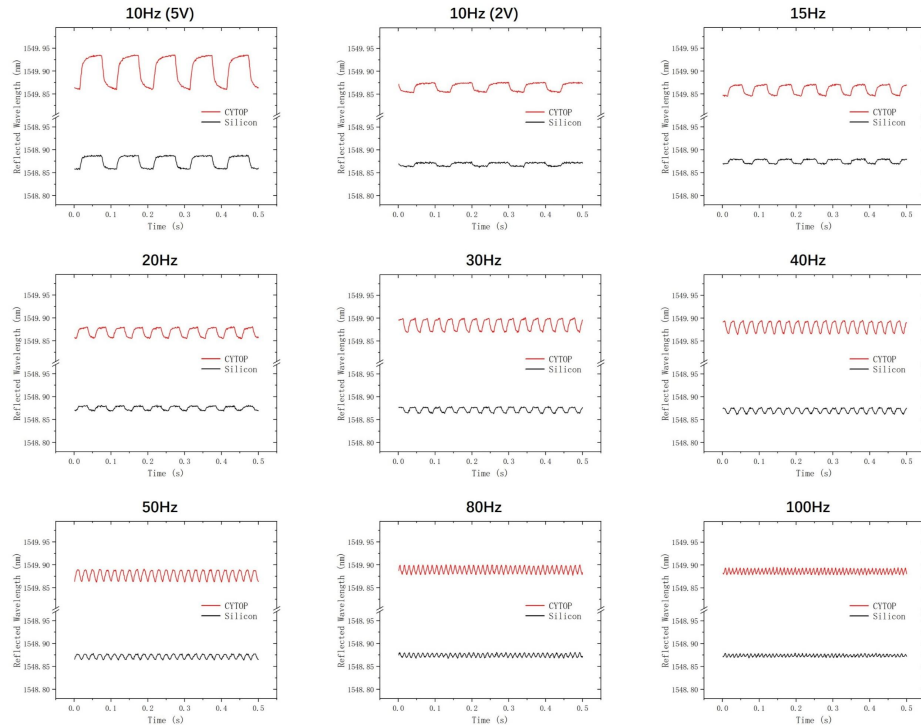


**Figure 70:** Average wavelength shift ( $\Delta\lambda$ ) under 10-100Hz square wave excitation

Although square waves became less distinct beyond 50 Hz due to platform limitations, periodic features were still observable. The average wavelength shifts are shown in **Figure 71**.

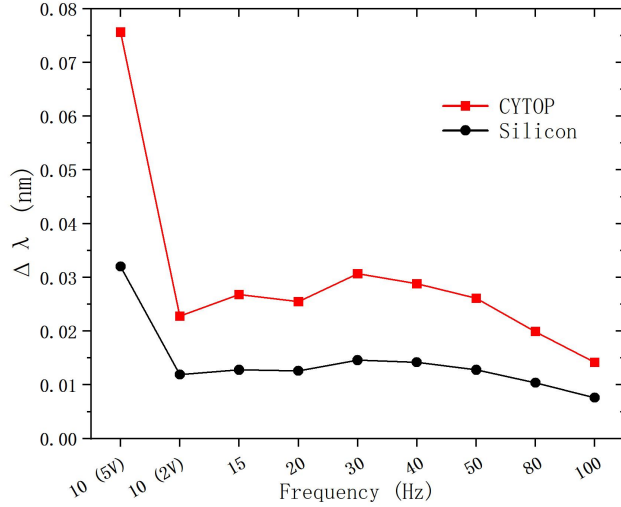


**Figure 71:** Average wavelength shift ( $\Delta\lambda$ ) under 10-100Hz square wave excitation

And the corresponding sensitivity ratio in **Figure 72**.

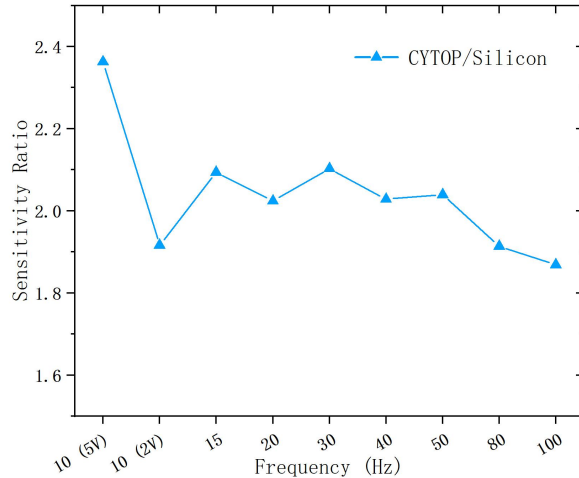


**Figure 72:** Sensitivity ratio ( $\Delta\lambda_{\text{CYTOP}} / \Delta\lambda_{\text{SMF-28}}$ ) under 10-100Hz square wave excitation

Overall, CYTOP demonstrated stronger responses to square wave excitation compared to sine wave, with small fluctuations but consistently higher sensitivity.

## ● Results and conclusion

Across the 10–100 Hz range, CYTOP FBG consistently outperformed SMF-28 in terms of wavelength shift. Even under reduced 2 V excitation, CYTOP maintained a 1.6–2.2× sensitivity advantage at most frequencies.

While the gap between CYTOP and SMF-28 narrowed with increasing frequency, CYTOP still showed clear and detectable responses at 80–100 Hz, where SMF-28 signals had mostly attenuated.

In particular, between 10–50 Hz, CYTOP delivered stable, periodic responses with clearly defined amplitude, confirming its potential for detecting high-frequency SCG components such as the AO peak.

### 5.3.4 Summary of vibration response across all frequencies

**Figure 73** summarizes the sensitivity ratio between CYTOP and SMF-28 FBGs across all tested frequencies. The results show that CYTOP exhibits the greatest advantage in the low-frequency range (0.1–0.9 Hz), a slightly reduced advantage in the mid-frequency range (1–10 Hz), and a further decrease in the high-frequency range (10–100 Hz). However, across all bands, its average wavelength shift remains more than 2x that of SMF-28.

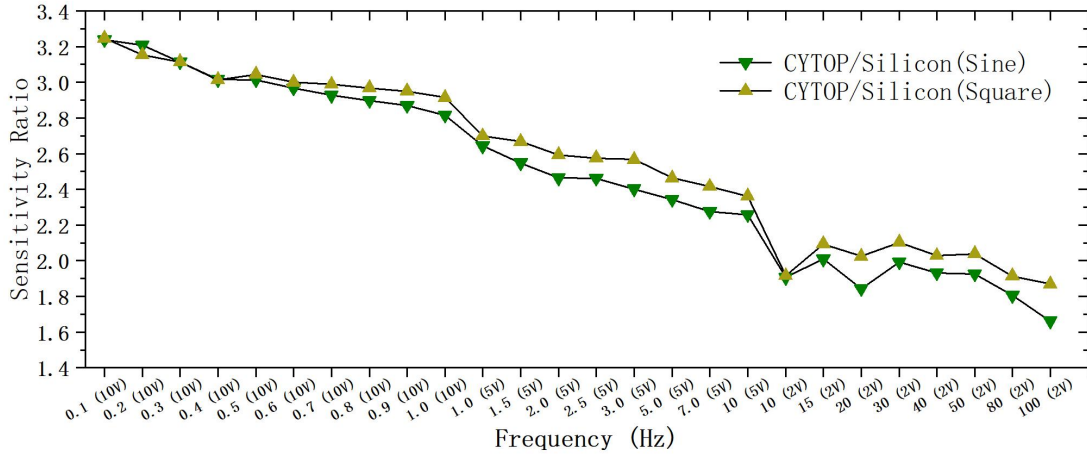


**Figure 73:** Sensitivity ratio (CYTOP vs. SMF-28) across all frequency bands

Apart from the decreasing excitation voltage used at higher frequencies, this downward trend in sensitivity ratio may be attributed to the viscoelastic properties of the CYTOP material and the damping effect of the PDMS packaging. These factors contribute to response delay and energy dissipation under high-frequency excitation, thus reducing the relative sensitivity advantage.

Nevertheless, within the key frequency range relevant to cardiac health monitoring (0.1–30 Hz), CYTOP FBGs continue to demonstrate a clear advantage. In particular, strong and stable performance is observed in the heartbeat-dominant range (0.7–3 Hz) and the SCG high-frequency band (5–30 Hz), where features such as the AO peak occur.

Based on the results across all test bands:

- Low-frequency tests verified the high sensitivity and low-noise performance of CYTOP FBG in detecting slow periodic signals such as respiration and resting heartbeats.
- Mid-frequency tests confirmed its ability to track ventricular contraction and relaxation dynamics, with a consistent linear response.
- High-frequency tests demonstrated its transient response capability and resistance to signal attenuation, especially in detecting rapid cardiac events like the AO peak.

In conclusion, CYTOP FBGs exhibited superior performance across low, mid, and high-frequency excitation conditions. These results provide strong experimental support for the application of CYTOP fibers in full-band cardiac mechanical signal monitoring and lay a solid foundation for future studies involving real cardiac signal acquisition, recognition, and intelligent analysis.

## 5.4 In Vivo Cardiac Signal Monitoring Experiments

### 5.4.1 Experimental Setup and Background

To evaluate the sensor's performance in capturing physiological signals from the thoracic and upper limb regions, six sensing sites were selected based on commonly used SCG acquisition locations [81]. as illustrated in **Figure 74**.

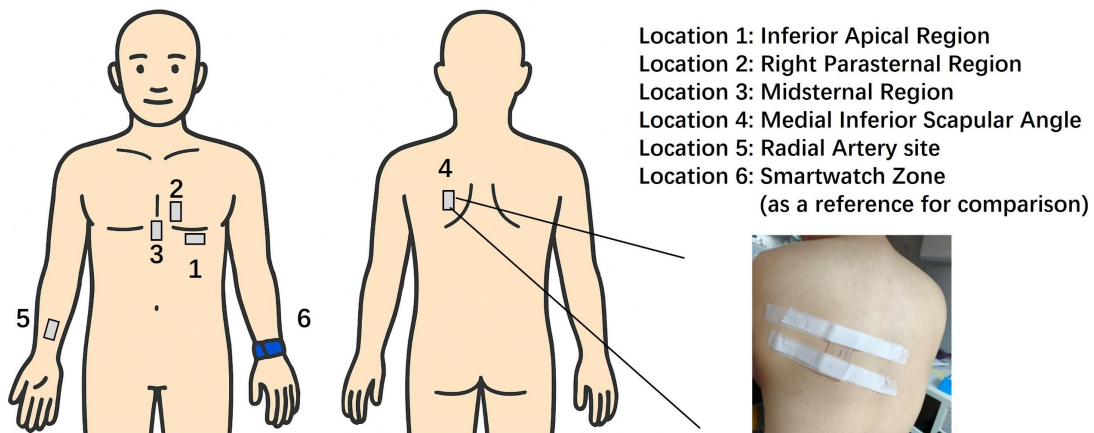


**Figure 74:** Layout at selected body locations

The selected sites are:

**Location 1:** Inferior Apical Region

**Location 2:** Right Parasternal Region

**Location 3:** Midsternal Region

**Location 4:** Medial Inferior Scapular Angle

**Location 5:** Radial Artery Site

**Location 6:** Smartwatch Zone (used as a HR reference)

All FBG sensors were attached using double-layer medical adhesive tape to ensure firm contact with the skin and optimal strain coupling.

The experiment included two parts:

- Thoracic Signal Acquisition (Sites 1–4):

A 24-year-old healthy male was monitored in standing, sitting, breath-hold, and natural breathing conditions. Signal amplitude, rhythm characteristics, and sensitivity variation across different postures were analyzed.

- Radial Artery Pulse Monitoring (Site 5):

Another 29 years old healthy male subject was tested under fist-clenching and relaxed-hand conditions to assess the sensor's ability to track fine pulse vibrations under different tension.

For heart rate reference, participants wore a smartwatch (OPPO Watch 4 Pro) on the left wrist during testing. This smartwatch integrates an 8-channel photoplethysmography (PPG) module with multi-wavelength emitters. It provides robust signal quality across various postures and skin tones. According to independent lab reports and public evaluations [82], the heart rate deviation of the device under resting conditions is less than  $\pm 2$  bpm compared to a professional ECG chest strap, confirming its reliability for use as a reference standard in this study.

#### 5.4.2 Signal Acquisition and Data Analysis Pipeline

After the sensing locations were configured, a complete signal acquisition and processing workflow was developed to enable multidimensional extraction of cardiac and respiratory mechanical signals using FBG sensors. As illustrated in **Figure 75**, this pipeline encompasses the full process from signal acquisition and preprocessing to feature extraction, providing a solid basis for heart rate estimation, respiratory tracking, and SCG signal analysis.

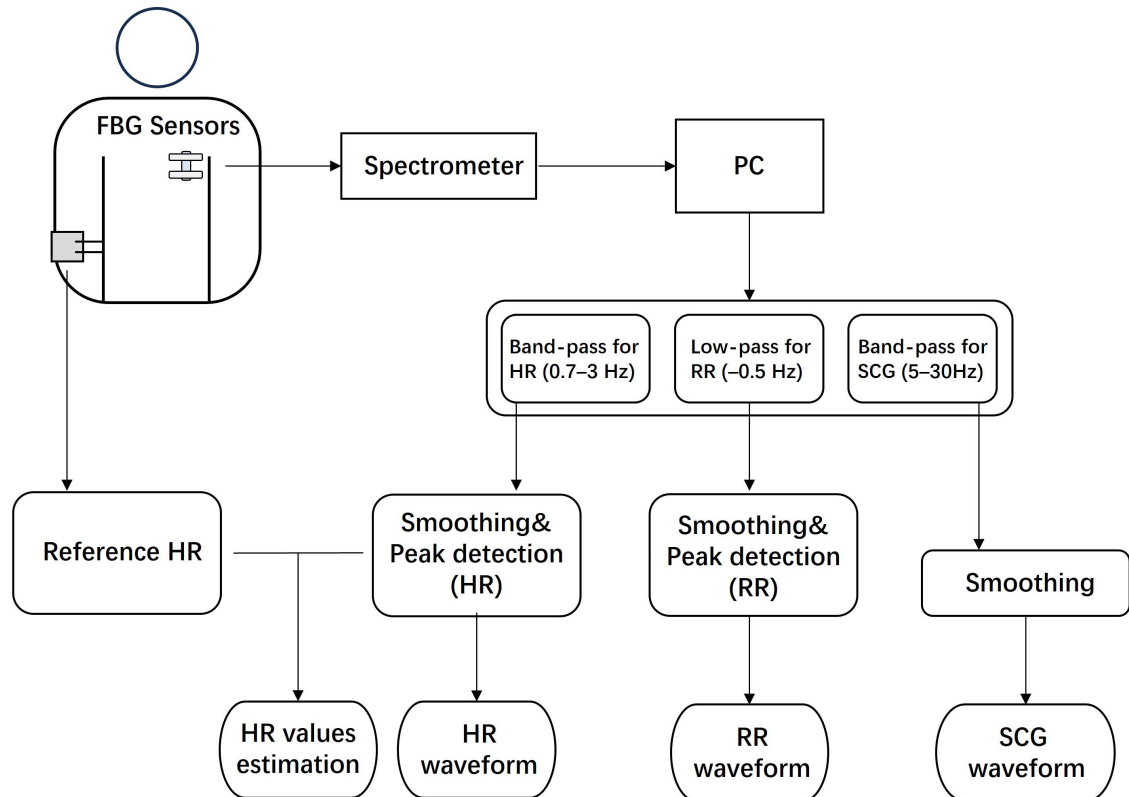


**Figure 75:** FBG-based system workflow for in vivo cardiac signal acquisition and processing

The system consists of:

- A multi-site FBG sensing unit
- A high-resolution optical demodulation device
- A back-end data processing platform

During acquisition, encapsulated FBG sensors adhered to key thoracic positions convert subtle skin vibrations into real-time Bragg wavelength shifts. These signals are transmitted via patch cords to the spectrometer for high-resolution demodulation.

The raw spectral data is transferred via USB to the upper computer (PC) for digital processing, including frequency filtering and physiological feature extraction. To differentiate various signal components, three parallel channels are employed:

- A 0.7–3 Hz bandpass filter for HR signal extraction
- A 0–0.5 Hz low-pass filter for respiration rate (RR) signal
- A 5–30 Hz bandpass filter to capture high-frequency components of SCG, especially the AO peak caused by aortic valve opening

Each filtered signal stream is processed via separate modules for smoothing and peak detection.

Additionally, heart rate readings from a smartwatch (used as Reference HR) are incorporated to assess the accuracy of the FBG-based system. Final system outputs include:

- Estimated HR values
- Continuous HR and RR waveforms
- Localized SCG feature profiles (e.g., AO peak markers)

#### **5.4.3 Preliminary Experiment: Sensor Positioning and Sensitivity Verification**

##### ***5.4.3.1 Sensor Positioning Method***

Due to the extremely subtle cardiac-induced thoracic vibrations, precise positioning of the sensor is critical for capturing stable and prominent heart signals during actual testing. To address this, the study proposes a positioning-assisted method based on an FBG array.

As described in the earlier sensor fabrication and packaging phase, three FBGs with center wavelengths of 1525 nm, 1550 nm, and 1575 nm were inscribed on a single SMF-28 fiber. These gratings were evenly spaced by 1 cm along the fiber axis and co-encapsulated in one PDMS unit, forming a simple one-dimensional multi-point FBG array.

Prior to formal testing, this array was attached as a whole to the surface of the target chest region, ensuring good skin contact. A 15-second heartbeat signal was collected under resting conditions. The results are shown in **Figure 76**, along with the Bragg wavelength response curve of a CYTOP FBG placed at the same central position.

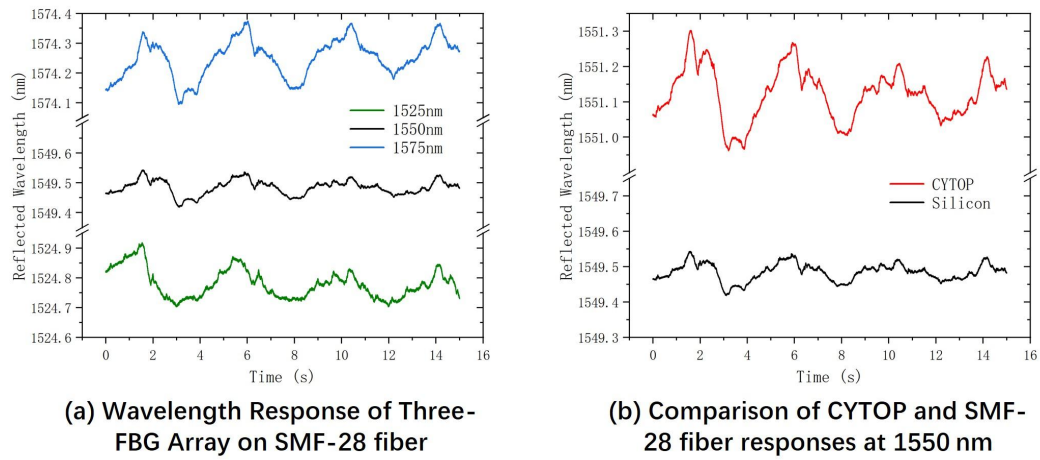


**Figure 76:** Initial signal comparison between multi-point SMF-28 FBG array and CYTOP FBG  
at the same location

By comparing the wavelength response curves of the three FBGs, it can be observed that although all of the 3FBGs waveforms in SMF-28 are generally similar, the 1575 nm FBG exhibits more pronounced periodic wavelength shifts, with higher signal amplitude and signal-to-noise ratio than the other two. This suggests that the corresponding location is closer to the main region of cardiac mechanical activity and has a stronger strain transmission path.

When comparing the responses of CYTOP and SMF-28 fibers placed at the same central location, it is evident that CYTOP fiber maintains a significantly higher sensitivity even under real human testing conditions.

Based on the above analysis, the overall position of the sensor was readjusted so that the CYTOP FBG, located at the center of the PDMS unit, aligns with the area of strongest vibration. This ensures optimal signal response at the given measurement site. The array-based positioning approach is simple and efficient, providing a quick reference for sensor placement across different individuals.

#### **5.4.3.2 Sensitivity Comparison Between the Two Fiber Types**

After readjusting the sensor placement, a comparative experiment was conducted to evaluate the response of the two types of fibers to subtle cardiac signals. A set of data was collected under breath-hold conditions and processed according to the filtering and smoothing workflow shown in **Figure 75**. Both the raw and processed signals are shown in **Figure 77**:

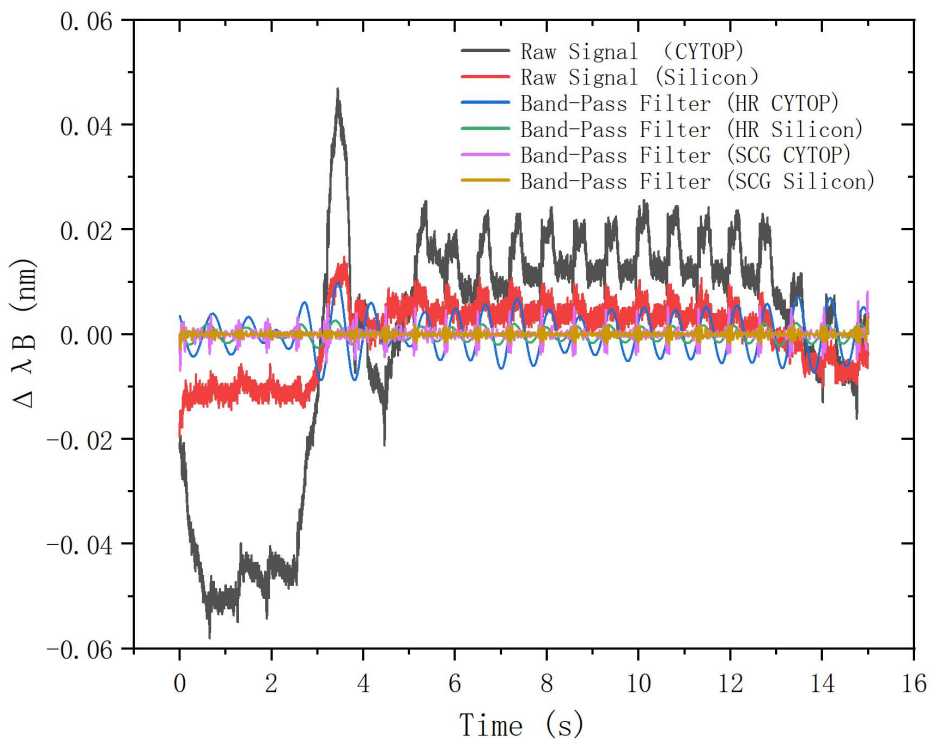


**Figure 77:** Raw and filtered signals collected by CYTOP and center SMF-28 FBGs

The HR waveform after 0.7–3 Hz bandpass filtering and smoothing is enlarged and shown in **Figure 78**.

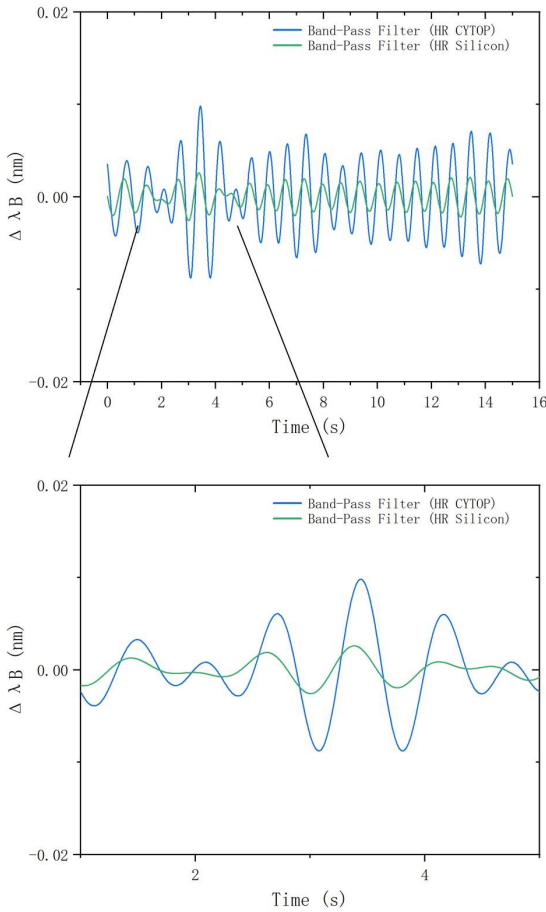


**Figure 78:** Enlarged HR waveform comparison: CYTOP vs. SMF-28

It can be observed that both CYTOP and SMF-28 fibers were able to clearly capture HR waveforms. However, during conditions involving large thoracic strain caused by breathing or slight body movement, the SMF-28 FBG often failed to present a distinct periodic HR waveform, which could hinder HR analysis and even lead to signal loss or inaccurate HR estimation.

For the detection of finer and higher-frequency SCG signals, the filtered (5–30 bandpass Hz) and smoothed results are shown in **Figure 79**:

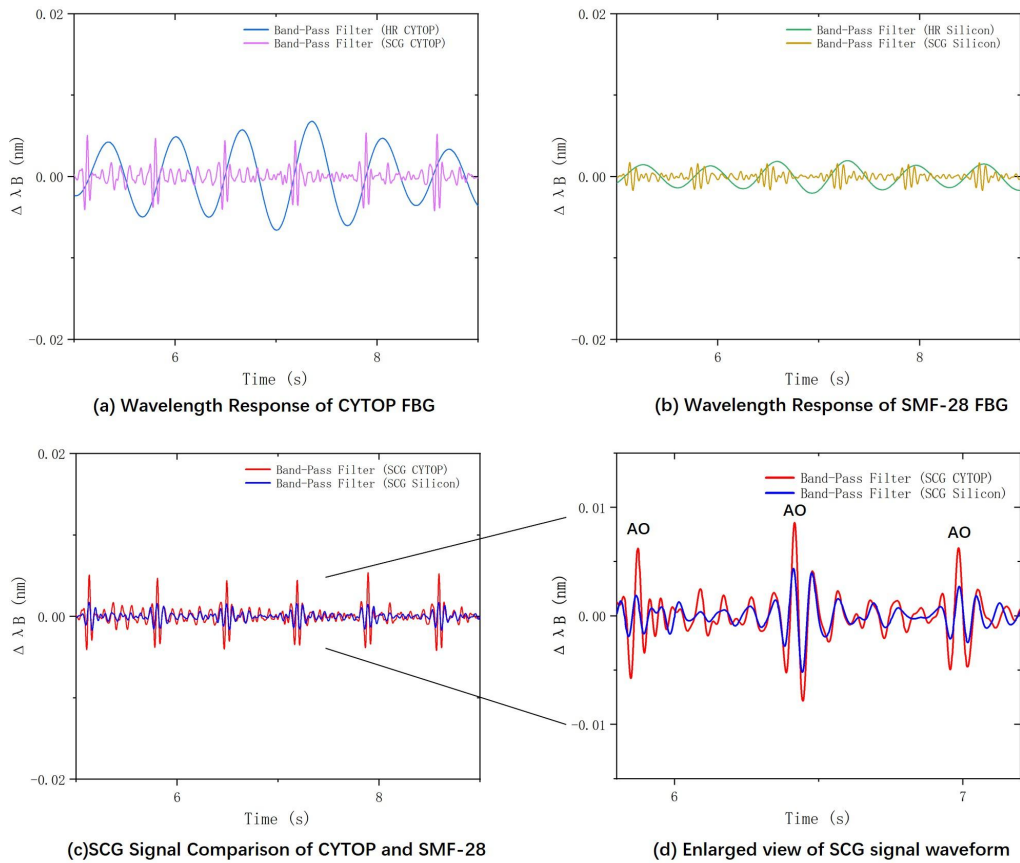


**Figure 79:** Enlarged SCG waveform comparison: CYTOP vs. SMF-28

The results clearly demonstrate the superior sensitivity of CYTOP fiber to subtle vibrations. Although both fiber types captured SCG signals aligned with the HR cycle, the SCG waveform detected by CYTOP showed more distinct AO peaks and a clearer overall waveform shape compared to SMF-28.

This advantage is particularly important for medical applications, where accurate identification of the AO peak in SCG (in conjunction with the R peak in ECG) is essential for calculating indicators like the pre-ejection period (PEP) [83], as well as for extracting and analyzing various SCG state points [84].

In summary, the experimental results confirm that CYTOP fiber maintains its high sensitivity advantage in detecting RR, HR, and SCG signals of varying amplitudes and frequencies under real human testing conditions. This further validates the conclusions drawn from previous vibration platform experiments.

#### **5.4.4 Cardiac Signal Analysis at Thoracic Sites**

Following the accurate positioning and sensitivity comparison of the sensors, cardiac signal measurements were conducted sequentially at predefined thoracic locations. To comprehensively evaluate the signal response characteristics under varying physiological and postural conditions, each sensor site was tested under two common postures—sitting and standing—and within each posture, measurements were performed under both normal breathing and breath-hold conditions. Each test lasted for 15 seconds.

The posture switching between sitting and standing was intended to assess how changes in chest wall tension and the relative position of the heart affect the FBG signal. The breath-hold condition was introduced to minimize low-frequency interference caused by respiration, thereby allowing the sensor to primarily respond to localized mechanical vibrations induced by heartbeats. This setup enhances the detection and analysis of high-frequency features such as SCG.

Through this test protocol, the signal variation patterns across different positions and conditions can be systematically identified, providing experimental evidence for optimizing sensor placement in real-world wearable applications.

##### ***5.4.4.1 Inferior Apical Region***

###### **1. RR and HR Monitoring under Normal Breathing**

###### **1.1 Sitting Posture**

Under sitting posture, the Bragg wavelength response collected by the CYTOP FBG attached to the inferior apical region is shown in **Figure 80**. The original signal was processed using a low-pass filter (0–0.5 Hz) to extract the RR component and a bandpass filter (0.7–3 Hz) to extract the HR component. Both filtered signals were then smoothed to isolate the periodic features associated with respiration and heartbeat.

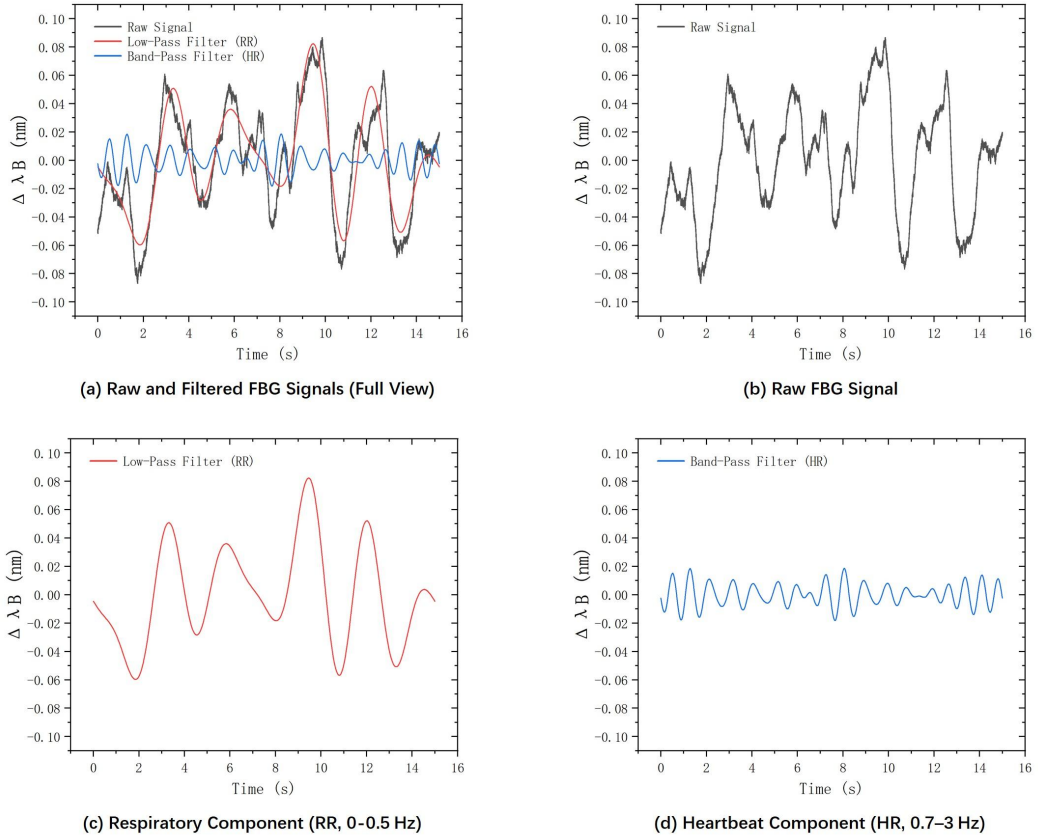


**Figure 80:** Response at the inferior apical region under sitting posture with normal breathing

By applying a peak detection algorithm based on zero-crossing of the first derivative to the filtered signals, a total of 5 respiratory cycles and 19 heartbeat-related cycles were identified. The calculated RR was 20 breaths per minute (breaths/min), and the HR was 76 beats per minute (bpm), based on the following formula:

$$RR = \frac{N_{RR}}{T} \times 60 \quad (30)$$

$$HR = \frac{N_{HR}}{T} \times 60 \quad (31)$$

where  $N_{RR}$  and  $N_{HR}$  denote the number of respiratory and cardiac cycles respectively, and  $T=15$  seconds is the duration of the test. The heart rate recorded by the reference smartwatch was 78 bpm.

## 1.2 Standing Posture

Under the standing posture, the Bragg wavelength response under normal breathing condition collected by the CYTOP FBG at the inferior apical region, along with the filtered and smoothed results, is shown in **Figure 81**.

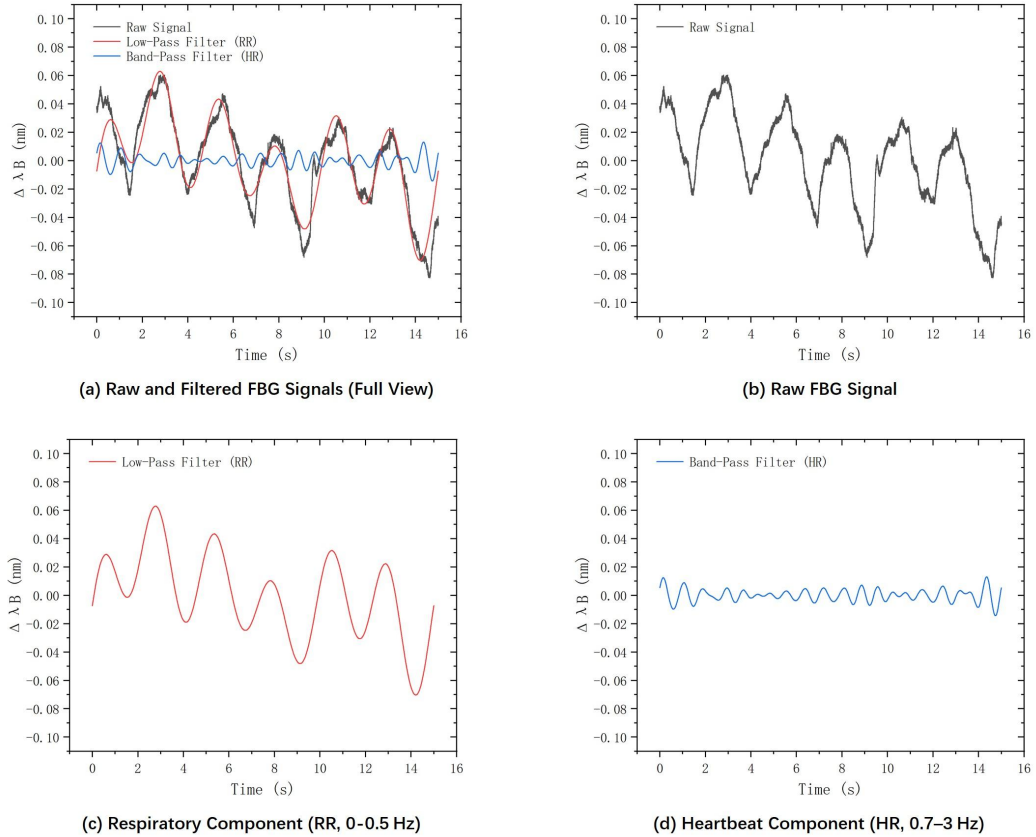


**Figure 81:** Response at the inferior apical region under standing posture with normal breathing

Using peak detection, a total of 6 respiratory cycles and 20 heartbeat-related cycles were identified. The resulting RR was calculated as 24 breaths/min, and the HR was 80 bpm. The reference heart rate was 83 bpm.

## 2. HR and SCG (AO Peak) Monitoring under Breath-Hold Condition

### 2.1 Sitting Posture

Under the sitting posture, the Bragg wavelength response collected by the CYTOP FBG at the inferior apical region during breath-hold is shown in **Figure 82**. The original signal was processed using two bandpass filters: 0.7–3 Hz for extracting the HR component, and 5–30 Hz for extracting SCG signals. Both filtered signals were further

smoothed to isolate the periodic features associated with cardiac cycles and subtle mechanical motion.

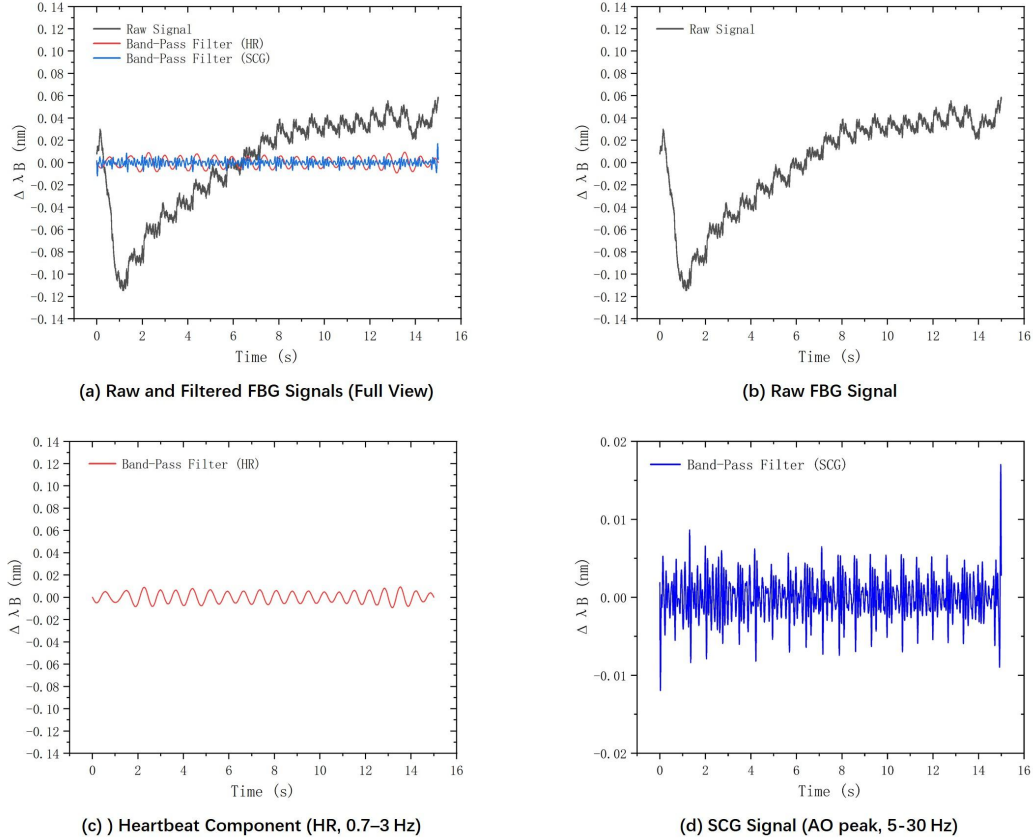


**Figure 82:** Response at the inferior apical region under sitting posture with breath- hold

Using a peak detection algorithm based on local maxima, a total of 21 heartbeat-related cycles were identified. Observing the SCG waveform, it was easy to distinguish the corresponding 21 periodic SCG events (excluding the segment affected by boundary noise). The resulting HR was calculated as 84 bpm, And the reference HR was 84 bpm.

## 2.2 Standing Posture

Under the standing posture, the Bragg wavelength response under breath-hold condition collected by the CYTOP FBG at the inferior apical region, along with the filtered and smoothed results, is shown in **Figure 83**.

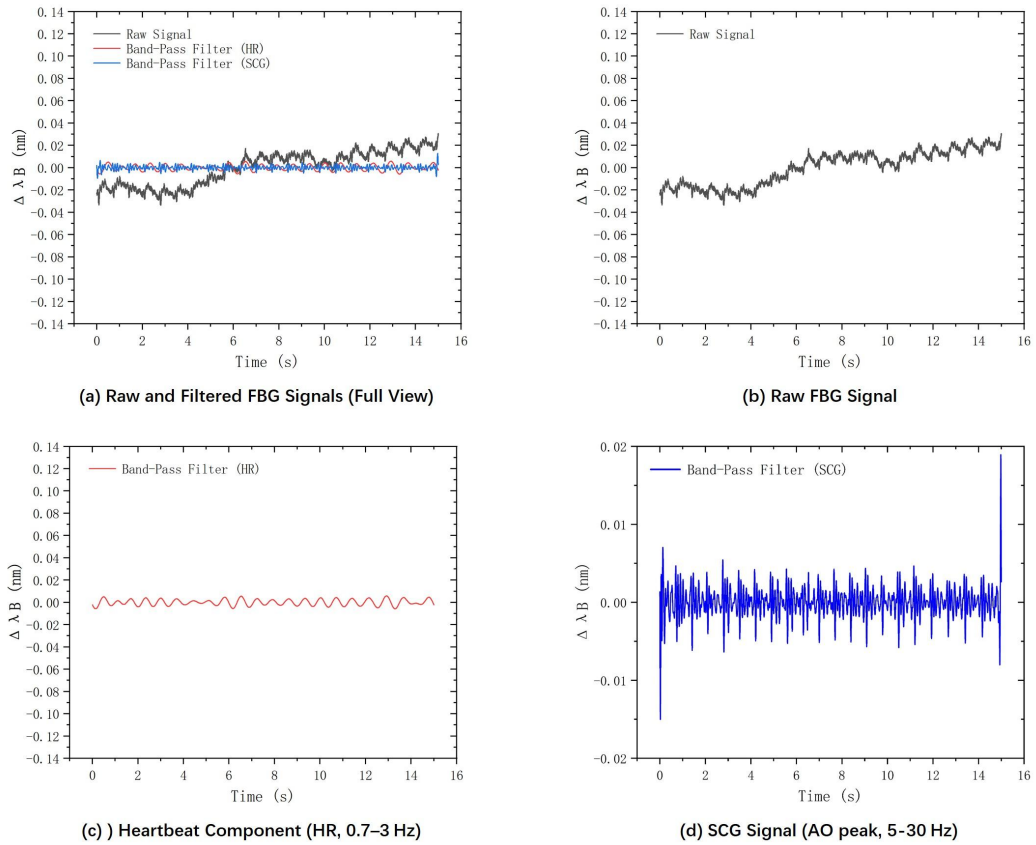


**Figure 83:** Response at the inferior apical region under standing posture with breath-hold

Using peak detection, a total of 22 heartbeat-related cycles were identified, and 22 corresponding periodic SCG events were clearly observed. The resulting HR was calculated as 88 bpm, and the reference HR was 87 bpm.

#### 5.4.4.2 Left Parasternal Region

##### 1. RR and HR Monitoring under Normal Breathing

###### 1.1 Sitting Posture

**Figure 84** shows the Bragg wavelength response collected at the left parasternal region in the sitting posture with normal breathing. Applied the same filtering and smoothing to extract RR and HR waveforms.

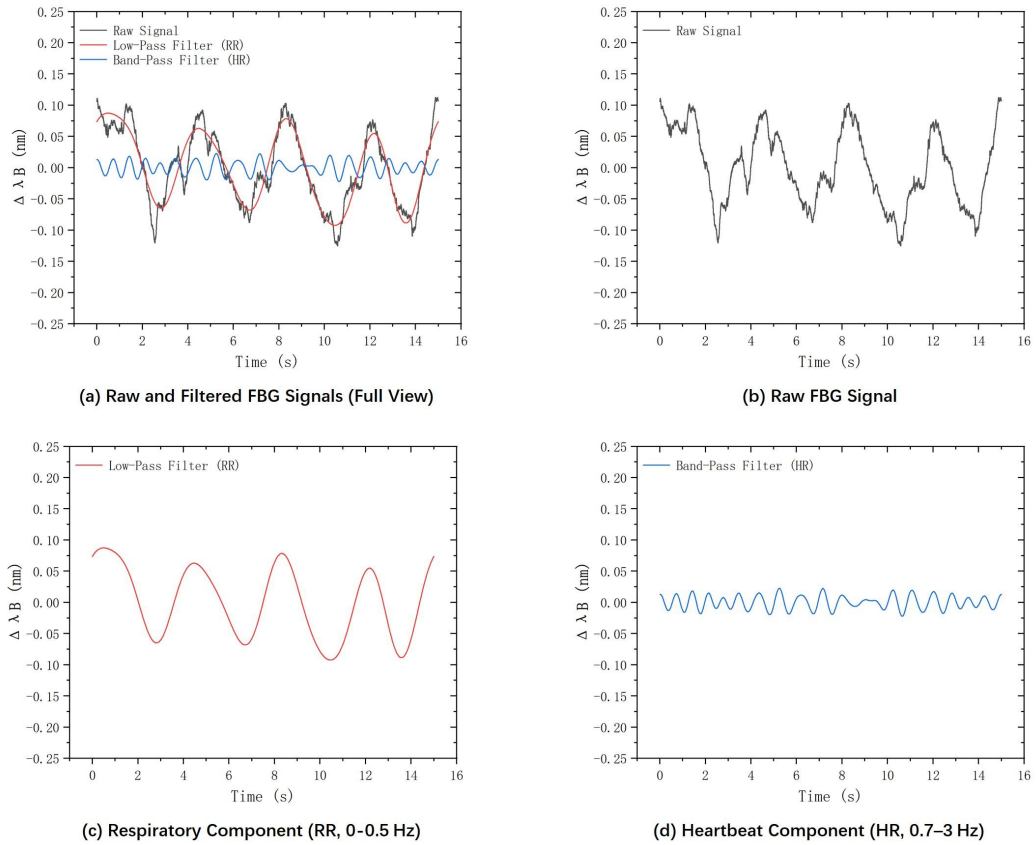


**Figure 84:** Response at the left parasternal region under sitting posture with normal breathing

A total of 4 respiratory cycles and 18 heartbeat-related cycles were identified. The resulting RR was calculated as 16 breaths/min, and the HR was 72 bpm. The reference HR recorded by the smartwatch was 75 bpm.

## 1.2 Standing Posture

**Figure 85** shows the response collected in the standing posture under normal breathing at the left parasternal region, processed using the same method for RR and HR analysis.

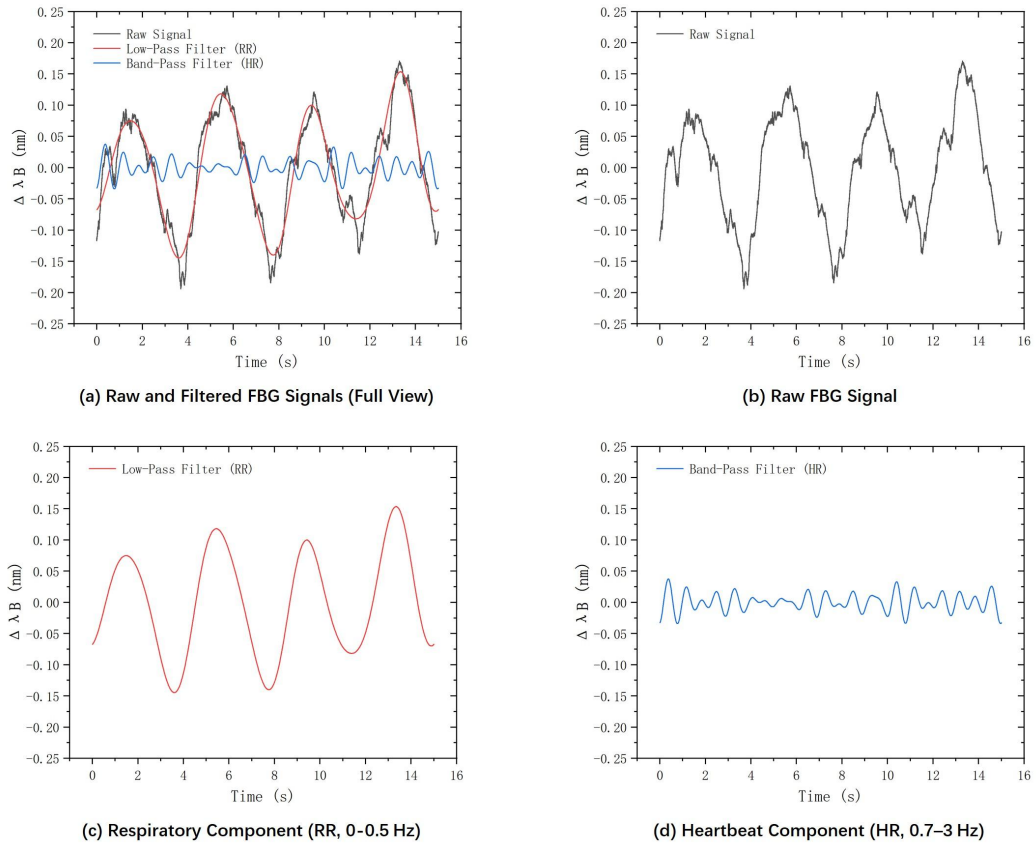


**Figure 85:** Response at the left parasternal region under standing posture with normal breathing

A total of 4 respiratory cycles and 21 heartbeat-related cycles were identified. The resulting RR was calculated as 16 breaths/min, and the HR was 84 bpm. The reference HR was 86 bpm.

## 2. HR and SCG (AO Peak) Monitoring under Breath-Hold Condition

### 2.1 Sitting Posture

**Figure 86** shows the Bragg wavelength response collected at the left parasternal region in the sitting posture under breath-hold condition. Applied the same filtering and smoothing as before (bandpass filters, 0.7–3 Hz for HR, 5–30 Hz for SCG) to extract HR and SCG waveforms.

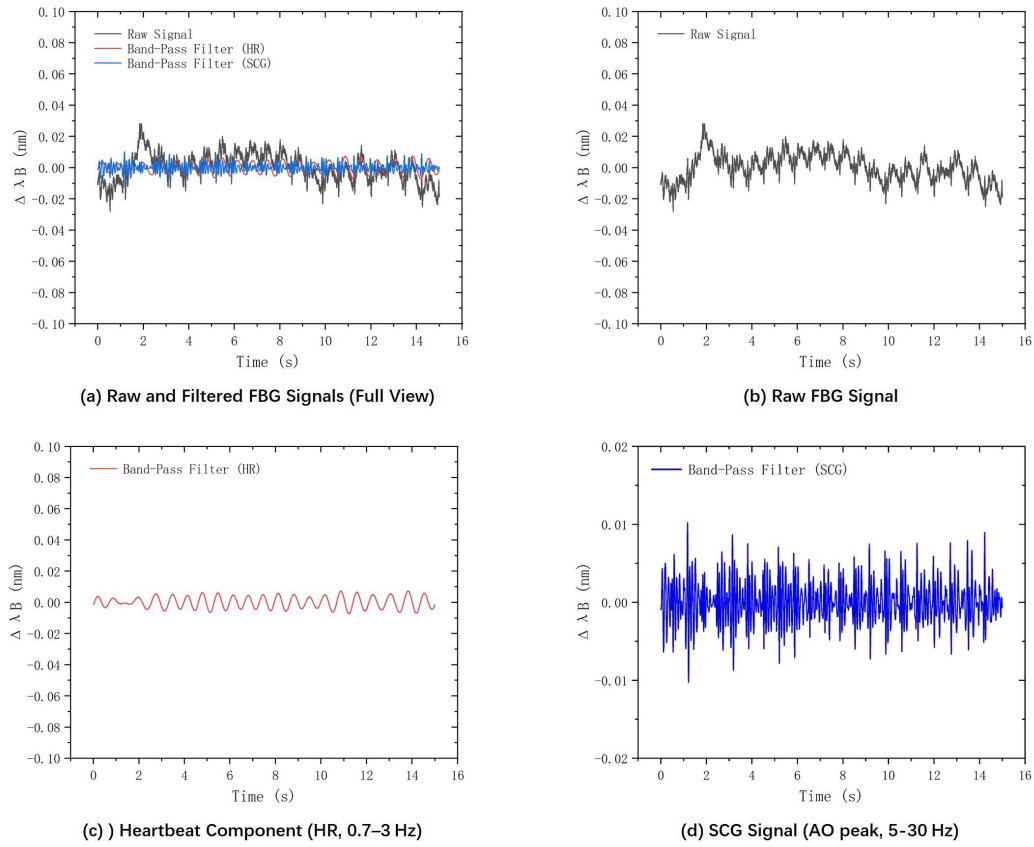


**Figure 86:** Response at the left parasternal region under sitting posture with breath-hold

Using peak detection, a total of 22 heartbeat-related cycles were identified, and 22 corresponding periodic SCG events were clearly observed. The resulting HR was calculated as 88 bpm, and the reference HR was 88 bpm.

## 2.2 Standing Posture

**Figure 87** shows the response collected in the standing posture under breath-hold condition at the left parasternal region, processed using the same method for HR and SCG analysis.

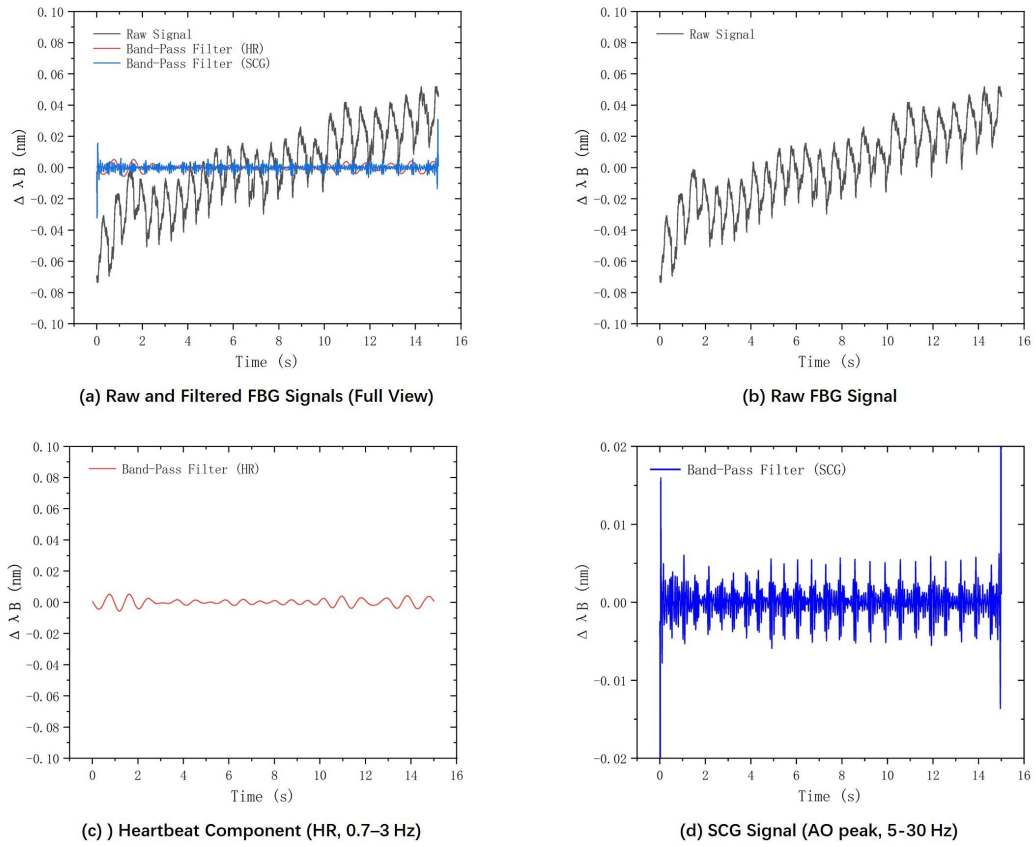


**Figure 87:** Response at the left parasternal region under standing posture with breath-hold

Using peak detection, a total of 20 heartbeat-related cycles were identified, and 20 corresponding periodic SCG events were clearly observed, excluding the segments affected by boundary noise. The resulting HR was calculated as 80 bpm, and the reference HR was 81 bpm.

#### 5.4.4.3 Midsternal Region

##### 1. RR and HR Monitoring under Normal Breathing

###### 1.1 Sitting Posture

**Figure 88** shows the Bragg wavelength response collected at the midsternal region in the sitting posture with normal breathing. Applied the same filtering and smoothing to extract RR and HR waveforms.

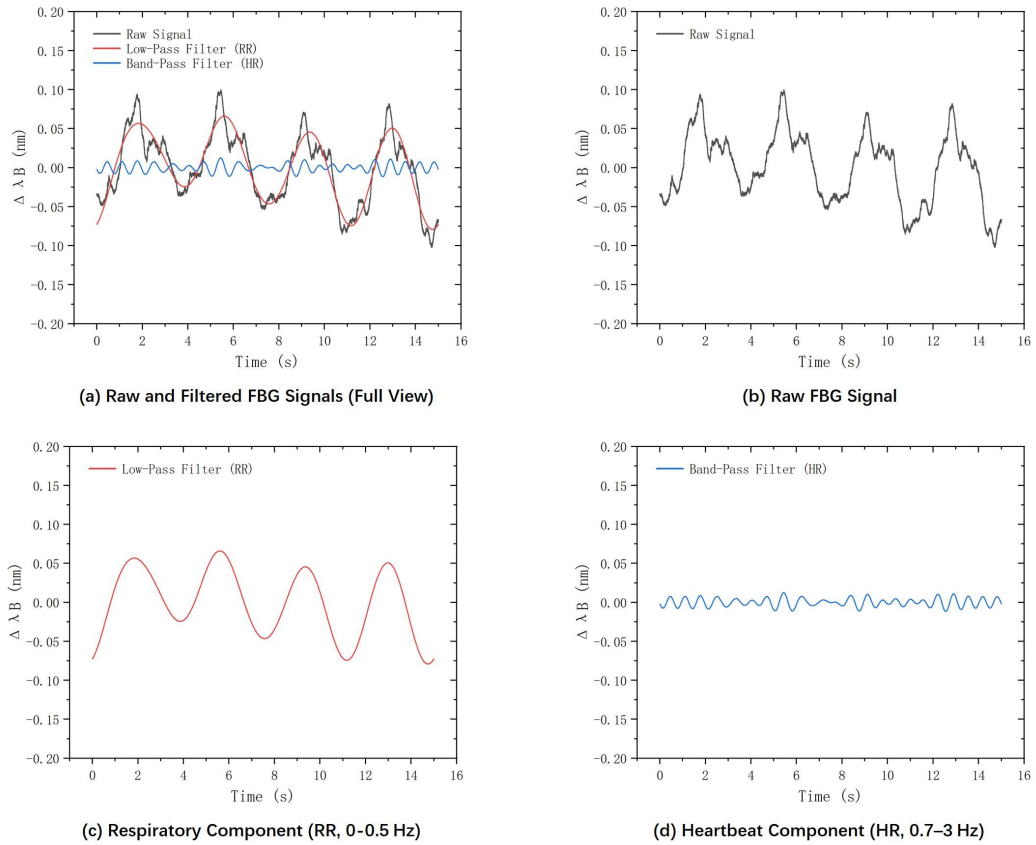


**Figure 88:** Response at the midsternal region under sitting posture with normal breathing

A total of 4 respiratory cycles and 22 heartbeat-related cycles were identified. The resulting RR was calculated as 16 breaths/min, and the HR was 88 bpm. The reference HR recorded by the smartwatch was 89 bpm.

## 1.2 Standing Posture

**Figure 89** shows the response collected in the standing posture under normal breathing at the midsternal region, processed using the same method for RR and HR analysis.

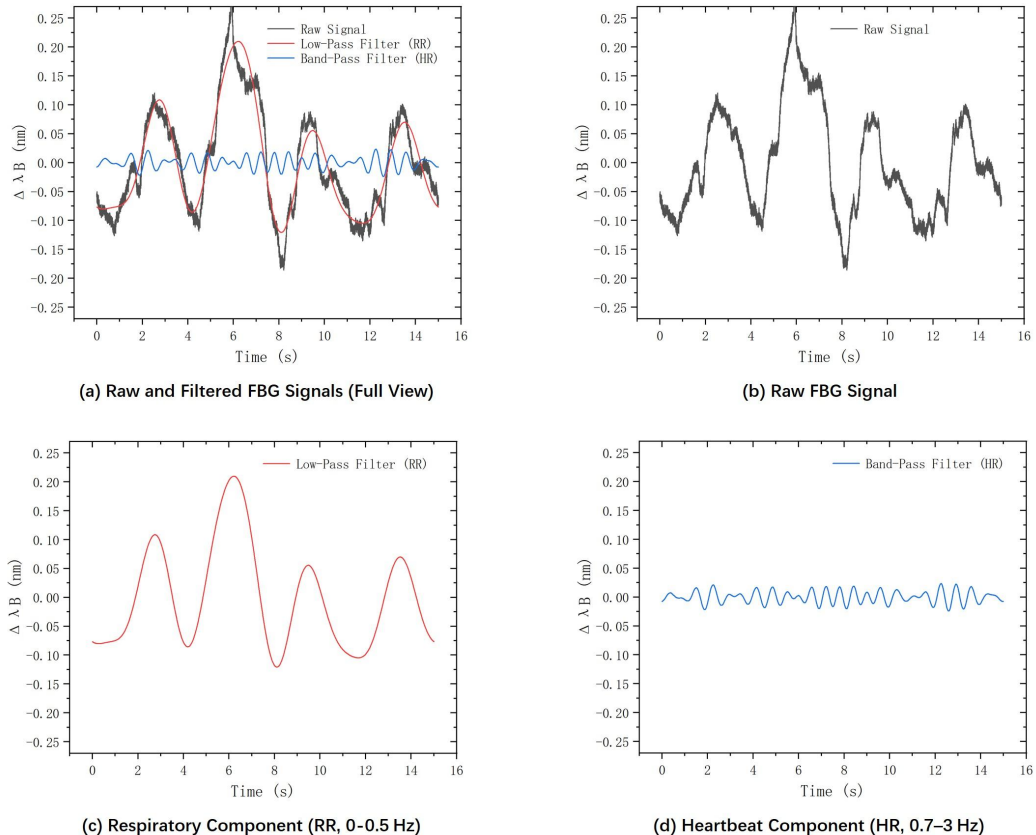


**Figure 89:** Response at the midsternal region under standing posture with normal breathing

A total of 4 respiratory cycles and 23 heartbeat-related cycles were identified. The resulting RR was calculated as 16 breaths/min, and the HR was 92 bpm. The reference HR was 91 bpm.

## 2. HR and SCG (AO Peak) Monitoring under Breath-Hold Condition

### 2.1 Sitting Posture

**Figure 90** shows the Bragg wavelength response collected at the midsternal region in the sitting posture under breath-hold condition. Applied the same filtering and smoothing as before (bandpass filters, 0.7–3 Hz for HR, 5–30 Hz for SCG) to extract HR and SCG waveforms.

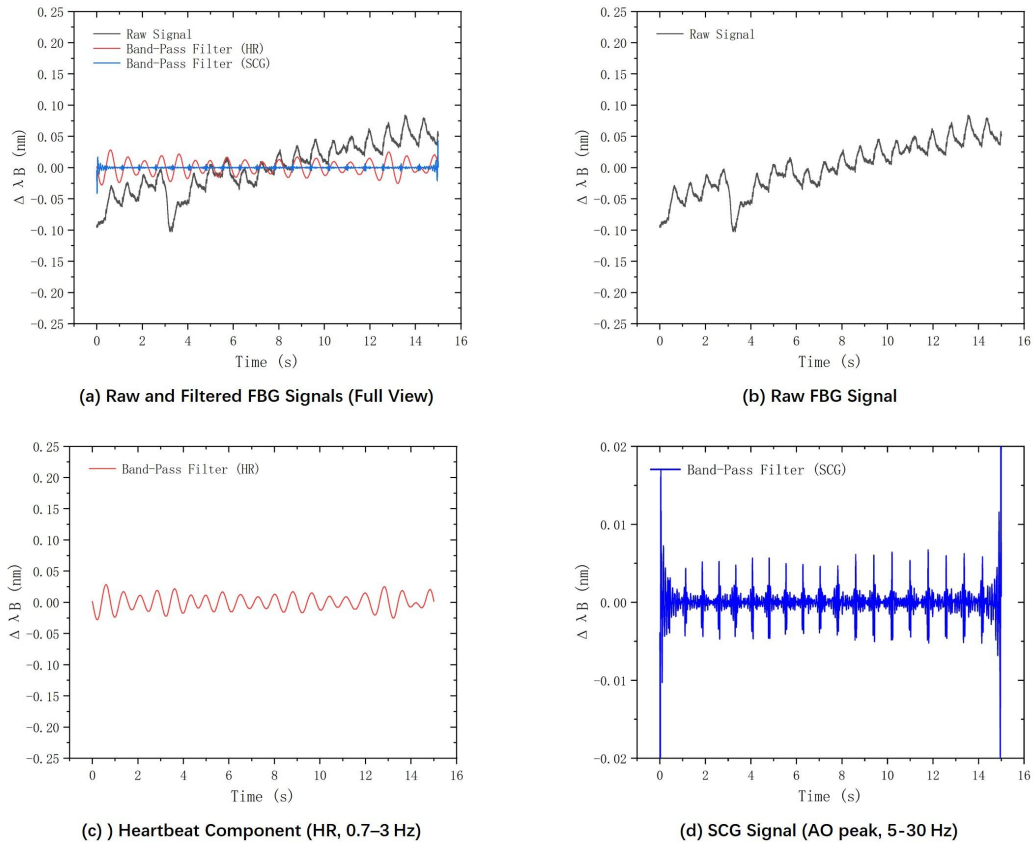


**Figure 90:** Response at the midsternal region under sitting posture with breath-hold

Using peak detection, a total of 20 heartbeat-related cycles were identified, and 20 corresponding periodic SCG events were clearly observed. The resulting HR was calculated as 80 bpm, and the reference HR was 80 bpm.

## 2.2 Standing Posture

**Figure 91** shows the response collected in the standing posture under breath-hold condition at the midsternal region, processed using the same method for HR and SCG analysis.

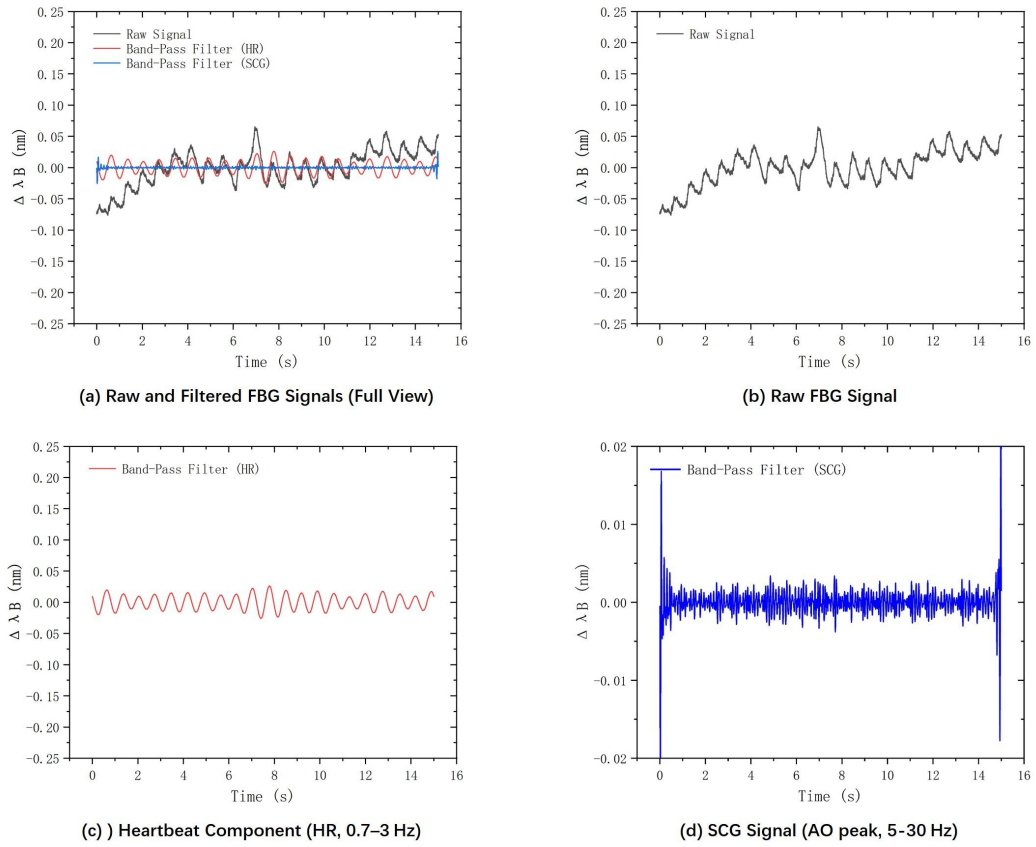


**Figure 91:** Response at the midsternal region under standing posture with breath-hold

Using peak detection, a total of 21 heartbeat-related cycles were identified, and 21 corresponding periodic SCG events were clearly observed. The resulting HR was calculated as 84 bpm, and the reference HR was 84 bpm.

#### 5.4.4.4 *Medial Inferior Scapular Angle*

##### 1. RR and HR Monitoring under Normal Breathing

###### 1.1 Sitting Posture

**Figure 92** shows the Bragg wavelength response collected at the medial inferior scapular angle in the sitting posture with normal breathing. Applied the same filtering and smoothing to extract RR and HR waveforms.

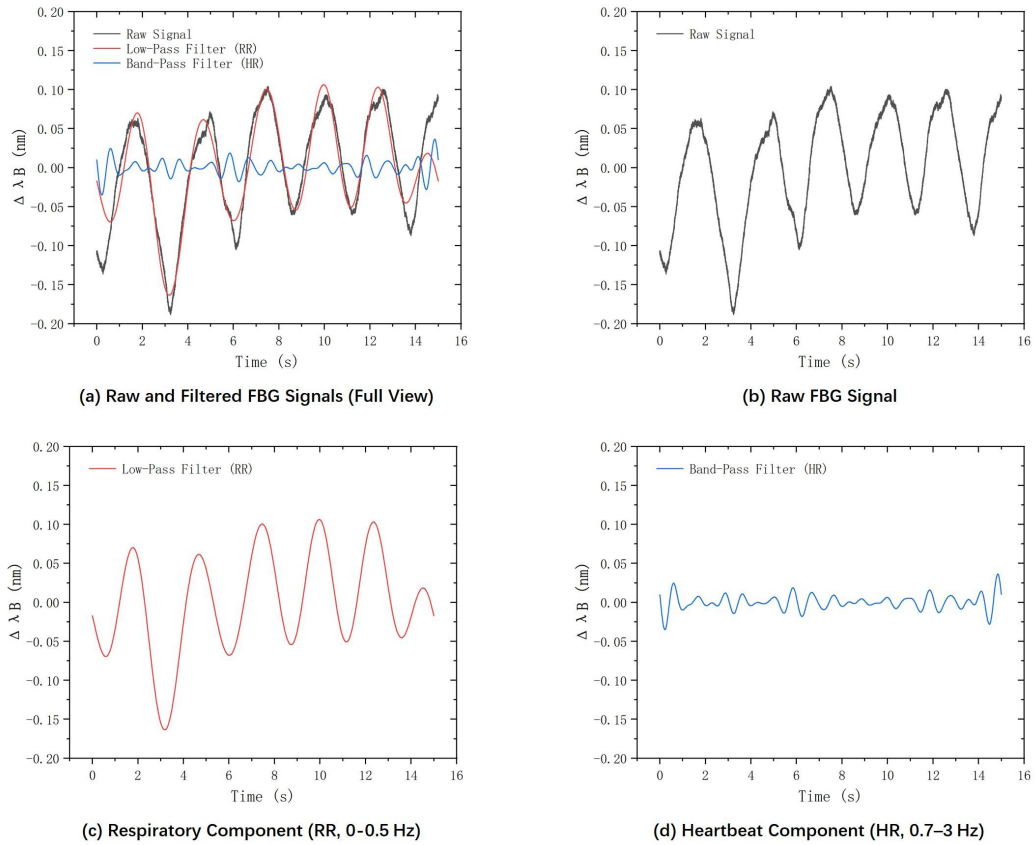


**Figure 92:** Response at the medial inferior scapular angle under sitting posture with normal breathing

A total of 6 respiratory cycles and 19 heartbeat-related cycles were identified. The resulting RR was calculated as 24 breaths/min, and the HR was 76 bpm. The reference HR recorded by the smartwatch was 83 bpm.

## 1.2 Standing Posture

**Figure 93** shows the response collected in the standing posture under normal breathing at the medial inferior scapular angle, processed using the same method for RR and HR analysis.

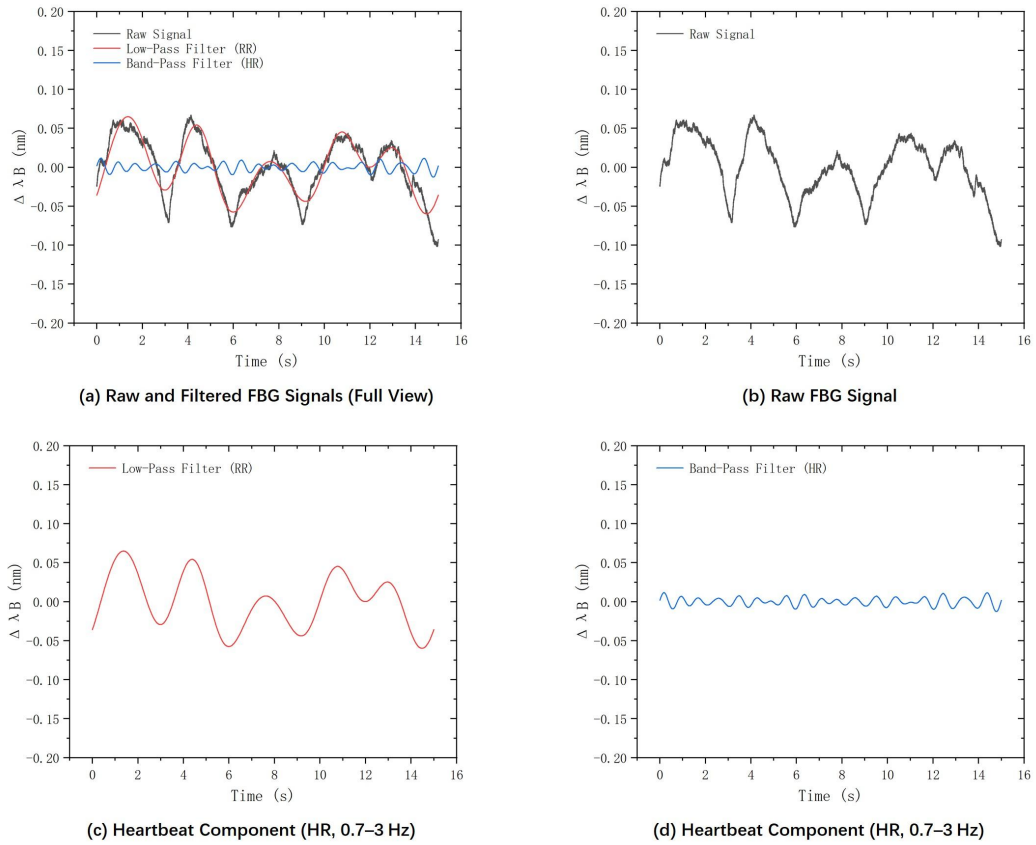


**Figure 93:** Response at the medial inferior scapular angle under standing posture with normal breathing

A total of 5 respiratory cycles and 19 heartbeat-related cycles were identified. The resulting RR was calculated as 20 breaths/min, and the HR was 76 bpm. The reference HR was 75 bpm.

## 2. HR and SCG (AO Peak) Monitoring under Breath-Hold Condition

### 2.1 Sitting Posture

**Figure 94** shows the Bragg wavelength response collected at the medial inferior scapular angle in the sitting posture under breath-hold condition. Applied the same filtering and smoothing as before (bandpass filters, 0.7–3 Hz for HR, 5–30 Hz for SCG) to extract HR and SCG waveforms.

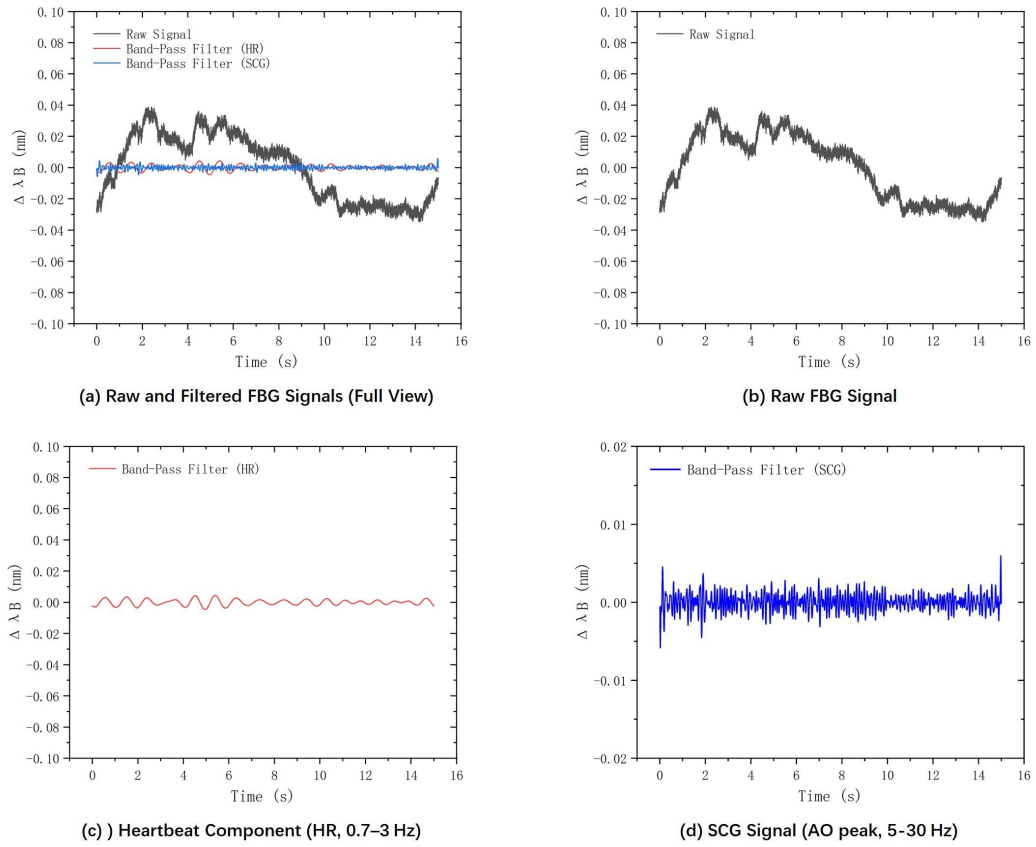


**Figure 94:** Response at the medial inferior scapular angle under sitting posture with breath-hold

Using peak detection, a total of 17 heartbeat-related cycles were identified. However, the SCG waveform lacked clear periodicity and did not align well with the cardiac rhythm, making it difficult to observe reliable heartbeat-related SCG events. The characteristic AO peaks could not be clearly distinguished. The resulting HR was calculated as 68 bpm, and the reference HR was 72 bpm.

## 2.2 Standing Posture

**Figure 95** shows the response collected in the standing posture under breath-hold condition at the medial inferior scapular angle, processed using the same method for HR and SCG analysis.

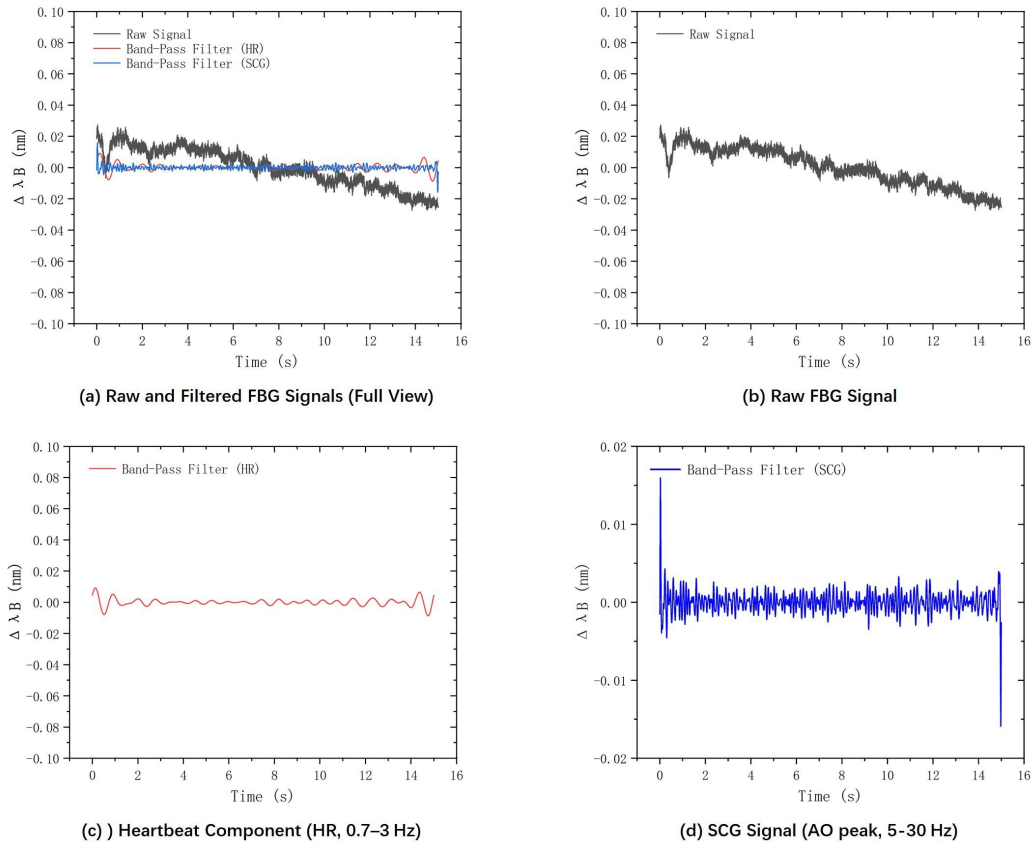


**Figure 95:** Response at the medial inferior scapular angle under standing posture with breath-hold

Using peak detection, a total of 21 heartbeat-related cycles were identified. However, only a portion of periodic SCG events were observed, indicating that the AO peaks appeared inconsistently and were fewer than the heartbeat cycles. The resulting HR was calculated as 84 bpm, and the reference HR was 86 bpm.

#### 5.4.5 Pulse Signal Detection at the Wrist

In addition to thoracic cardiac vibration monitoring, the sensing application was extended to radial pulse detection. As the wrist area is relatively small and requires firm sensor attachment, an elastic strap was used to secure the CYTOP FBG at the radial artery position.

## 1. Relaxed Condition

Under the relaxed condition, two sets of raw Bragg wavelength response signals were collected, as shown in **Figure 96**.

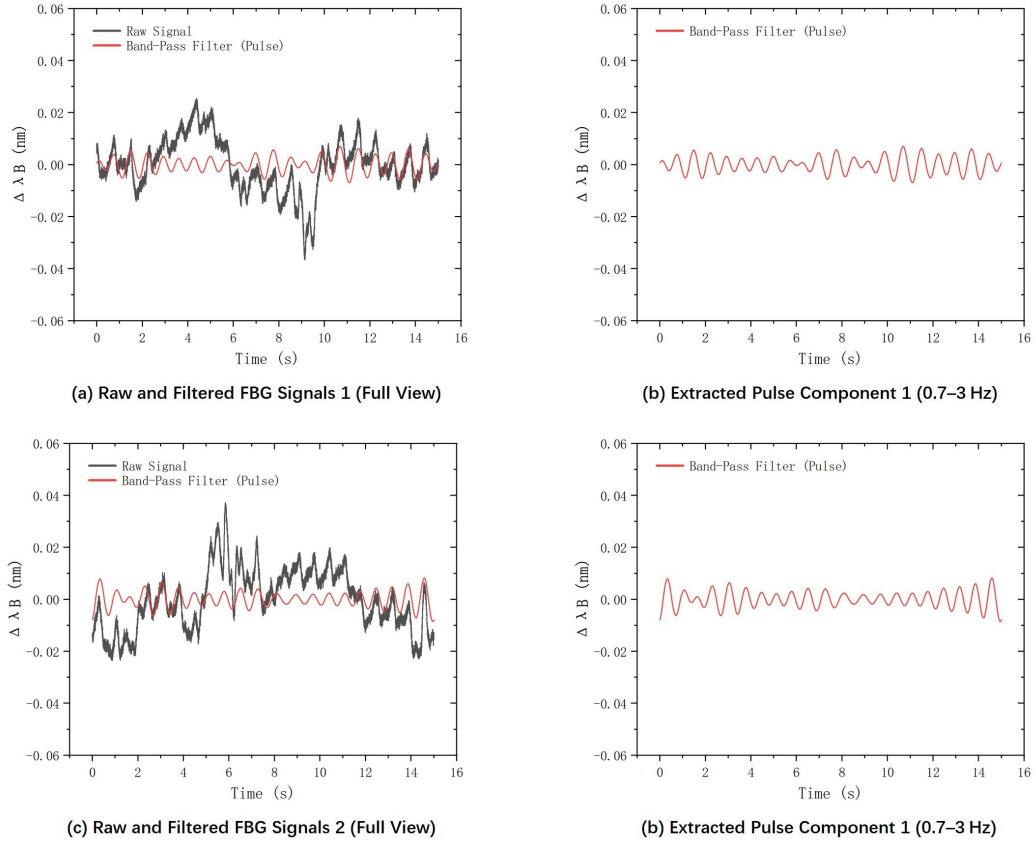


**Figure 96:** Bragg wavelength response of CYTOP FBG at the wrist under relaxed condition

After applying a bandpass filter (0.7–3 Hz) and smoothing, multiple distinct pulse cycles were successfully extracted.

## 2. Fist-Clenching Condition

**Figure 97** shows the Bragg wavelength response signal collected during a fist-clenching condition.

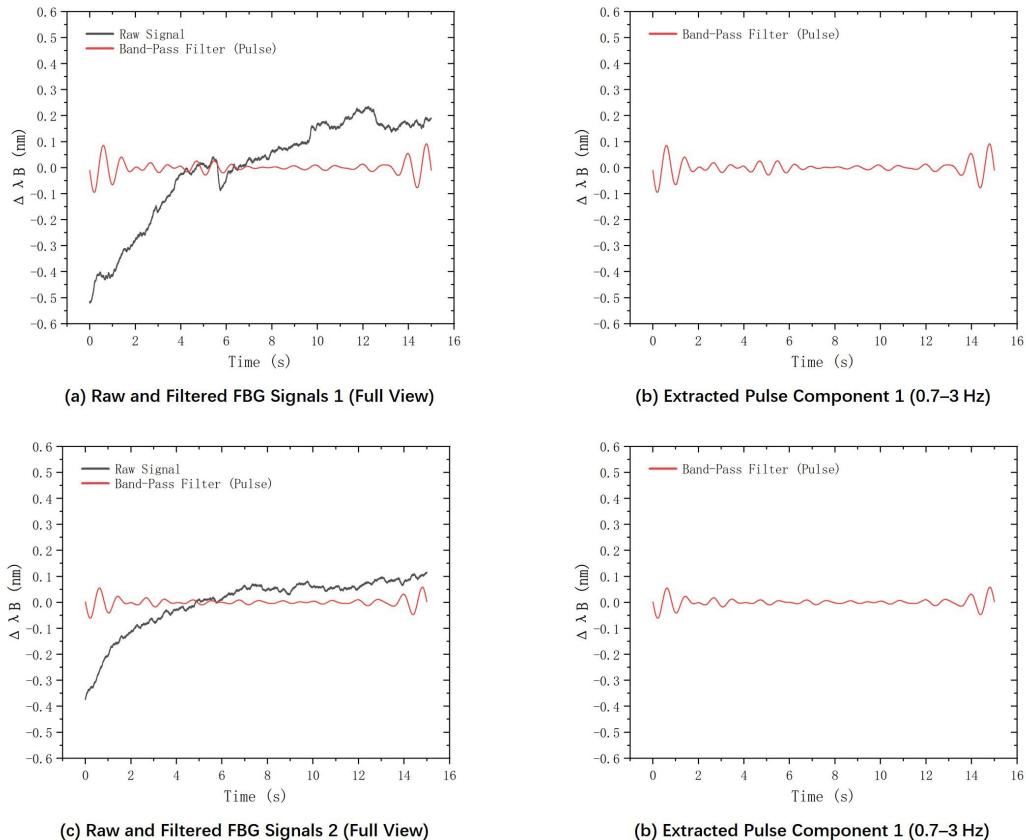


**Figure 97:** Bragg wavelength response of CYTOP FBG at the wrist under fist-clenching condition

Although the overall heartbeat rhythm remained identifiable, the waveform exhibited instability in some cycles, including distortions and reduced amplitudes. This may be attributed to local strain path alterations caused by muscle tension during fist clenching.

In summary, this simple test validated the feasibility of applying the designed sensor for pulse measurement at the wrist. However, the current configuration has notable limitations and would require structural redesign to accommodate the dynamic and variable movements of the wrist.

### 5.4.6 Signal Analysis and Evaluation

#### 1. Evaluation of Heart Rate Measurements

To evaluate the accuracy of HR detection at different measurement sites, all recorded HR values under various conditions were compared with the reference values obtained from a smartwatch. The corresponding errors and mean errors for each site were calculated and summarized in **Table 1**.

Position	<i>FBG</i>	<i>Reference</i>	<i>Bias</i>	<i>Mean Bias</i>
	(bpm)	(bpm)	(bpm)	(bpm)
<i>Inferior Apical Region</i>	76	78	-2	-1
	80	83	-3	
	84	84	0	
	88	87	1	
<i>Left Parasternal Region</i>	72	75	-3	-1.5
	84	86	-2	
	88	88	0	
	80	81	-1	
<i>Midsternal Region</i>	88	89	-1	0
	92	91	1	
	80	80	0	
	84	84	0	
<i>Medial Inferior Scapular Angle</i>	76	83	-7	-3
	76	75	1	
	68	72	-4	
	84	86	-2	

**Table 1:** Measured heart rate, reference heart rate, and error statistics across different test sites

Based on a comparative analysis of the table, it was observed that measurement errors occurred at all locations to varying degrees. Among them, the midsternal region exhibited the smallest error (0 bpm), while the medial inferior scapular angle showed the largest error (-3 bpm). These deviations are mainly due to the simplified method used in this study for estimating HR, which involved multiplying the number of heartbeat cycles within a fixed duration by 4, without correcting for waveform trends near the boundary of the measurement window.

Despite this, the midsternal region consistently demonstrated the lowest mean error, as it is least affected by respiratory movement and postural interference during actual measurements, thus yielding better strain coupling quality. In contrast, the medial inferior scapular angle suffered from reduced signal transmission due to the longer mechanical path from the heart, resulting in slightly lower measurement accuracy.

Overall, the HR errors across all test sites remained within  $\pm 3$  bpm, which meets the expected accuracy requirements of the designed system.

## 2. Detailed Comparison of SCG Signals

Based on the test results, three anatomical sites that consistently yielded stable SCG signals were selected for detailed analysis: the Inferior Apical Region, Left Parasternal Region, and Midsternal Region. Multiple measurements were conducted at each site, and the processed SCG waveforms are shown in **Figures 98, 99, and 100**, respectively.

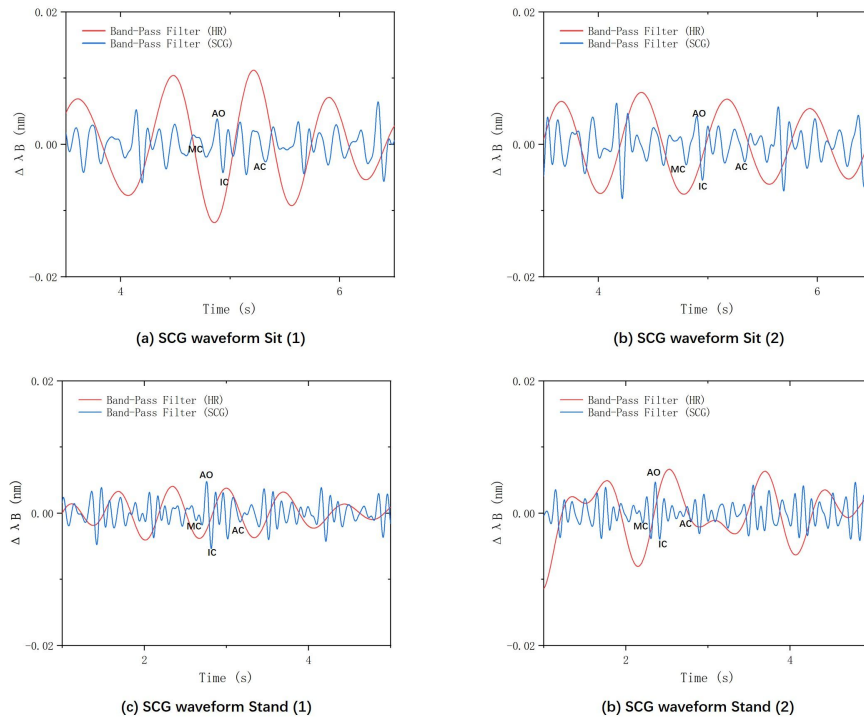


**Figure 98:** Detailed SCG waveform and annotated feature points at the Inferior Apical Region

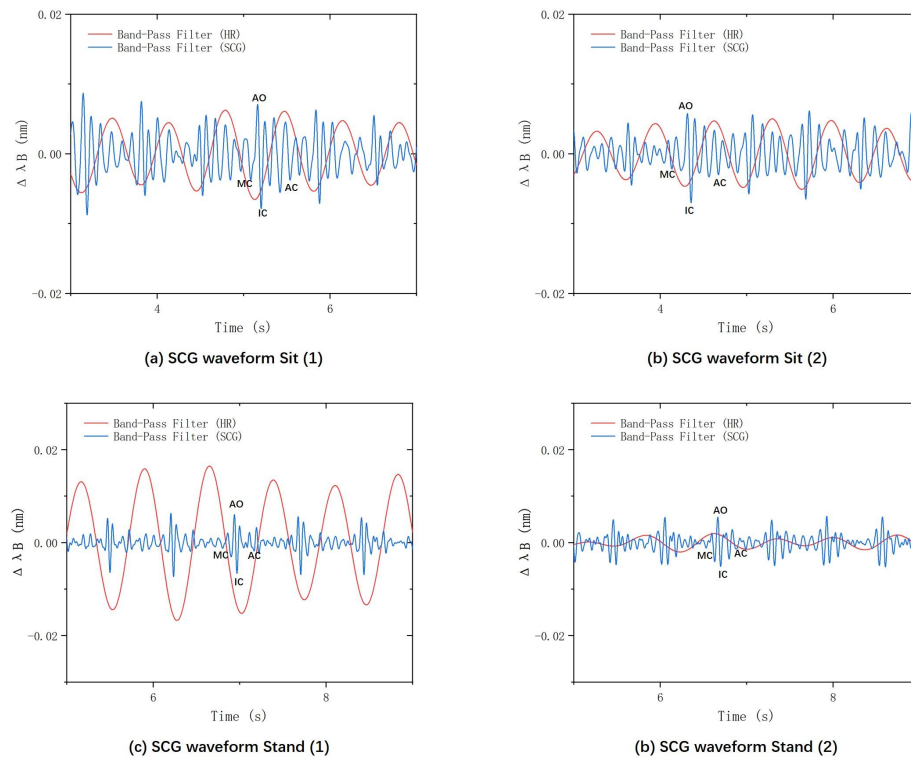


**Figure 99:** Detailed SCG waveform and annotated feature points at the Left Parasternal Region

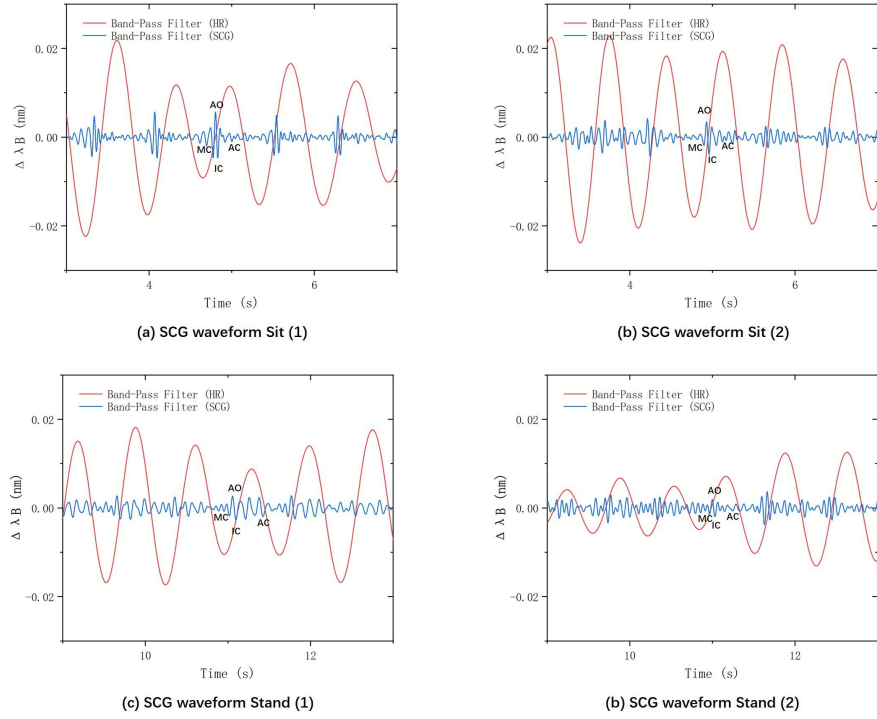


**Figure 100:** Detailed SCG waveform and annotated feature points at the Midsternal Region

Key mechanical events corresponding to the cardiac cycle were annotated on each SCG waveform, following the definitions provided in the literature [84], including:

- MC (Mitral valve Closure): Represents the onset of ventricular contraction.
- AO (Aortic valve Opening): Represents the start of blood ejection from the left ventricle.
- IC (Isovolumetric Contraction): Represents the end of isovolumetric contraction, occurring around the AO point.
- AC (Aortic valve Closure): Represents the end of ventricular systole.

From the waveform comparison, it can be observed that these characteristic SCG events can be clearly identified across all three measurement sites, demonstrating the sensor's ability to capture subtle cardiac mechanical activity. However, variations in noise levels were observed depending on the sensor placement and subject posture. Consistent with previous heart rate analysis results, the midsternal region under sitting posture exhibited the most distinct SCG waveform morphology, with clearly identifiable feature points and minimal noise interference, indicating superior signal stability at this location.

### **5.4.7 Experimental Summary**

In the in vivo experiments, we systematically validated the performance of the designed CYTOP FBG sensor across multiple anatomical sites and physiological states. Measurements were conducted at three thoracic positions—the Inferior Apical Region, Left Parasternal Region, and Midsternal Region—as well as one posterior site—the Medial Inferior Scapular Angle. For each site, signal acquisition was performed under both sitting and standing postures, and under normal breathing and breath-hold conditions.

The results demonstrated that the sensor was capable of accurately capturing RR, HR, and identifying detailed SCG waveform features, including key mechanical events (MC, AO, IC, AC). These findings confirm the sensor’s reliable signal coupling, directional sensitivity, and suitability for multipoint cardiac monitoring.

To further evaluate its versatility, the sensor was also applied to radial pulse monitoring at the wrist using an elastic strap. Clear pulse waveforms were successfully recorded, indicating the sensor’s potential for peripheral vascular signal detection in wearable scenarios.

Overall, the experimental results show that CYTOP fiber FBG sensors offer significant advantages over conventional silica-based optical fibers in detecting mechanical signals related to cardiac activity. These include superior sensitivity, better strain transfer efficiency, and improved resistance to motion artifacts. The outcomes of this study provide a strong theoretical and experimental foundation for future applications in clinical monitoring and non-invasive cardiac function assessment.

## Conclusion and Outlook

In this study, fiber Bragg gratings (FBGs) were successfully inscribed into polymer optical fibers (CYTOP) using a femtosecond laser plane-by-plane writing technique, and applied to the detection of cardiac mechanical signals in the human body. Experimental results demonstrated that the designed sensor system achieved its intended goals, verifying the feasibility of using CYTOP FBGs to detect SCG signals. This provides both experimental validation and theoretical support for the future development of dynamic, non-invasive cardiac monitoring technologies.

At present, ECG remains one of the most commonly used techniques for cardiac health assessment and is effective for monitoring arrhythmias. However, its sensitivity and specificity for diagnosing structural heart diseases are relatively limited. For the detection of mechanical cardiac dysfunctions, FBG-based systems offer advantages over conventional clinical tools such as echocardiography (ECHO) and coronary angiography (CAG). These include greater portability, flexibility, and lower cost—making them more suitable for non-invasive and continuous monitoring of cardiac mechanical activity.

While ECHO and CAG are powerful in evaluating structural and functional abnormalities, they also face challenges such as high operator dependence, elevated cost, and poor suitability for long-term dynamic monitoring. CAG, in particular, is invasive and associated with certain risks, making it unsuitable for frequent assessments. In contrast, the fiber optic sensing system designed in this study presents a convenient, accurate, and low-interference alternative with significant potential for practical application.

Despite the success of the current experiments, several aspects can be further improved in future research:

- **FBG inscription:** Multipoint FBG arrays can be written on a single CYTOP fiber to enable simultaneous multi-site measurements, enhancing spatial resolution and deployment flexibility.
- **Packaging optimization:** Reducing the thickness of the PDMS encapsulation can improve mechanical strain transmission and reduce damping of high-frequency signals.

- **Pre-strain optimization:** Graded loading (e.g., controlled bending or tensile force) can be introduced to systematically evaluate how different pre-strain levels affect sensitivity, ultimately identifying the optimal pre-strain configuration.
- **Vibration platform testing:** The excitation frequency and amplitude can be increased to explore the upper response limits of CYTOP-FBGs under extreme mechanical stimuli.
- **In vivo testing:** More physiological locations can be explored for signal acquisition, and signal processing algorithms for RR, HR, and SCG feature detection can be further optimized to improve accuracy under complex physiological conditions.
- **Reference signal acquisition:** Replacing the smartwatch-based heart rate reference with ECG allows precise alignment of SCG AO peaks with ECG R peaks, enabling the calculation of clinically valuable timing parameters such as pre-ejection period (PEP).
- **Sensor fixation improvements:** Enhanced fixation methods can improve stability during respiration and postural changes, ensuring higher SCG detection success rates and waveform completeness.
- **SCG waveform processing:** SCG signals can be segmented, aligned, and averaged across heartbeat cycles to generate a stable reference waveform suitable for medical-level time-domain analysis.
- **System integration:** A compact, integrated fiber optic sensor module can be developed to fully leverage the lightweight, flexible, low-power, and low-cost nature of optical fibers—making the system better suited for wearable, long-term, and real-time cardiac health monitoring applications.

## BIBLIOGRAPHY

- [1] Brito Díaz, Buenaventura, Alemán Sánchez, José Juan, Cabrera de León, Antonio. Frecuencia cardiaca en reposo y enfermedad cardiovascular[J]. Medicina Clinica, 2014, 143(1):34-38. DOI:10.1016/j.medcli.2013.05.034
- [2] Of the Report T W C. Report on cardiovascular health and diseases in China 2021: an updated summary[J]. Biomedical and Environmental Sciences, 2022, 35(7): 573-603. Burlacu A, Brinza C, Popa I V, et al. Influencing cardiovascular outcomes through heart rate variability modulation: A systematic review[J]. Diagnostics, 2021, 11(12): 2198.
- [3] Maas J J , Pinsky M R , Wilde R B D , et al. Cardiac output response to norepinephrine in postoperative cardiac surgery patients: interpretation with venous return and cardiac function curves.[J]. Critical Care Medicine, 2013, 41(1):143-150. DOI:10.1097/CCM.0b013e318265ea64.
- [4] Kause J , Smith G , Prytherch D , et al. A comparison of antecedents to cardiac arrests, deaths and emergency intensive care admissions in Australia and New Zealand, and the United Kingdom--the ACADEMIA study.[J]. Resuscitation, 2004, 62(3):275-282. DOI:10.1016/j.resuscitation.2004.05.016.
- [5] Anton O , Fernandez R , Rendon-Morales E , et al. Heart Rate Monitoring in Newborn Babies: A Systematic Review[J]. Neonatology, 2019, 116(3):1-12. DOI:10.1159/000499675.
- [6] European Society of Cardiology. European society of cardiology: Cardiovascular disease statistics 2019[J]. European Heart Journal, 2020, 41(1): 12-85.
- [7] Kim S J, Mesquita F C P, Hochman-Mendez C. New biomarkers for cardiovascular disease[J]. Texas Heart Institute Journal, 2023, 50(5).
- [8] Duarte A , Belo O . Cardiac well-being indexes: a decision support tool to monitor cardiovascular health.[J]. Journal of integrative bioinformatics, 2021, 18(2):127-138. DOI:10.1515/jib-2020-0040.
- [9] Neha, Sardana H K, Kanwade R, et al. Arrhythmia detection and classification using ECG and PPG techniques: A review[J]. Physical and Engineering Sciences in Medicine, 2021, 44(4): 1027-1048.
- [10] Esgalhado F, Batista A, Vassilenko V, et al. Peak detection and HRV feature evaluation on ECG and PPG signals[J]. Symmetry, 2022, 14(6): 1139.

- [11] Li H Z , Boulanger P .A Survey of Heart Anomaly Detection Using Ambulatory Electrocardiogram (ECG)[J].Sensors, 2020, 20(5):1461-.DOI:10.3390/s20051461.
- [12] Ikeda T .Current Use and Future Needs of Noninvasive Ambulatory Electrocardiogram Monitoring[J].Internal Medicine, 2021, 60(1).DOI:10.2169/internalmedicine.5691-20.
- [13] Hassan M A, Malik A S, Fofi D, et al. Video-based heartbeat rate measuring method using ballistocardiography[J]. IEEE Sensors Journal, 2017, 17(14): 4544-4557.
- [14] Kong L Q, Wu Y H, Pang Z G. Measurement of heart rate based on ballistocardiography[J]. Chinese Journal of Lasers, 2020, 47(2): 0207042.
- [15] Salerno D. M., Zanetti J. Seismocardiography: A new technique for recording cardiac vibrations. Concept, method, and initial observations. Journal of Cardiovascular Technology, 1990, 9(2): 111-118.
- [16] Crow R. S., Hannan P., Jacobs D., et al. Relationship between seismocardiogram and echocardiogram for events in the cardiac cycle. American Journal of Noninvasive Cardiology, 1994, 8(1): 39-46.
- [17] Yang J, Yang L, Liu W, et al. Analysis of the radial pulse wave and its clinical applications: a survey[J]. IEEE Access, 2021, 9: 157940-157959.
- [18] Pilz N, Heinz V, Ax T, et al. Pulse wave velocity: methodology, clinical applications, and interplay with heart rate variability[J]. Reviews in Cardiovascular Medicine, 2024, 25(7).
- [19] Dohlemann C, Guntner M, Ulmer H E. On reappraisal of auscultation and phonocardiography[J]. Monatsschrift Kinderheilkunde, 2003, 151(1): 78-81.
- [20] Kovács F, Horváth C, Balogh Á T, et al. Fetal phonocardiography—past and future possibilities[J]. Computer methods and programs in biomedicine, 2011, 104(1): 19-25.
- [21] Lin J, Fu R, Zhong X, et al. Wearable sensors and devices for real-time cardiovascular disease monitoring[J]. Cell reports physical science, 2021, 2(8).
- [22] He R, Shen L, Wang Z, et al. Optical fiber sensors for heart rate monitoring: A review of mechanisms and applications[J]. Results in Optics, 2023, 11: 100386.
- [23] Pospíšilová M, Kuncová G, Trögl J. Fiber-optic chemical sensors and fiber-optic bio-sensors[J]. Sensors, 2015, 15(10): 25208-25259.
- [24] Cano Perez J L, Gutiérrez-Gutiérrez J, Perezcampos Mayoral C, et al. Fiber optic

- sensors: a review for glucose measurement[J]. *Biosensors*, 2021, 11(3): 61.
- [25] Bujugundla R S, Pradhan H S. Emerging technologies for Fiber-Optic Based Sensors in Biomedical Domain: A Review and Recent Developments[J]. *IEEE Transactions on Instrumentation and Measurement*, 2024.
- [26] Vilela D, Romeo A, Sánchez S. Flexible sensors for biomedical technology[J]. *Lab on a Chip*, 2016, 16(3): 402-408.
- [27] Hong Y J, Jeong H, Cho K W, et al. Wearable and implantable devices for cardiovascular healthcare: from monitoring to therapy based on flexible and stretchable electronics[J]. *Advanced Functional Materials*, 2019, 29(19): 1808247.
- [28] Zhang Y, Chen Z, Hee H I. Noninvasive measurement of heart rate and respiratory rate for perioperative infants[J]. *Journal of Lightwave Technology*, 2019, 37(11): 2807-2814.
- [29] Li X, Li Y, Wei H, et al. A Review of Wearable Optical Fiber Sensors for Rehabilitation Monitoring[J]. *Sensors*, 2024, 24(11): 3602.
- [30] Lin S, Wang F, Qu Y, et al. An Anti-Jamming High-Temperature Sensor Based on Optical Fiber in-Line Mach-Zehnder Interferometer Structure[J]. *IEEE Sensors Journal*, 2024.
- [31] Polygerinos P, Zbyszewski D, Schaeffter T, et al. MRI-compatible fiber-optic force sensors for catheterization procedures[J]. *IEEE Sensors Journal*, 2010, 10(10): 1598-1608.
- [32] Chiavaioli F, Baldini F, Tombelli S, et al. Biosensing with optical fiber gratings[J]. *Nanophotonics*, 2017, 6(4): 663-679.
- [33] Irawati N, Hatta A M, Yhuwana Y G Y, et al. Heart rate monitoring sensor based on singlemode-multimode-singlemode fiber[J]. *Photonic Sensors*, 2020, 10: 186-193.
- [34] Lyu W, Yuan W, Yu J, et al. Non-Contact Short-Term Heart Rate Variability Analysis Under Paced Respiration Based on a Robust Fiber Optic Sensor System[J]. *IEEE Transactions on Instrumentation and Measurement*, 2024.
- [35] Agustiyanto, F. R. , Hatta, A. M. , Arifianto, D. , Radityo, M. , Maulana, P. S. , & Pikir, B. S. . An sms fiber structure for seismocardiography (scg) monitoring. *Results in Optics*, 19.
- [36] Othonos A. Fiber bragg gratings[J]. *Review of scientific instruments*, 1997, 68(12): 4309-4341.

- [37] Correia R, James S, Lee S W, et al. Biomedical application of optical fibre sensors[J]. *Journal of Optics*, 2018, 20(7): 073003.
- [38] Haseda Y, Bonefacino J, Tam H Y, et al. Measurement of pulse wave signals and blood pressure by a plastic optical fiber FBG sensor[J]. *Sensors*, 2019, 19(23): 5088.
- [39] Dziuda Ł, Skibniewski F W. A new approach to ballistocardiographic measurements using fibre Bragg grating-based sensors[J]. *Biocybernetics and Biomedical Engineering*, 2014, 34(2): 101-116.
- [40] De Tommasi F, Presti D L, Caponero M A, et al. Smart mattress based on multipoint fiber Bragg gratings for respiratory rate monitoring[J]. *IEEE Transactions on Instrumentation and Measurement*, 2022, 72: 1-10.
- [41] Leal-Junior A G, Diaz C A R, Avellar L M, et al. Polymer optical fiber sensors in healthcare applications: A comprehensive review[J]. *Sensors*, 2019, 19(14): 3156.
- [42] Lallana P C, Aldabaldetreku G, López A, et al. Sensing applications in aircrafts using polymer optical fibres[J]. *Sensors*, 2021, 21(11): 3605.
- [43] Nagar M A, Janner D. Polymer-Based Optical Guided-Wave Biomedical Sensing: From Principles to Applications[C]//*Photonics*. MDPI AG, 2024, 11(10): 972.
- [44] Alam M W, Islam Bhat S, Al Qahtani H S, et al. Recent progress, challenges, and trends in polymer-based sensors: a review[J]. *Polymers*, 2022, 14(11): 2164.
- [45] Ma H, Jen A K Y, Dalton L R. Polymer-based optical waveguides: materials, processing, and devices[J]. *Advanced materials*, 2002, 14(19): 1339-1365.
- [46] Yoshihara N. Performance of perfluorinated POF[C]//*Polymer Optical Fiber Conference*. 1997, 97.
- [47] Theodosiou A, Kalli K. Recent trends and advances of fibre Bragg grating sensors in CYTOP polymer optical fibres[J]. *Optical Fiber Technology*, 2020, 54: 102079.
- [48] Leal-Junior A, Theodosiou A, Díaz C, et al. Polymer optical fiber Bragg gratings in CYTOP fibers for angle measurement with dynamic compensation[J]. *Polymers*, 2018, 10(6): 674.
- [49] Liu H Y, Peng G D, Chu P L. Thermal stability of gratings in PMMA and CYTOP polymer fibers[J]. *Optics communications*, 2002, 204(1-6): 151-156.
- [50] Theodosiou A, Savva P, Mendoza E, et al. In-situ relative humidity sensing for ultra-high-performance concrete using polymer fiber Bragg gratings[J]. *IEEE Sensors Journal*, 2021, 21(14): 16086-16092.

- [51] Sui K, Ioannou A, Meneghetti M, et al. Temperature sensing of the brain enabled by directly inscribed Bragg gratings in CYTOP polymer optical fiber implants[J]. Optical Fiber Technology, 2023, 80: 103478.
- [52] Niu S, Wang W, Liu P, et al. Recent Advances in Applications of Ultrafast Lasers[C]//Photonics. MDPI AG, 2024, 11(9): 857.
- [53] Lei S, Zhao X, Yu X, et al. Ultrafast laser applications in manufacturing processes: A state-of-the-art review[J]. Journal of Manufacturing Science and Engineering, 2020, 142(3): 031005.
- [54] Martinez A, Dubov M, Khrushchev I, et al. Direct writing of fibre Bragg gratings by femtosecond laser[J]. Electronics letters, 2004, 40(19): 1.
- [55] Zhao J, Zhao Y, Peng Y, et al. Review of femtosecond laser direct writing fiber-optic structures based on refractive index modification and their applications[J]. Optics & Laser Technology, 2022, 146: 107473.
- [56] Marshall G D, Williams R J, Jovanovic N, et al. Point-by-point written fiber-Bragg gratings and their application in complex grating designs[J]. Optics express, 2010, 18(19): 19844-19859.
- [57] He J, Chen Z, Xu X, et al. Femtosecond laser line-by-line inscription of apodized fiber Bragg gratings[J]. Optics Letters, 2021, 46(22): 5663-5666.
- [58] Yang K, Liao C, Liu S, et al. Optical fiber tag based on an encoded fiber Bragg grating fabricated by femtosecond laser[J]. Journal of Lightwave Technology, 2020, 38(6): 1474-1479.
- [59] Duan T, Li X, Wang R, et al. Femtosecond Laser Plane-By-Plane Inscription of Chirped and Tilted Fiber Bragg Gratings[J]. Journal of Lightwave Technology, 2024.
- [60] Theodosiou A, Lacraz A, Stassis A, et al. Plane-by-plane femtosecond laser inscription method for single-peak Bragg gratings in multimode CYTOP polymer optical fiber[J]. Journal of Lightwave Technology, 2017, 35(24): 5404-5410.
- [61] Broadway C, Kinet D, Theodosiou A, et al. CYTOP fibre Bragg grating sensors for harsh radiation environments[J]. Sensors, 2019, 19(13): 2853.
- [62] Fajkus M, Kostelansky M, Fridrich M, et al. FBG sensor for heart rate monitoring using 3D printing technology[J]. IEEE Access, 2024.
- [63] Coimbra W, Oliveira P, Theodosiou A, et al. Strain measurement in hyrax appliances using FBG sensors in a 3D-printed human maxillary model[J]. IEEE

- Photonics Technology Letters, 2022, 34(15): 811-814.
- [64] Yi D, Huo Z, Geng Y, et al. PDMS-coated no-core fiber interferometer with enhanced sensitivity for temperature monitoring applications[J]. Optical Fiber Technology, 2020, 57: 102185.
- [65] Kai C, Yingping H, Dandan S, et al. A lossless fiber pressure sensor based on PDMS[J]. IEEE Access, 2020, 8: 189036-189042.
- [66] Zha B, Wang Z, Li L, et al. Wearable cardiorespiratory monitoring with stretchable elastomer optical fiber[J]. Biomedical Optics Express, 2023, 14(5): 2260-2275.
- [67] A J A N , A C M A , B G P A .Computational modeling of cardiac growth and remodeling in pressure overloaded hearts—Linking microstructure to organ phenotype[J].Acta Biomaterialia, 2020, 106:34-53.DOI:10.1016/j.actbio.2020.02.010.
- [68] 李宏男,任亮.结构健康监测光纤光栅传感技术[M].中国建筑工业出版社,2008.
- [69] Wei Z , Weimin C , Xiaohua L ,et al.Accuracy evaluation of demodulation results of fiber Bragg grating sensors[J].Applied Optics, 2017, 56(33):9212.DOI:10.1364/AO.56.009212.
- [70] Liu Z , Zhang Z F , Tam H Y ,et al.Multifunctional Smart Optical Fibers: Materials, Fabrication, and Sensing Applications[J].Photonics, 2019, 6(2):48.DOI:10.3390/photonics6020048.
- [71] Theodosiou A , Kalli K .Recent trends and advances of fibre Bragg grating sensors in CYTOP polymer optical fibres[J].Optical Fiber Technology, 54[2025-04-17].DOI:10.1016/j.yofte.2019.102079.
- [72] Meltz G , Morey W W , Glenn W H .Formation of Bragg gratings in optical fibers by a transverse holographic method[J].Optics Letters, 1989, 14(15):823-825.DOI:10.1364/OL.14.000823.
- [73] Hill K O , Malo B , Vineberg K A ,et al.Efficient mode conversion in telecommunication fibre using externally written gratings[J].Electronics Letters, 1990, 26(16):1270-1272.DOI:10.1049/el:19900818.
- [74] Martinez A , Dubov M , Khrushchev I ,et al.Direct writing of fibre Bragg gratings by femtosecond laser[J].Electronics Letters, 2004, 40(19):1170-1172.DOI:10.1049/el:20046050.

- [75] Smith G N, Kalli K, Sugden K. Advances in femtosecond micromachining and inscription of micro and nano photonic devices[J]. *Frontiers in guided wave optics and optoelectronics*, 2010, 674.
- [76] Theodosiou A, Lacraz A, Stassis A, et al. Plane-by-plane femtosecond laser inscription method for single-peak Bragg gratings in multimode CYTOP polymer optical fiber[J]. *Journal of Lightwave Technology*, 2017, 35(24): 5404-5410.
- [77] Lacraz A, Polis M, Theodosiou A, et al. Femtosecond laser inscribed Bragg gratings in low loss CYTOP polymer optical fiber[J]. *IEEE Photonics Technology Letters*, 2015, 27(7): 693-696.
- [78] Posporis A, Ioannou A, Kalli K. Pre-strain effects on CYTOP fibre Bragg grating temperature sensors[C]//Micro-Structured and Specialty Optical Fibres VII. SPIE, 2022, 12140: 119-124.
- [79] Obeid D, Sadek S, Zaharia G, et al. Doppler radar for heartbeat rate and heart rate variability extraction[C]//2011 E-Health and Bioengineering Conference (EHB). IEEE, 2011: 1-4.
- [80] Pandia K, Inan O T, Kovacs G T A. A frequency domain analysis of respiratory variations in the seismocardiogram signal[C]//2013 35th Annual International Conference of the IEEE Engineering in Medicine and Biology Society (EMBC). IEEE, 2013: 6881-6884.
- [81] Santucci F, Lo Presti D, Massaroni C, et al. Precordial vibrations: A review of wearable systems, signal processing techniques, and main applications[J]. *Sensors*, 2022, 22(15): 5805.
- [82] Zhou G, Zhao W, Zhang Y, et al. Comparison of OPPO Watch Sleep Analyzer and Polysomnography for Obstructive Sleep Apnea Screening[J]. *Nature and Science of Sleep*, 2024: 125-141.
- [83] Chu C Y, Lee W H, Hsu P C, et al. Myocardial performance index derived from pre-ejection period as a novel and useful predictor of cardiovascular events in atrial fibrillation[J]. *Journal of cardiology*, 2015, 65(6): 466-473.
- [84] Inan O T, Migeotte P F, Park K S, et al. Ballistocardiography and seismocardiography: A review of recent advances[J]. *IEEE journal of biomedical and health informatics*, 2014, 19(4): 1414-1427.